NAUSIVIOS CHORA

A Journal in Naval Sciences and Technology

PART B:

Electrical Engineering and Computer Science

ΝΑΥΣΙΒΙΟΣ ΧΩΡΑ

Περιοδική Έκδοση Ναυτικών Επιστημών

ΜΕΡΟΣ Β:

Επιστήμες Ηλεκτρολόγου Μηχανικού και Μηχανικού Υπολογιστών

Volume 7/2018 - Τεύχος 7/2018

TABLE OF CONTENTS

Reliability and Availability Study of Modern Indoor VLC Systems with eSSK Modulation

A.N. Stassinakis[a*], N.A. Androutsos[a] and A.D. Tsigopoulos[b]

[a]*Department of Electronics, Computers, Telecommunications and Control, Faculty of Physics, National and Kapodistrian University of Athens, Athens, 15784, Greece,*
emails: {a-stasinakis; nickandr}@phys.uoa.gr
[b] *Department of Battle Systems, Naval Operations, Sea Studies, Navigation, Electronics and Telecommunications, Hellenic Naval Academy, Hadjikyriakou ave,*
Piraeus 18539, Greece, e-mail: atsigo@snd.edu.gr
**Corresponding Author*

Abstract. Indoor visible light communication (VLC) systems that use Light Emitting Diode (LED) technology are used in various modern very high data rate communication applications due to the plenty of advantages they offer such as their very high bandwidth and their low operational and installation cost. Furthermore, due to the weakness of light to penetrate the walls, such systems have very low vulnerability to security attacks so they are suitable for indoor military communications. VLC systems can be easily deployed in navy ships or submarines where security and low power consumption are very important factors. In order to increase the performance of such systems, many modulation techniques can be used with the enhanced Space Shift Keying (eSSK) being an effective one. The drawback of such modulation technique is the decrease of the coverage area for a receiver that needs to communicate with all Light Emitting Diode (LED) transmitters. In this work, the coverage area and the performance of the system will be investigated for various patterns of LED transmitters. The performance metric that will be calculated is the bit error rate (BER), a very important metric that is associated with the reliability of the system and its value is strictly determined in modern communication standards. So by achieving lower BER using eSSK technique, the communication systems become more suitable for modern applications. Simulation results will be provided for the performance of the VLC system.

Keywords: Visible light communications, eSSK, Bit error rate, LED.
PACS: 42.79.Sz

I. INTRODUCTION

The last few years there is an increasing scientific research and commercial interest for Visible Light Communication (VLC) systems, since they offer many advantages and can successfully cover the requirements of modern communication systems, [1]. The most important of them are the high data rate they can achieve, along with the low installation and operational cost, [2], and that's why they will be extensively used for 5th generation (5G) networks in order

ISSN:1791-4469

to solve many issues of modern networks, [1], [3]. Moreover, these systems operating in visible electromagnetic spectrum where no license is required, while at the same time these frequencies are environmentally friendly and completely safe for humans [1]. These advantages, have introduced Light Fidelity (LiFi) systems, which already being used commercially, [4], [5], for data transmission, while at the same time they offer room illumination. Furthermore, VLC systems, are suitable for fulfilling global communication and information projects such as smart home and smart cities applications, [1], [2], [6].

An effective modulation technique for the VLC systems is the space shift keying (SSK) which is a kind of spatial modulation technique where each transmitter is active in a specific time slot and transmits a unique symbol, [2], [7], [8]. In conventional SSK, the duration and the amplitude of the transmitted pulses are the same for every transmitter while in eSSK their width is different and unique for each transmitter, [2]. In this work the BER performance of the eSSK VLC system is estimated.

However, a performance mitigation factor of the VLC systems, as for every wireless communication system, is the incoming noise through the receiver's photodiode which deteriorates the signal to noise ratio (SNR) of the optical link, [1], [9], [10]. A very significant coefficient that increases the noise of such a system is the background optical noise, and the main source of this, is the sunlight radiation which is difficult to be avoided. In this work, in order to reduce the effect of background noise, we adopt the technique of , [1], with the application of an optical filter, [11], [12], at the receiver's photodiode. In this way, we can decrease the received wavelength range, that's not used for data transmission.

The remainder of this work is organized as follows: in section II we describe the system model, while in Section III we derive mathematical expression for the SNR after the application of an optical filter at the receiver, and we study the technique of the coverage area calculation. Next, in section IV we estimate the Bit Error Rate (BER) of the system, while in Section V we demonstrate the corresponding numerical results for the BER of the system. Finally, the conclusions are presented in Section VI.

II. SYSTEM MODEL

In this work we consider that 4 Red Green Blue (RGB) white LED lamps have been installed on the ceiling of a room, with height h, for illumination and data transmission. The length and the width of the room are L and W respectively. Here it should be mentioned that, for the data transmission we only use the red color. The exact positions of the LED lamps, which actually are our transmitters, on the ceiling are LED1(0,0,h), LED2(L,0,h), LED3(0,W,h), LED4(L,W,h), where the values are measured in meters.

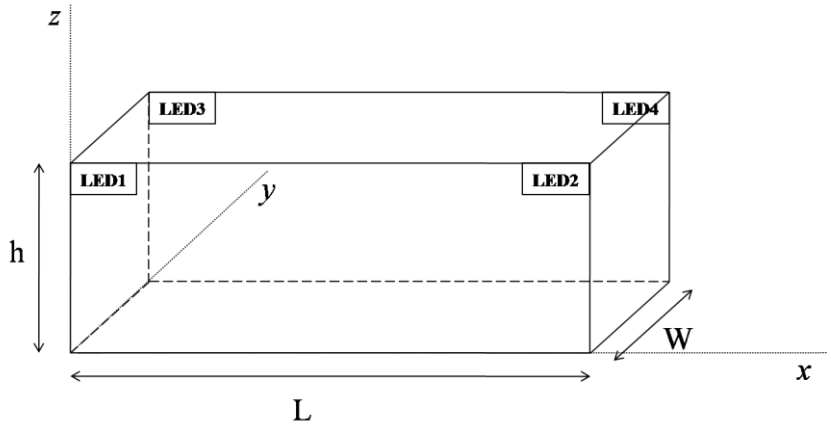

FIGURE 1: Room Dimensions and LED installation

The photodiode is supposed to be able for the reception of a wide range of wavelengths, [1], while the order of emission of each transmitter, is assumed to be Lambertian, m, and is determined as, [10], [13]:

$$m = -\frac{\ln 2}{\ln[\cos(\varphi_s)]} \tag{1}$$

where φ_s is the semi-angle at half power. Furthermore, in a direct optical link the DC gain of the channel is given as, [1], [10], [13]:

$$H_0 = A\frac{m+1}{2\pi d^2}\cos^m(\varphi)T_s(\psi)\cos(\psi)g(\psi) \text{ for } 0 \le \psi \le \psi_c \tag{2}$$

where A represents the physical area of the photodiode of the detector, d is the distance between transmitter and receiver, while φ and ψ are the angle of incidence and normalized irradiance respectively. Parameter $T_s(\psi)$ stands for the gain of an optical filter and ψ_c for the width of field of view (FOV) at the photodiode of the receiver. Finally, $g(\psi)$ is the gain of an optical concentrator which defined as, [2], [10], [13]:

$$g(\psi) = \frac{n^2}{\sin^2(\psi)} \text{ for } 0 \le \psi \le \psi_c \tag{3}$$

where n is the refractive index of the medium. In the case where $\psi \ge \psi_c$, both H_0 and $g(\psi)$ are zero. Considering P_t as the optical power of the transmitter, the power in the receiver side is given as, [10], [13], [14]:

$$P_r = P_t A\frac{m+1}{2\pi d^2}\cos^m(\varphi)T_s(\psi)\cos(\psi)g(\psi) \tag{4}$$

A typical emission pattern of a LED transmitter according to Lambertian model is shown in Fig. 2:

ISSN:1791-4469

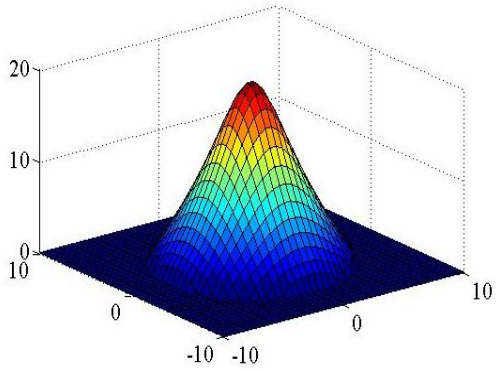

FIGURE 2: 3-D emission pattern

The modulation that will be used in this work is the eSSK technique that is very effective and widely used. Applying this modulation, each transmitter has a different and unique width of the emitted pulse, while the amplitude remains the same. Hence, the pulse width of the transmitted signal is the identity of each LED lamp, [2], [10]. At the same time the width of the transmitted pulse is different and unique for each transmitter and the pulse duration of the transmitted symbol is $\tau_i T$ where i indicates each different transmitter that symbol comes from and T is the duration T of the transmitted pulse and the received signal is expressed as:

$$r(t) = \gamma H(t) * x(\mathrm{t}) + \mathrm{n(t)} \tag{5}$$

where "*" represents the convolution between **H(t)** and **x(t)**, γ is the responsivity of the receiver, **H(t)** is the channel gain, **x(t)** is the matrix of transmitted signal and **n(t)** is the matrix of the Additive White Gaussian Noise (AWGN). The channel gain for a system with 4 transmitters and 1 receiver will be given as:

$$H(\mathrm{t}) = \begin{bmatrix} h_{11} & h_{21} & h_{31} & h_{41} \end{bmatrix} \tag{6}$$

So by using 4 transmitters, the following symbols may be generated as: LED1(00), LED2(01), LED3(10), LED4(11).

III. SNR AND COVERAGE AREA

A. Coverage Area

There is a threshold value for the optical power that can be detected in every photodiode. Hence, if the received optical power of each LED lamp is above this threshold, the system will be efficient. Otherwise, if the received optical power of each LED lamp is below this threshold, the user will not be able receive certain symbols and as a result the performance and the efficiency of the system will be significantly deteriorated, [2]. As long as, eSSK modulation technique is used, the receiver must be able to communicate with all 4 receivers. Thus, the calculation of the area where the receiver is able to detect all the symbols is very important. The coverage area of the system is the overlapping area of all threshold circles from all LED lamps, as shown in Fig.3:

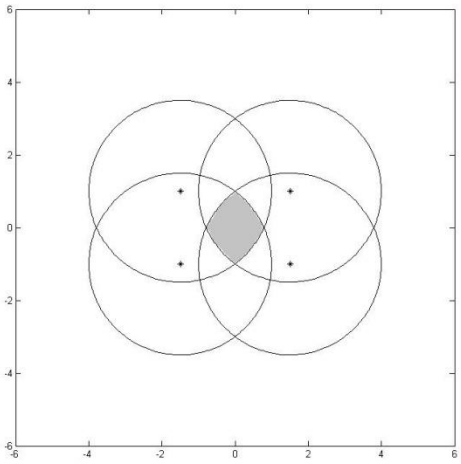

FIGURE 3: Overlapping Area of 4 LED lamps

In order to deploy an effective VLC system with eSSK, the parameters and the installing pattern of the LED transmitter must be carefully selected depending on the standard requirements of the link.

B.SNR after the application of an optical filter

In the case of eSSK modulation the SNR is given as, [7], [15]:

$$SNR = \frac{(\gamma P_t)^2}{N\sigma_{total}^2} \sum_{i=1}^{N} \tau_i \tag{7}$$

where γ represents the responsivity of the photodiode, P_t stands for the transmitted power, τ_i is the duty cycle parameter and σ_{total}^2 is the total noise variance that is given by, [1], [9], [10]:

$$\sigma_{total}^2 = \sigma_{thermal}^2 + \sigma_{shot}^2 \tag{8}$$

where $\sigma_{thermal}^2$ represents the variance of the thermal noise, which is the electronic noise generated from thermal agitation of charge carriers inside a conductor and given as [1], [9], [10]:

$$\sigma_{thermal}^2 = 8\pi nkT_k AB^2 \left[\frac{I_2}{G} + \frac{2\pi\Gamma nAI_3 B}{g_m} \right] \tag{9}$$

with k being Boltzmann's constant, G is the open loop voltage gain, T_k is the absolute temperature, A is the physical receiver area, I_2 and I_3 are noise bandwidth factors, n is the capacitance of photo detector per unit area, g_m is the transconductance and B is the noise's bandwidth. Additionally, σ_{shot}^2 represents the variance of the shot noise, which is the noise induced by ambient light and its variance is given as, [1], [9], [10]:

ISSN:1791-4469

$$\sigma_{shot}^2 = 2q\gamma P_r B + 2q\gamma P_{bg} I_2 B \quad (10)$$

with q being the electronic charge and P_{bg} is the background noise power. Assuming that the value of P_{bg} depends on the received sunlight noise, the mathematical expression is given as, [16]:

$$P_{bg} = r_{coe} E_{\det} T_0 A v^2 \quad (11)$$

where r_{coe} is the reflection coefficient, and T_0 is the peak filter transmission coefficient. For downlink communication, the receiving side, which is equipped on the exterior, is under direct exposure to sunlight and thus r_{coe} becomes equal to one. For uplink communication, the light bulbs that face toward the ground are affected by backscattering sunlight reflected from the floor's surface and thus r_{coe} = 0.1. Additionally, $E_{\det}$, which is the irradiance within the spectral range of the receiver in W/m^2, can be calculated as, [1],[16]:

$$E_{\det} = \int_{\lambda_1}^{\lambda_2} \frac{S_{peak} W(\lambda, T_B)}{\max[W(\lambda, T_B)]} d\lambda \quad (12)$$

In expression (10) λ_1 and λ_2 are the lower and upper spectral limits of the wavelength of the sunlight noise, while $W(\lambda, T_B)$ stands for the spectral irradiance of a blackbody radiation model, [1], [16]:

$$W(\lambda, T_B) = \frac{2\pi h_p c^2}{\lambda^5} \left(\frac{1}{e^{h_p c/\lambda k T_B} - 1} \right) \quad (13)$$

where h_p stands for the Planck's constant, c is the speed of light in vacuum and T_B is the average surface temperature of the Sun in Kelvin degrees. The Sun's spectral irradiance measure outside the earth's atmosphere closely resembles a blackbody of 6000°K, [1],[5]. Here, it should be mentioned that, for the calculation of the integral of expression (10), the Monte Carlo method is deployed using 1×10^6 random samples Furthermore the peak spectral irradiance in $W/m^2/\mu m$ is given as, [17]:

$$S_{peak} = 10^{-4} E_{global}^2 + 1.5768 E_{global} \quad (14)$$

with E_{global} being the global solar irradiance. The band-pass filter can be used for the reduction of the received background noise from higher and lower wavelengths, as the information of our system is transmitted by using the red light of the RGB led lamp. Such optical filters can be easily constructed using various materials, [1].

IV. BER ESTIMATION

In this section, we study the performance of our system in terms of Bit Error Rate (BER). BER is one of the most well-known and crucial metrics for the performance estimation of every communication system, [18], as it is associated with the reliability of the system and its value is strictly determined in modern communication standards. The BER expression for the eSSK modulation scheme, based on, [15], can be written as:

$$BER \le \frac{4}{N\log_2(N)(N-1)} \sum_{j=1}^{N-1} \sum_{i=j+1}^{N} Q\left(\sqrt{\left(\frac{TN}{4S} SNR\left(\| \tau_i h_i - \tau_j h_j \|_F\right)^2\right)}\right) \quad (15)$$

where $S = \sum_{i=1}^{N} \tau_i$, $h_{ij}(t)$ is the channel gain between the *i-th* transmitter and the receiver, i = 1,2,3 and 4, T is the duration of the transmitted pulses which is the same for every transmitter, N is the number of transmitters, and $\|.\|_F$ is Frobenius norm about matrices.

V. NUMERICAL RESULTS

In this section the numerical results of the indoor VLC system described above will be presented. The VLC systems is modulated with eSSK technique using 4 LED transmitters that are installed at the corners of a room with dimensions 5m x 5m x 3m. The transmitted power of each LED is 1 Watt and the semi-angle φ=85°. The receiver is placed 1.5m above the floor and has the technical characteristics presented in table (2):

Technical Characteristics of Receiver Photodiode	
Detectors Surface (A)	$8 \cdot 10^{-4} m^2$
Field of view (FOV)	*60°*
SNR threshold	*5dB*

TABLE 1: Technical characteristics of receiver Photodiode

According to these characteristics, the overlapping area in the room can be precisely calculated with Monte Carlo simulation using 10^6 random samples.

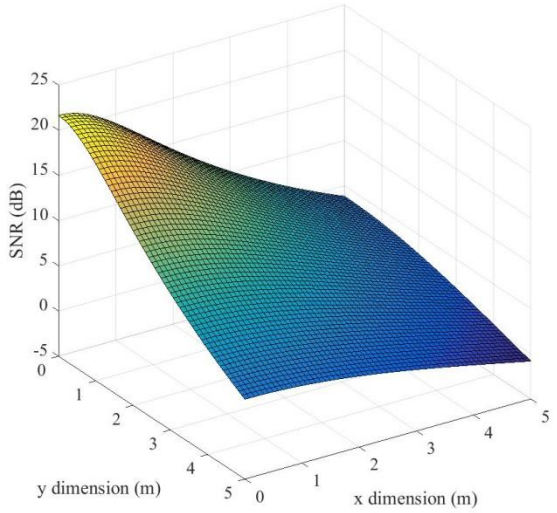

FIGURE 4: SNR of each LED in case no optical filter is applied

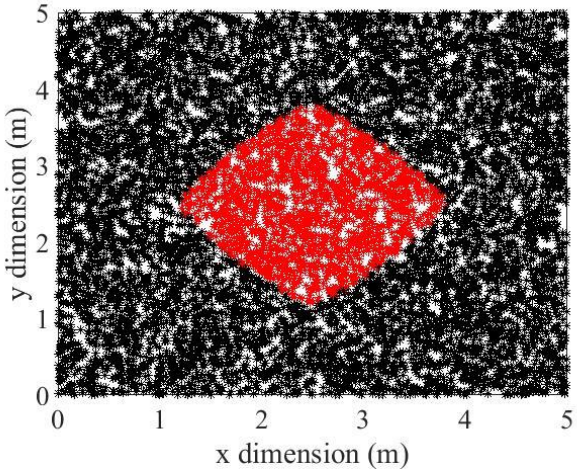

FIGURE 5: Overlapping area of VLC system in case no optical filter is applied

In figure (4) the SNR of each LED is presented. This SNR corresponds to the total SNR the at the receiver as in eSSK modulation only one LED transmits every time slot. In figure (5) the overlapping area is presented. In this area, the receiver is able to receive all 4 symbols. The maximum SNR equals 21dB while the surface of the overlapping area is $A_e=4m^2$.

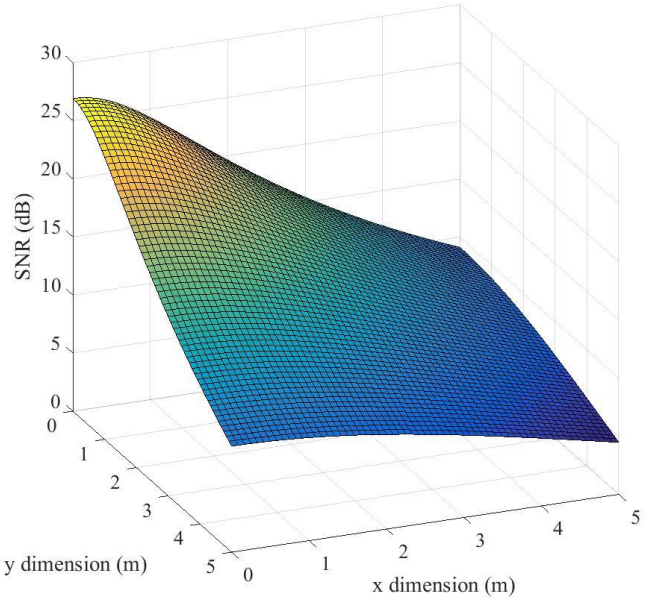

FIGURE 6: SNR of each LED using optical filter

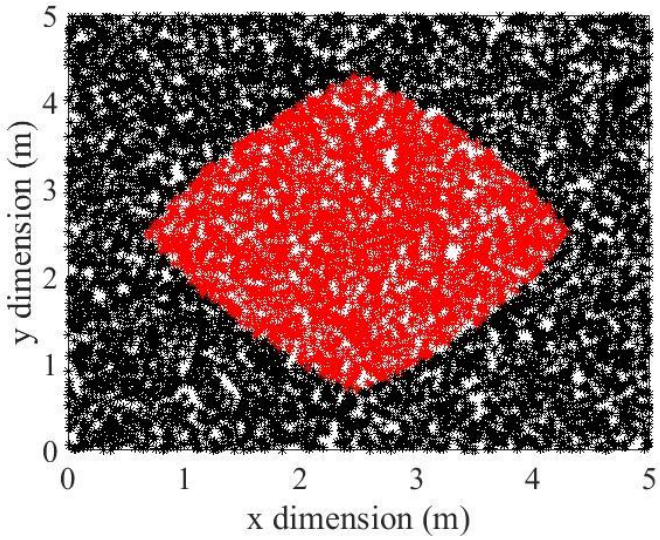

FIGURE 7: Overlapping Area using optical filter

In figures (6) and (7), an optical filter with frequencies cutoff at 600nm and 800nm, so that only red light that carries the information can pass to the receiver, is applied to the system and the corresponding results are presented. According to the results the performance of the system clearly increases as the maximum SNR is 27 dB. At the same time the availability of the system improves as the overlapping area expands by 100% with the total surface area increasing to $8m^2$.

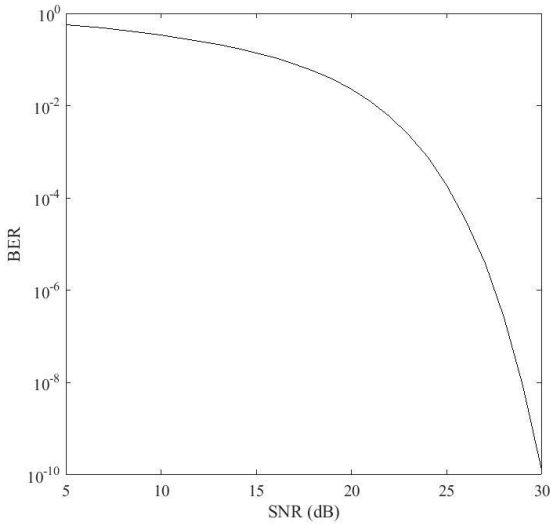

FIGURE 8: BER for the eSSK

Furthermore, the BER of the eSSK VLC link is presented in figure (8). These results corresponds to a specific point in the room where the channel gain is h=[1, 0.8, 0.6, 0.4]. It is clear that as the SNR increases, the performance of the systems increases as the BER becomes lower. More specifically, for an SNR value greater than 25 dB the system's performance becomes very reliable. So the use of the optical filter that increases the SNR, makes the system even more robust for networks that require high reliability and security. More specifically, for the values of

ISSN:1791-4469

SNR that were calculated in cases with and without filter, the BER decreases more than 4 orders of magnitude.

VI. CONCLUSIONS

In this work, the SNR performance of a VLC system using an optical bandpass filter for the deterioration of the sunlight background noise has been estimated, and the coverage area of such a system using various patterns of LED transmitters has been investigated. Additionally, the reliability of the VLC system using eSSK modulation scheme has been studied in terms of BER and the relevant closed form mathematical expression has been derived. The corresponding numerical results demonstrated that the use of an optical filter can greatly improve the performance and the availability of the VLC system, as the overlapping area expands and the BER decreases many orders of magnitude.

ACKNOWLEDGMENTS

This research is co-financed by Greece and the European Union (European Social Fund- ESF) through the Operational Programme «Human Resources Development, Education and Lifelong Learning» in the context of the project “Strengthening Human Resources Research Potential via Doctorate Research” (MIS-5000432), implemented by the State Scholarships Foundation (IKY).

REFERENCES

1. D. K. Manousou, A. N. Stassinakis, E. Syskakis, H. E. Nistazakis, G. S. Tombras, Ch. K. Volos, and A.D. Tsigopoulos, “Estimation of the influence of Vanadium Dioxide Optical Filters at the Performance of Visible Light Communication Systems,” *2018 7th Int. Conf. Mod. Circuits Syst. Technol.*, pp. 1–4, 2018.
2. S. Menounou, A. N. Stassinakis, H. E. Nistazakis, G. S. Tombras, and H. G. Sandalidis, “Coverage Area Estimation for High Performance eSSK Visible Light Communication Systems,” *2017 Panhellenic Conf. Electron. Telecommun.*, pp. 1–4, 2017.
3. S. Jayasudha, N. Bakkiyalakshmi, M. Manju, R. Sivabarani, and M. Subasridevi, “Visible Light Communications For 5g Wireless Networking Technology,” vol. 10, no. 4, pp. 390–395, 2016.
4. D. Tsonev, S. Videv, and H. Haas, “Light Fidelity (Li-Fi): Towards All-Optical Networking,” *Proc. SPIE, Vol. 9007, Broadband Access Commun. Technol. VIII; 900702, doi 10.1117/12.2044649*, no. 0, 2014.
5. H. Chun, C. J. Chiang, A. Monkman, and D. Obrien, “A study of illumination and communication using organic light emitting diodes,” *J. Light. Technol.*, vol. 31, no. 22, pp. 3511–3517, 2013.
6. D. Karunatilaka, F. Zafar, V. Kalavally, and R. Parthiban, “LED based indoor visible light communications: State of the art,” *IEEE Commun. Surv. Tutorials*, vol. 17, no. 3, pp. 1649–1678, 2015.
7. W. O. Popoola, S. Sinanovic, and H. E. Nistazakis, “Enhancing the error performance of optical SSK under correlated channel condition,” *2016 IEEE Int. Conf. Commun. Work. ICC 2016*, pp. 7–11, 2016.

8. W. O. Popoola, E. Poves, and H. Haas, "Error Performance of Generalised Space Shift Keying for Indoor Visible Light Communications," *IEEE Trans. Commun.*, vol. 61, no. 5, pp. 1968–1976, May 2013.
9. M. S. Ab-Rahman, N. I. Shuhaimi, L. A. H. Azizan, and M. R. Hassan, "Analytical study of signal-to-noise ratio for visible light communication by using single source," *J. Comput. Sci.*, vol. 8, no. 1, pp. 141–144, 2012.
10. T. Komine and M. Nakagawa, "Fundamental analysis for visible-light communication system using LED lights," *IEEE Trans. Consum. Electron.*, vol. 50, no. 1, pp. 100–107, 2004.
11. W. Lu, G. Zhao, B. Song, J. Li, X. Zhang, and G. Han, "Preparation and thermochromic properties of sol-gel-derived Zr-doped VO2films," *Surf. Coatings Technol.*, vol. 320, pp. 311–314, 2017.
12. J. Du, Y. Gao, H. Luo, Z. Zhang, L. Kang, and Z. Chen, "Formation and metal-to-insulator transition properties of VO2ZrV2O7composite films by polymer-assisted deposition," *Sol. Energy Mater. Sol. Cells*, vol. 95, no. 7, pp. 1604–1609, 2011.
13. Z. Ghassemlooy, D. Wu, M. A. Khalighi, and X. Tang, "Indoor Non-directed Optical Wireless Communications - Optimization of the Lambertian Order," *J. Electr. Comput. Eng. Innov.*, vol. 1, no. 1, pp. 1–9, 2013.
14. S. Menounou, A. N. Stassinakis, H. E. Nistazakis, A. Tzanakaki, H. G. Sandalidis, and G. S. Tombras, "Study and simulation on performance of a VLC communication system." 7th IC-EPSMSO, 2017.
15. K. N. Manganaris, H. E. Nistazakis, A. N. Stassinakis, A. Tzanakaki, G. Mkrttchian, and G. S. Tombras, "eight transmitter-short range indoor vlc systems using spatial modulation technique of enhanced ssk with variable pulse width and correlated channel conditions." 7th International Conference on "Experiments/Process/System Modeling/Simulation/Optimization" 7th IC-EPSMSO Athens, 2017.
16. H. C. Kim, B. W. Kim, and S. Y. Jung, "Performance of a wavelength hopping MC-VPPM scheme for vehicle-to-infrastructure(V2I) VLC," *Photonic Netw. Commun.*, vol. 33, no. 1, pp. 1–9, 2016.
17. D. G. Kaskaoutis, H. D. Kambezidis, S. Kumar Kharol, and K. V. S. Badarinath, "The diffuse-to-global spectral irradiance ratio as a cloud-screening technique for radiometric data," *J. Atmos. Solar-Terrestrial Phys.*, vol. 70, no. 13, pp. 1597–1606, 2008.
18. G. K. Varotsos, H. E. Nistazakis, and G. S. Tombras, "OFDM RoFSO Links with Relays Over Turbulence Channels and Nonzero Boresight Pointing Errors," vol. 12, no. 12, 2017.

ISSN:1791-4469

A Case Study on the Feasibility of RCS Measurements in a Non-Anechoic Environment Using Legacy or Inexpensive Commercial Off-The-Shelf Equipment

C. N. Vazouras, C. Bolakis, E. A. Karagianni, M. E. Fafalios and J. A. Koukos

Sector of Combat systems, Naval operations, Sea studies, Navigation, Electronics & Telecommunications, Hellenic Naval Academy, Hatzikyriakou Ave., Piraeus 18539, Greece.

Abstract. An experimental setup was built and tested for indoor measurements of Radar Cross Section (RCS) of small targets in the Hellenic Naval Academy (HNA) premises. No anechoic chamber being available, separation of the target echo from unwanted background returns was sought via the old, well-established CW-nulling (CW-cancellation) technique. A simple instrumentation system was implemented along the literature guidelines, with some handy modifications, using a general purpose scalar Spectrum Analyzer (SA) for reception. Several legacy free-floating microwave sources were tested first, achieving cancellation to a limited extent, leaving a residual signal (in the absence of target) with considerable power fluctuations, which, however, can be reduced using the averaging function of the SA. Significant improvement was achieved using an inexpensive Commercial Off-The-Shelf (COTS) phase-locked YIG oscillator which, by careful manual tuning and use of averaging, allows for a fairly stable residual return at levels within 20 dB from the trace-averaged noise floor of the receiver. Further on, calibration measurements with a conducting square plate target at normal incidence were performed, resulting in remarkably close approximation of the established canonical RCS value of the target.

Keywords: instrumentation; electromagnetic measurements; radar cross section; CW-nulling; test range; phase-locked frequency synthesizer.

INTRODUCTION

Measurement of Radar Cross Section (RCS) has been the object of extensive study since the earliest days of radar, initiated in military environments, and began to make its way into the open literature in the 1950s and early 1960s [1]. Modern state-of-the-art measurements [1, 2] usually involve time domain techniques, like gated measurements, and / or inverse FFT data processing, with a high degree of computer control and automation. Such methods require costly special-purpose instrumentation, and, in the indoor case, an appropriate test range (anechoic chamber). On the other hand, an earlier frequency-domain method (i.e. based on monochromatic measurements) may still be applied at incomparably lower cost.

ISSN:1791-4469

The objective of the present work is to examine the use of the traditional CW-nulling (or CW-cancellation) approach [1-3] with minimal cost and instrumentation requirements. To this end, some range calibration measurements were performed inside the HNA Laboratory Building using readily available legacy equipment of the HNA Telecommunications Laboratory and some inexpensive Commercial Off-The-Shelf (COTS) microwave sources in X-band frequencies. In the absence of a proper indoor test range, namely, in the words of [1], an "enclosure lined with radar absorbing materials" (i.e. an anechoic chamber), as well as time-domain instrumentation, efforts were concentrated upon minimization of the unwanted background echo (i.e. the returns from the test range in the absence of target) via the CW-nulling technique [3-5]. As is well known, the method seeks to (almost) cancel the unwanted echo by subtracting an appropriately attenuated and phase-shift portion of the incident wave. The method dates at least from the early 1950s [4, 5] and probably from the earliest applications of RCS measurements. In [2], as early as 1993, it is referred to as "obsolete", due to the emergence of swept- and stepped-frequency and time-domain (gated) instrumentation radars, greatly advantageous to speed and efficiency of measurement; as also noted therein, however, the cancellation principle is still applied in newer instrumentation systems. The CW-nulling method is also referenced in the relevant IEEE standard [1]. In short, the method seems to remain as well-established as ever, so long as one recognizes its limitations. It may also be significantly facilitated by some technological and commercial advances, such as the ones exploited in the present study:

- use of a general purpose scalar Spectrum Analyzer (SA) instead of a specialized receiver, taking advantage of its inbuilt digital processing capabilities (unheard of in the early days of the method)
- use of an inexpensive Commercial Off-The-Shelf (COTS) phase-locked frequency synthesizer unit in the X-band as a signal source, to provide the frequency stability indispensable to successful application of the method.

On the other hand, the passive framework of the instrumentation system is very simple and easy to compose, along the well-known guidelines of the literature, using legacy waveguide components. The measurement process is quite cumbersome and time-consuming (as it has always been), but this is the price to pay for the simplicity and inexpensiveness of the instrumentation used. Several preliminary range calibration tests demonstrated the feasibility of considerable reduction of the background echo, implying the possibility of obtaining reasonable RCS estimates for a variety of targets.

EXPERIMENTAL SETUP AND INSTRUMENTATION

A simple experimental instrumentation along the lines of [3-5] was used, as depicted in Fig.1.

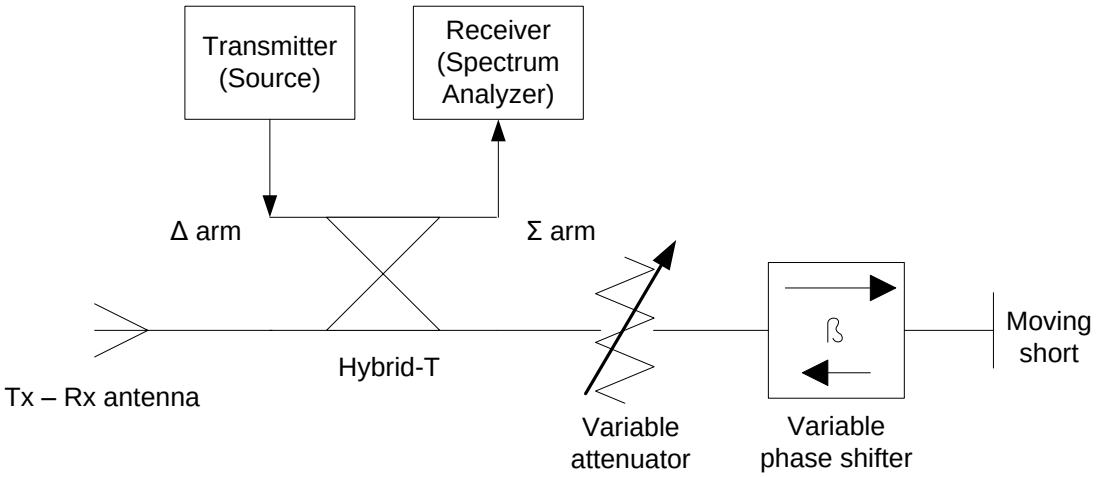

FIGURE 1. Block diagram of the measurement instrumentation.

The instrumentation is based on WR-90 rectangular waveguide parts, with the standard inner dimensions of 0.9 in (22.86 mm) × 0.4 in (10.16 mm) and the recommended frequency band of 8.2 to 12.4 GHz. Referring to Fig.1, the incident wave generated by the microwave signal source is split in halves by means of a magic-T. The first half is transmitted by the antenna, while the second half (out of phase by 180 degrees) travels towards the load via the opposite arm of the magic-T. The signal entering the receiver is proportional to the vector sum of the echo received by the same antenna and the internal reflected wave from the load (a small portion of the second half of the incident wave). As is well known, the CW-nulling technique is based on adjustment of the internal reflected wave to cancel out the background echo at the receiver. In the instrumentation described e.g. in [3-5], a matched load is used and adjustment is achieved by inserting some degree of mismatch by a 3-stub tuner. In the present work, a moving short was used as termination, preceded by a variable attenuator and a phase shifter, both based on the traditional construction of a vane moving across a WR-90 waveguide, with mechanical adjustment using a rotating Vernier scale. To achieve echo cancellation, one adjusts the attenuator and phase shifter to render the magnitude and phase of the internal reflected wave as near the background echo as possible, which results in minimization of the total signal observed at the SA due to the 180 degree phase difference inserted by the magic-T junction. In some cases, moving the position of the shorted termination was also found to be helpful, practically extending the range of phase difference adjustment offered by the shifter.

After testing and comparison with the 3-stub tuner arrangement, the present modified setup appears to achieve a similar or better degree of cancellation, probably due to more precise mechanical adjustment of the attenuator and phase shifter by means of the rotating Vernier. Moreover, by adjusting the attenuator to maximum (about 40 dB), the internal reflected wave is essentially eliminated (attenuated by 80 dB), and hence an estimate of the total background echo level is obtained at the receiver. The adequacy of the attenuation to effectively eliminate the reflected wave in comparison with the background echo was verified by stabilization of the signal at the receiver during the adjustment of the attenuator. Calibration of the system for frequency variation of the transmitter output power and various insertion and reflection losses of the passive components, may be achieved similarly in a simple way by replacing the antenna with a short circuit, eliminating the reflected wave by maximizing the attenuation, and measuring the signal power level at the receiver over the range of frequencies to be tested. The power

ISSN:1791-4469

variations thus obtained may be subtracted from the actual target echo power levels measured over the same frequency range, to separate the frequency dependency of the target from the one due to the instrumentation system (except the antenna) itself. This, of course, is no system calibration in its proper sense, since it does not take into account the antenna gain and free space losses; as is well known (see e.g. [2]), proper calibration may be achieved via measurements of a "canonical" target such as a conducting plate (at normal incidence) or sphere. However, it is of some interest for initial validation of the present instrumentation system and measurement approach, since it yields an estimate of the frequency behavior of the antenna and target combination, to be assessed by comparison against the expected behavior which for some types of antennas and targets is known to a good degree of accuracy. So, in the following, this procedure will be referred to as "partial calibration". Further on, setting the attenuator at maximum and replacing the antenna with a power measuring device (a power meter or a spectrum analyzer), we can measure the power fed into the input terminal of the transmitting antenna, i.e. the "available power" for transmission. To get the actual radiated power one should, of course, subtract the mismatch and antenna losses, but they will be taken into account anyway by the "full" calibration procedure. Moreover, the mismatch loss between the waveguide and the antenna is expected to be offset (to a large extent) by the mismatch loss of the waveguide to coaxial adaptor used for the power measurement, which is generally of similar magnitude (e.g., a typical SWR in the range of 1.3 - 1.6 for both). The available power thus measured may be used for comparison of the power output of the various generators tested (and for estimation of the overall system sensitivity).

The antenna used was a WR-90 based pyramidal horn with a gain of approximately 16 dB at 8.2 GHz. A general purpose scalar SA, namely the NS-265 model made by Nex1, was used as receiver. It covers the frequency range 9 kHz – 26.5 GHz, with an amplitude measurement range down to – 110 dBm, an average displayed noise level of – 110 dBm or less, and a frequency flatness of ± 2.2 dBm at the frequency band of interest (8-10 GHz). Thus, it offers a good (albeit not exceptional) sensitivity and frequency behavior. An input SWR up to 1.5 with an inbuilt 2.92 mm socket is given in the specifications. Our instrument has an inbuilt 7 mm (APC-7) socket (known to outperform the 2.92 mm one in terms of SWR) with an additional N-type adaptor (socket saver); assuming for it a maximum SWR value of 1.3 (typical for good quality N-type connectors), we estimate an overall maximum SWR of about 1.6 for the combination (corresponding to a power reflection coefficient about 0.057 or a mismatch loss of about 0.25 dB). As is typical of most SAs, the accuracy of absolute power measurements is poor (no error limits are even specified by the manufacturer), but comparative results, such as power ratio measurements, are much more reliable. As has already been mentioned, RCS measurements are usually based on such results, deriving absolute RCS values by comparison with measurements of some appropriate "canonical" target. Thus, in the present study, the SA was used to measure received power using the "channel power measurement" function; as it will be seen in the following, only power ratios (in dB) are used for RCS estimation at each frequency. An "adjacent channel power measurement" function is also provided by the SA, measuring power level differences between adjacent frequency ranges (channels), and was used to estimate the distance (in dB) between the received signal level and the corresponding noise floor, as an indication of the achievable dynamic range; to this end, the adjacent channels were set to equal frequency widths (integration bandwidths), located so as to ensure that the received signal lies fully in the first (main) channel and no part of it overlaps with the second (adjacent) channel. To reduce noise, the RF input attenuation was set to zero and the average detection mode was used.

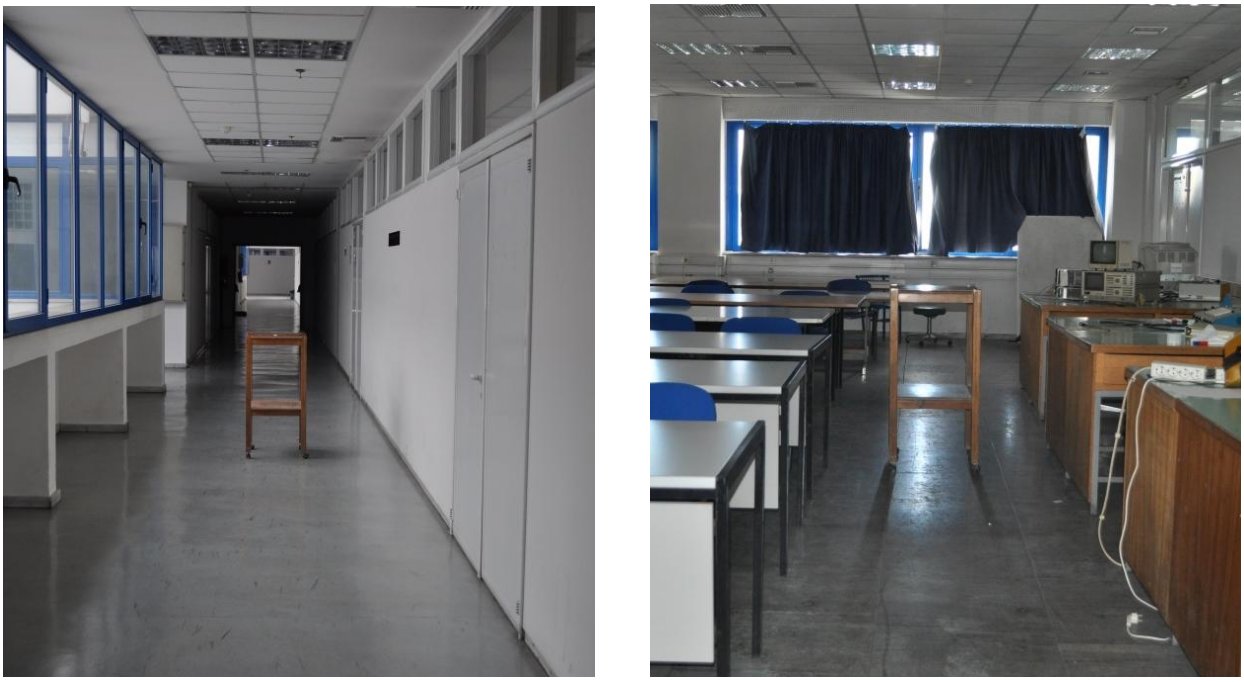

(a) **(b)**

FIGURE 2. Test site view: (a) corridor (b) classroom.

In the absence of a proper indoor test range, i.e., in the words of [1], an "enclosure lined with radar absorbing materials", test measurements were carried out in two indoor sites inside the HNA Laboratory Building: (a) a lengthy corridor (in all about 65 m long, 2.5 m wide and 3 m high), (b) the classroom used by the Telecommunications Laboratory for laboratory exercises and theory lectures (a 15 by 10 by 3 m room, full of furniture and lab equipment). A site view is depicted in Fig. 2. No modification to the usual layout of the sites was made before the test measurements. Both sites, especially the second one, exhibit strong unwanted returns, as expected and verified by the test results. This, in turn, results in serious limitation of the dynamic range and increased uncertainty of measurements. Still, with an appropriate signal source, some useful results may be drawn, as will be seen in the following.

Several microwave signal sources were tested, namely:

1) A legacy reflex klystron tube (Raytheon 2K25) oscillator, with an output power typically at 20 – 40 mW (according to various datasheets). Its operating frequency lies between 8.5 – 9.66 GHz, mechanically adjustable by varying the size of the cavity, and electronically adjustable (about 50 MHz around a mechanically adjusted center frequency) by varying the reflector voltage. Voltage feed was provided by a (quite old but recently refurbished and tested) Mid-Century EE/2 power supply. Its reflector voltage ripple does not exceed 3 mV; for the klystron mode used, the frequency shift by reflector voltage is typically around 2-3 MHz per volt, according to the tube specifications, and hence the resulting frequency variation will not exceed a few kHz. The frequency variation due to temperature changes, typically up to about 200 kHz per °C of tube temperature, appears to be a much more important source of frequency fluctuations. A WR-90 isolator with an insertion loss of up to 1.5 dB was used at the tube output for extra frequency stability.

ISSN:1791-4469

2) An old but still fully functional HP 620B (reflex klystron based) microwave signal generator. It operates in the frequency range of 7 – 11 GHz, manually adjustable, with an output power rating at 1 mW minimum. Its typical frequency stability is less than 0.006% per °C of ambient temperature and less than 0.02 % for a 10% line voltage change. A waveguide to coaxial adaptor was used at the generator's N-type output.
3) A custom Dielectric Resonator Oscillator (DRO) module built from an extremely inexpensive commercial motion sensor unit, at 10.396 GHz, with a power output of approximately 5 mW measured at the N-type output connector. Limited (about 100 MHz) mechanical tuning is possible but not used here.
4) A phase-locked commercial (obtained via surplus sales) frequency synthesizer using an Yttrium Iron Garnet (YIG) tuned oscillator (YTO) unit, namely a Stellex/Endwave MiniYIG 6755-726F unit, attached to a phase-locking controller module by the same provider. The YTO unit is (as all YTOs) electronically adjustable by current tuning, typically up to a recommended value of ± 200 mA with a 5 MHz/mA sensitivity, i.e. within a ± 1 GHz frequency range. The center frequency (with zero tuning current) is 9.11 GHz and the power output between 11 – 12 dBm in the 8.1 – 10.1 GHz frequency range, both measured in free-floating mode (without the synthesizer board). In phase-locked mode (with the synthesizer board) the output is programmable at 1 MHz steps, with a power output within 5 – 6 dBm in the above frequency range. The synthesizer module was programmed via serial interface using a Windows PC, according to the instructions found in [6] and [7]; successful locking was verified using the SA. The YTO unit was also tested alone (in free-floating mode) as a signal source, but found to exhibit large short-term frequency fluctuations, similar to the other free-floating sources used (or even larger), attributable to the large temperature drift[1] inherent in the unit (typically ± 30 MHz and up to ± 60 MHz). Hence, further such testing was considered uninteresting and not pursued.

All sources were kept idle for an interval of 30 minutes after turn-on, prior to any testing, to allow for temperature stabilization.

RESULTS AND DISCUSSION

As a first step, testing was carried out for the microwave signal sources (1) – (4) discussed above. For each one of the sources, using the instrumentation setup described in the previous section, the CW-nulling adjustment procedure with no target present was performed, and the received signal, i.e. the residual signal after nulling adjustment, monitored on the SA. A well-known type of instability was exhibited, namely temporal fluctuations of the residual signal power, due to temporal fluctuations of the center frequency of the source, varying substantially across the various sources tested. It was observed, however, that after initial thermal stabilization, there is no significant short-term drift and the frequency fluctuations tend to occur around a more or less stable center frequency. Thus, use can be made of the trace averaging function of the SA in combination with the adjacent channel power measurement function (an example is shown in Fig. 3), to gradually average out the power fluctuations. A significant stabilization of the residual

[1] The term "frequency drift" generally means a systematic (non-random) change of frequency with time. In the context of the YTO unit datasheet, however, it denotes just the overall frequency variation with temperature. If the temperature fluctuates, such variations will be observed as temporal fluctuations of the free-floating YTO frequency.

power measurement was thus achieved, depending upon the number of terms (subsequent sweeps) averaged; with 100 or more terms, the power indication was stabilized to within ± 1 dB of a mean value, taken as the observed value of the residual signal power. The repeatability of the results at time intervals of several minutes was not perfect, ranging within 1 – 2 dB from the previous value for the phase-locked YTO and 3 – 4 dB for the rest of the sources. Such deviations contribute to the uncertainty of target echo measurements, and in practice, with test target echoes at about 30 dB (or more) above the residual power level, as it will be seen in the following, the impact is limited.

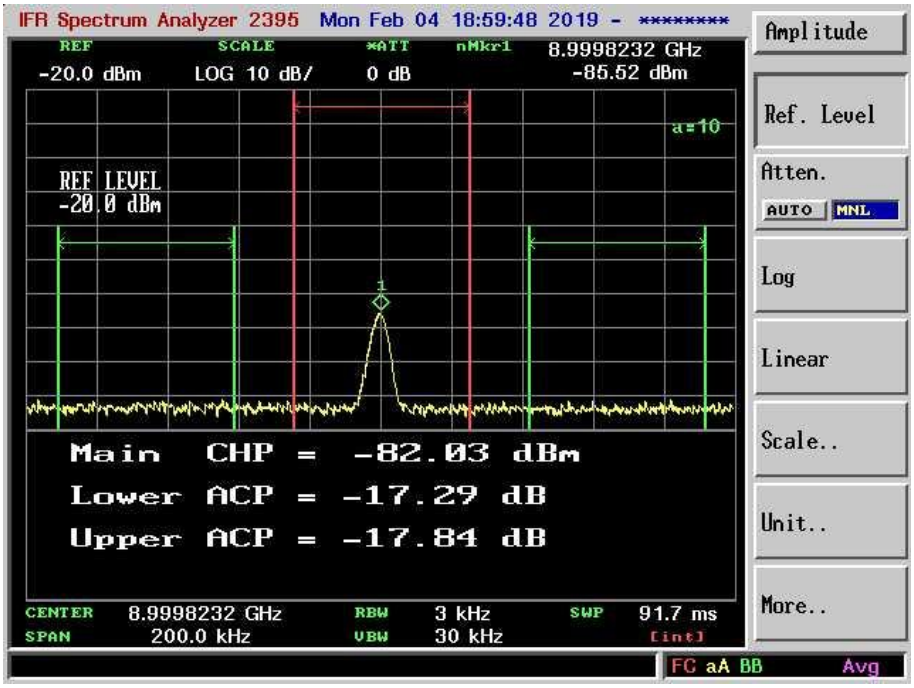

FIGURE 3. A spectral view of the residual signal with the phase-locked YTO source.

Upon inspection of the signal power spectrum, some features of each source were deduced:

- The phase-locked YTO source provides, as expected, the best signal in terms both of bandwidth (or, otherwise stated, phase noise) and of fluctuations. A 100 kHz frequency span was used for adjacent channel power measurements, with the default values (automatically adjusted by the SA) of 3 kHz for the resolution bandwidth (RBW) and 30 kHz for the video bandwidth (VBW). The indication of the signal's 20-dB bandwidth with this RBW was approximately 10 kHz. Upon reduction of the RBW it diminishes, in accordance with the measured results shown in [6] and the phase noise specifications of the YTO. However, a smaller RBW value was not adopted, partly to avoid large sweep times and partly because, with a finer RBW, the inherent limitations of the onboard reference temperature compensated voltage controlled crystal oscillator (TCVCXO) of the synthesizer (noticed in [6]) are expected to become apparent, exhibiting smaller-scale frequency instabilities which would complicate the measuring process without significantly altering the averaged results. With the RBW used, the short-term frequency fluctuations within the time required for trace averaging were almost invisible. At significantly larger time intervals, a slower fluctuation up to about ± 50 KHz around the

ISSN:1791-4469

center frequency was sometimes observed; it might be attributed to small frequency instabilities of the reference TCVCXO and / or small temperature fluctuations in the YTO. It was generally not fast enough to disrupt the averaging process, but in some cases required repetition of the nulling adjustment before target echo measurement.

- The HP 620B signal generator exhibits significant frequency fluctuations of about ± 100 kHz around the center frequency. A 1 MHz frequency span was adopted for the SA measurements, with the default values of 10 kHz RBW and 100 kHz VBW. The indication of 20-dB signal bandwidth with this RBS is near 50 kHz.
- The 2K25 reflex klystron oscillator exhibits the strongest frequency fluctuations, up to about ± 500 KHz around the center frequency, and correspondingly strong residual power fluctuations. The frequency span of the SA was set to 5 MHz, with the corresponding default values of 30 kHz RBW and 300 kHz VBW, and the 20-dB signal bandwidth indication was also inferior to the previous source, of the order of 250 kHz or so; in both cases, precise observation of the 20-dB bandwidth was difficult due to frequency fluctuations.
- The DRO oscillator exhibits smaller frequency fluctuations of about ± 50 KHz around the center frequency, but a very large phase noise. With a 5 MHz frequency span setting, as above, the 20-dB signal bandwidth is indicated at about 2 MHz; we believe it to be the main reason for the inferior performance observed for this source, as will be seen presently.

Besides the residual return signal, the background echo power and the available power for transmission were also measured in the manner described previously. Due to much larger values and the very nature of these quantities, no significant instability problem was encountered. The results for the worst-case classroom site are shown on Table 1. The 1 dB compression point of the SA is at – 10 dBm, indicating that all measurements are well within the dynamic range of the instrument; the same is true of measurements presented in the following.

TABLE 1. CW-nulling adjustment test results for various microwave signal sources

Microwave Signal Source	**Frequency (GHz)**	**(1) Residual Power After Nulling (dBm)**	**(2) Background Echo (dBm)**	**(3) Available Power (dBm)**	**Margin (dB) (3) – (1)**
2K25 reflex klystron	9.000	– 72	– 23.5	– 1.5	70.5
HP 620B generator	9.000	– 80	– 47	– 16	64
DRO module	10.396	– 66	– 51	– 9.2	56.8
Phase-locked YTO synthesizer	9.000	– 82	– 34.5	– 4	78

For the corridor site, similar tests were also performed, yielding consistently improved (i.e. lower) values of background echo power by 4 – 5 dB, and of residual signal power by 2 – 3 dB. The improvement may be attributed to the length of the corridor, as well as the absence of diverse scatterers like furniture and equipment. Thus, calibration measurements with a canonical target, as will be presented in the following, were carried out in the corridor site.

The margin between the available power and the residual power, essentially the quantity defined in [3] (Sec. 11.5.1.1) as isolation between transmitter and receiver, may be used for comparison of the "nulling efficiency" of the various sources. The value achieved with the YTO

source seems remarkably good, especially in the corridor site (cf. Table 2 below), even though it still falls short of the order of 100 dB recommended in [3] for accurate measurement of target nulls. On the other hand, the background echo power obviously gives an indication of the noisiness of the test site's environment, corresponding to each source; different sources resulted in different levels of background echo. A more clear comparison could also use the margin between the background echo power and the available power level. Both figures of merit may seem somewhat superfluous in the present case, since the superiority of the phase-locked YTO source is already clear from the preceding discussion (and actually was expected from the beginning), but provide some additional quantitative insight.

We finally note that a wooden table (visible on Fig. 2) was used as a handy bearing, and found to increase the background echo by approximately 0.5 dB, but with a negligible effect on the residual power, i.e. successfully eliminated by the nulling adjustment. For future RCS measurements, construction of a polystyrene foam bearing with a simple positioning setup is envisaged.

Following the preliminary tests described above, a series of target return power measurements were carried out in the corridor site, using the YTO synthesizer, within a frequency range of 8.4 – 9.6 GHz. The target was a square aluminum plate of 30.5 × 30.5 cm dimensions, located at a distance of 6 m, at normal incidence. As is well known [2], such a plate may serve as an appropriate calibration target, with an RCS value known to a good degree of accuracy, given by the physical optics approach (see e.g. [2], eq. 5.22)

$$\sigma = 4\pi \frac{A^2}{\lambda^2} \tag{1}$$

where A is the physical area of the plate, i.e. $A = d^2$ for a square plate, with d the side length.

In the case of measuring the RCS of a practical target, these would be the calibration measurements, taken as reference values to comparatively estimate the RCS of the target of interest. In the scope of the present study, however, our goal is to assess the possibility of estimating the known RCS value of the square plate target via measurements by the present instrumentation in rather unfavorable conditions. To this end, the corresponding "partial calibration" procedure (as defined previously) was employed, and the signal power $P_{c,meas}$ at the receiver upon replacing the horn antenna with a waveguide short was measured besides the actual return power at all frequencies involved. We also denote

- the power output of the signal source by P_s
- the available power for transmission (as defined previously), i.e. approximately the power fed to the terminal of the transmitting antenna, by P_t
- the echo power inwards at the same point, now viewed as the output of the receiving antenna, i.e. the power extracted from the terminal of the receiving antenna, by P_r
- the return power measured at the receiver by $P_{r,meas}$

The measurement results (in dBm) are tabulated in Table 2. In all cases, the residual return power levels were no more than 20 dB above the trace-averaged noise floor of the receiver (as indicated by the adjacent channel power measurement of the SA). It is worth noticing that levels of return power significantly below the background echo levels are easily detected and measured, of course due to the low levels of residual power achieved by the nulling adjustment.

ISSN:1791-4469

TABLE 2. Measurement results for a square plate target (all powers in dBm)

Frequency (GHz)	Residual Power	Background Echo	$P_{r,meas}$	$P_{c,meas}$
8.4	– 88	– 47	– 55.5	– 12.3
8.6	– 90	– 51	– 54.5	– 12.7
8.8	– 85	– 37	– 52	– 10.7
9.0	– 85	– 39	– 53.5	– 10.3
9.2	– 87	– 36.5	– 53.5	– 13.1
9.4	– 92	– 35	– 51	– 13.3
9.6	– 85	– 41.5	– 52	– 13.3

Since the reflection coefficient of the waveguide short equals 1 to a good degree of accuracy, it may be safely assumed that, upon replacing the horn antenna with a waveguide short, the power P_t is totally reflected inwards and we can write

$$P_{c,meas} = P_t - L \tag{2}$$

$$P_{r,meas} = P_r - L \tag{3}$$

where all powers are in dBm and L (in dB) is the total loss along the signal path from the output of the receiving antenna to the receiver (including insertion and reflection losses of the components involved, the impact of power splitting by the hybrid-T etc.)

From (2) – (3) it follows that

$$P_r - P_t = P_{r,meas} - P_{c,meas} \tag{4}$$

Eq. (4) allows estimation of the difference between P_r and P_t via the difference between the measured quantities $P_{r,meas}$ and $P_{c,meas}$, which incorporate the corresponding internal losses of the instrumentation. On the other hand, P_r and P_t are related via the radar range equation (see e.g. [2]), which, with the same antenna for transmission and reception, in its simplest form is

$$P'_r = P'_t \frac{G^2 \lambda^2 \sigma}{(4\pi)^3 R^4} \tag{5}$$

or, in logarithmic form

$$P'_r - P'_t = 2G + \sigma + 20\log\left(\lambda / R^2\right) - 30\log(4\pi) \tag{6}$$

In (5-6), the primed quantities denote the transmitted and received power at the horn antenna, after mismatch loss (both for transmission and reception) at the antenna terminal. To account for this loss, denoted by L_A (in dB), we write

$$P'_t = P_t - L_A \tag{7}$$

$$P_r = P'_r - L_A \tag{8}$$

and hence

$$P'_r - P'_t = P_r - P_t + 2L_A = P_{r,meas} - P_{c,meas} + 2L_A \tag{9}$$

Upon combining (4) and (9), the experimental RCS of the target is estimated via

$$\sigma = P_{r,meas} - P_{c,meas} + 2L_A - 2G - 20\log\left(\lambda / R^2\right) + 30\log(4\pi) \tag{10}$$

where the power values are in dBm, the transmitting and receiving antenna gain G is in dB, R and λ are in meters and σ is in dBsm (dB square meters). For the gain G, a typical variation of roughly 0.6 dB per GHz across the X-band frequencies (as e.g. in [8], Sec. 13.4) was used. For the mismatch loss L_A , a reasonable estimate may be obtained by a SWR value of 1.3. For WR-90 waveguide horn antennas with a waveguide to coax adaptor, maximum values of SWR at 1.3 or less (e.g.1.25) according to datasheets are not unusual; in our setup, no waveguide to coax

adaptor (which tends to increase mismatch losses) is present. Thus, with an antenna SWR = 1.3, the corresponding mismatch losses are 2 $L_A \cong 0.15$ dB.

As regards the measurement uncertainty, a simple and rough estimate may be obtained based on the observation that the procedure described here is essentially a power ratio measurement, as is also apparent in (10). Both power measurements involved ($P_{r,meas}$ and $P_{c,meas}$) were carried out at the same frequency and with the same configuration of the measuring instrument (the SA). Thus, most instrumentation uncertainties do not affect the total uncertainty, while others (such as the ± half-count error) are significantly small in magnitude, as noted e.g. in [9, 10]. Further on, as also discussed and visualized in these classical references, the largest source of uncertainties is by far the mismatch uncertainties, due to generator and load mismatches along the signal path. In our instrumentation setup, reasonable estimates for these mismatches, as mentioned previously, are:

- Load SWR $\cong 1.6 \Rightarrow$ Load reflection coefficient $\rho_L \cong 0.23$ (as discussed for the SA)
- Generator SWR $\cong 1.5 \Rightarrow$ Generator reflection coefficient $\rho_g \cong 0.2$ (a conservative estimate for the waveguide to coaxial adaptor used to connect the YTO generator)

In a simplistic first approach, we may use the (rather conservative) traditional worst-case approach outlined in [9, 10], while neglecting possible instrumentation uncertainties for the quantity ($P_{r,meas} - P_{c,meas}$) and focusing on mismatch uncertainties. A more rigorous and detailed examination and statistical treatment along the guidelines of ISO 17025 (as outlined e.g. in [10]) is envisaged for future test measurements. Further sources of error, besides mismatch uncertainties, include

- the antenna gain G
- the residual unwanted echo power, say P_{res} , after CW-nulling
- the mismatch loss L_A

All of the above factors correspond to the traditionally termed "systematic" errors; a "random" error component should be added. (In ISO 17025 terms, these two concepts are replaced by "Type B" and "Type A" uncertainties, but with no strict correspondence meant.)

For the mismatch uncertainties, the uncertainty boundaries are given by

$$M_{u,max} = 10\log\left(1+\rho_g\rho_L\right)^2 \cong 0.39\,\text{dB} \quad (11)$$

$$M_{u,min} = 10\log\left(1-\rho_g\rho_L\right)^2 \cong -0.21\,\text{dB} \quad (12)$$

The above uncertainty contributions must be doubled, since two power measurements are involved, amounting to a total +0.78 to –0.42 dB contribution.

The uncertainty in the antenna gain G turns out to be quite important, since this (lacking a calibrated reference antenna) was obtained by two power measurements using a HP 432A power meter with a HP 8478B thermistor mount. The measurement conditions are close to these adopted for the detailed example given in [9] and [10], minus the reference oscillator error (not existing for the thermistor sensor) which is approximately offset by the larger instrumentation error margin of the HP432A (±1% instead of ±0.5% full-scale). We also adopt a more conservative estimate for the load mismatch loss, using the maximum SWR = 1.35 of the sensor specifications, instead of the typical one of about 1.15 at the frequency of interest or the 1.2 value used in the example. This results in an increase of about 0.1 dB in the mismatch uncertainty margins with regard to the example values; in all, following the example of [9,10] with these modifications and rounding up to first digit, we obtain a worst-case uncertainty estimate of approximately ±0.5 dB for each power measurement, i.e. a total of ±1 dB for the antenna gain G.

ISSN:1791-4469

The residual echo power after nulling, as already noted, adds directly to the total uncertainty, since there is no phase correlation with the wanted return signal. Denoting it by P_{res} , the upper and lower error bound due to this term may be written as

$$R_{u,max/min} = 10\log\left(1 \pm \frac{P_{res}}{P_{r,meas}}\right) \quad (13)$$

As seen in Table 2, the largest (worst-case) value of P_{res} is about 31.5 dB below the corresponding measured return power $P_{r,meas}$, which yields a very small R_u contribution of ±0.0031 dB. (Even a residual value at 20 dB below $P_{r,meas}$ would give only about ±0.044 dB).

Further on, the uncertainty contribution from L_A may be neglected due to the small value of L_A itself; in other words, it is covered by the value of generator SWR ≅ 1.5 adopted here.

Finally, the "random" error component may be estimated at roughly ±1 dB, since this was the range of fluctuations of the power indication around its mean (measured) value, as noted previously.

Adding up the above contributions and rounding up to first digit, a total worst-case uncertainty estimate of approximately +2.8 to –2.5 dB is obtained. An additional (not accounted for) source of errors is the antenna – target misalignment (deviation from normal incidence), possibly in the range of several degrees (due to manual alignment), even though before every measurement an alignment of the target was carried out to the position maximizing the received signal.

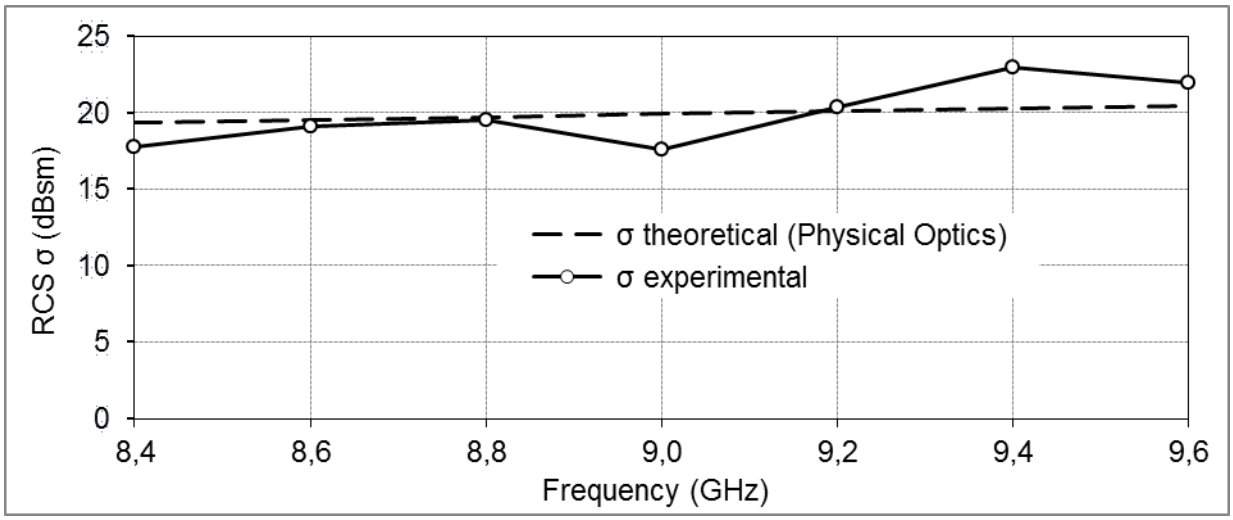

FIGURE 4. Comparison of theoretical and measured RCS values for the square plate target.

Based on the above considerations, the experimental RCS values from (7) are depicted in Fig. 4, along with the corresponding theoretical (physical optics) values given by (1).

A noteworthy agreement between experimental and theoretical RCS values is thus achieved, the discrepancy being about +2.7 dB at worst. In particular, the experimental RCS values appear consistent with the well-known upward trend of the theoretical RCS values with frequency.

CONCLUSIONS

Application of the CW-nulling technique was tested in an unfavorable non-anechoic environment, using simple waveguide equipment, a general purpose scalar SA and several legacy

or COTS microwave signal sources, for frequencies in the X-band. A very inexpensive phase-locked YTO source was found adequate to achieve low levels of residual echo power after nulling, within 20 dB of the system noise floor, and corresponding levels of isolation between transmitter and receiver between 80 and 90 dB (depending on the test frequency). The average detection mode and the trace averaging function of the SA were helpful to reducing the residual echo. Further calibration measurements, with a conducting square plate target at normal incidence, allowed simple and straightforward estimation / verification of its RCS within 3 dB of the accepted physical optics values across the whole range of frequencies tested, even though the unwanted background echo signal was well above the wanted target return.

Notwithstanding limitations of the dynamic range and the uncertainty of measurements, these findings suggest the possibility of obtaining reasonable RCS estimates (probably with the exception of directions around target nulls) for a variety of targets, provided the target return levels are adequately high and, of course, the target dimensions are appropriate for the indoor test range and meet the far-field criterion. Further canonical target geometries could be studied this way. Larger targets could also be tested at appropriate frequencies via the dimensional scaling technique. Use of the present instrumentation for outdoor range measurements might also be explored by appropriate modifications (such as adding an output amplifier unit etc.) In such a scenario, results of previous computational work to model complex targets [11] might be considered for comparison purposes.

Several prospective improvements to the experimental setup and instrumentation are of interest and may be achieved at relatively low cost, notably replacement of the phase-locked YTO with an even stabler synthesized source (or just substitution of the onboard reference TCVCXO with a higher quality one), as well as background echo reduction by even a limited quantity of absorbers inserted into carefully selected locations within the test range.

REFERENCES

1. *IEEE Recommended Practice for Radar Cross-Section Test Procedures*, IEEE Std 1502-2007, IEEE Antennas and Propagation Society, 2007.
2. E.F. Knott, *Radar Cross Section Measurements*, Van Nostrand Reinhold, 1993.
3. G.T. Ruck, D.E. Barrick, W.D. Stuart, C.K. Krichbaum, *Radar Cross Section Handbook*, Plenum Press, 1970.
4. R.G. Kouyoumjian, "The Calculation of the Echo Areas of Perfectly Conducting Objects by the Variational Method", Ph.D. Dissertation, Ohio State University, 1953.
5. J.N. Hines and T.E. Tice, "On Investigation of Reflection Measuring Equipment", Antenna Laboratory, Ohio State University, Report No. 478-13, 1953.
6. http://www.ke5fx.com/stellex.htm
7. https://www.qsl.net/ct1dmk/stellex.html
8. C.A. Balanis, *Antenna theory: analysis and design*, 2nd ed., John Wiley & Sons, 1997.
9. *Fundamentals of RF and Microwave Power Measurements*, Application Note 64-1, Hewlett Packard Co., 1977 (revised 1978).
10. *Fundamentals of RF and Microwave Power Measurements*, Application Note 64-1C, Agilent Technologies Co., 2001.
11. P. Frangos, E. Boulougouris, S. Pintzos and I. Aliferis, "Calculation of the Radar Cross Section of complex radar targets using high frequency electromagnetic techniques", International Conference on Electromagnetics in Advanced Applications (ICEAA '99), September 13 - 17, 1999, Torino, Italy.

ISSN:1791-4469

BLER of SIMO FSO Systems over Saturated Turbulence Channels and Pointing Errors

A.N. Stassinakis[a*] and G.D. Roumelas[a]

[a]*Department of Electronics, Computers, Telecommunications and Control, Faculty of Physics, National and Kapodistrian University of Athens, Athens, 15784, Greece,*
emails: {a-stasinakis; groumelas}@phys.uoa.gr
**Corresponding Author*

Abstract. During the last years, terrestrial free space optical (FSO) systems have attracted great commercial and research interest as they offer license-free and very high bandwidth access characteristics with very low installation and operational cost. Their successful presence in demanding applications and networks, such as real-time Military Theater of Operations, can guarantee high performance and security for naval applications e.g. communications in shipyard between fixed or mobile transceivers. On the other hand, weather conditions and atmospheric turbulence affect significantly the propagation of the laser beam that transmits the information, deteriorating the performance of the FSO system. Additionally, another factor that decreases the performance of such systems is the pointing errors due to the misalignment between the receiver and the transmitter. Both turbulence and pointing errors are responsible for fast and intensive power fluctuations at the receiver i.e. the scintillation effect, so the optical channel can be investigated statistically and modelled accurately through various statistical distribution models depending on the effects' strength. Thus, for saturated turbulence, negative exponential statistical distribution can be used in order to model the channel precisely. To overcome the system's degradation that is caused by turbulence and pointing errors, various techniques have been proposed and used, with the receivers' diversity scheme being a very effective one. Thus, in this work, we investigate the effect of saturated turbulence conditions and pointing errors and how the deployment of receivers' diversity can effectively increase the performance of the system. The metric that will be investigated and is related to the performance and reliability of an FSO system is the block error rate (BLER). The specific quantity is a very significant one, especially for the very high data rate communication systems, such FSOs, because its outcome can specify the kind of coding scheme which should be used. Thus, novel, closed form mathematical expressions for the estimation of the average BLER of the system will be derived and the corresponding numerical results are presented. Furthermore, using the obtained simulation outcomes, the theoretical predictions of this work, will be verified.

Keywords: FSO communications, SIMO FSO systems, Negative exponential turbulent channel, pointing errors, spatial receiver's diversity, average BLER
PACS: 42.79.Sz

I. INTRODUCTION

Nowadays, the demand for faster and more efficient communication urges the field of telecommunications towards more modern systems. A technology with great potential, that is continuously attracting more attention is the free space optics (FSO) technology.The terrestrial FSO systems can provide very high data rates and almost unlimited bandwidth, due to the physical properties of light, while their equipment is characterized by low installation and upkeep cost and low energy consumption. They can, also, offer high security links, as a result of their line – of – sight (LoS) requirement.

However, the performance of an FSO system is affected by numerous phenomena that decrease their efficiency. A typical terrestrial FSO link consists of a laser or LED as the transmitter and a photodetector at the receiver's end. Because of the light beam propagating through the atmospheric medium, their operation depends significantly on the weather conditions. Adverse weather conditions, such as rain, snow, fog, etc. increase the absorption and scattering of the beam and hinder the stable and efficient communication between the two ends of the link. Another phenomenon, that originates from the stochastic nature of the atmosphere, is the atmospheric turbulence, which causes local variations of the refractive index of the atmosphere. These variations have a negative impact on the propagating light beam, leading to fast and random fluctuations in the irradiance of the received pulse, known as scintillations,[1]–[6].

Moreover, the FSO systems are point – to – point (PtP) links and their requirement for LoS is mandatory. Consequently, they are usually installed on top of high – rise buildings. Certain effects, such as thermal expansion, strong wind loads and weak earthquakes, can cause the sway of the buildings, resulting in misalignments of the beam from the center of the detector, also called pointing errors effect. The latter can cause, in turn, the partial collection of the transmitted power, which translates into fluctuations in the irradiance that reaches the detector and sever degradations to the performance of the communication link, [7]–[10].

A common technique used to counterbalance the degradations induced to the optical link is the receiver's diversity technique. In the case of spatial diversity, the signal is transmitted in several copies by one transmitter towards multiple receivers, creating a single – input – multiple – output (SIMO) system. Due to the fact that the same signal is detected by more than one receiver, the probability of bit errors appearing at the receiver's end is minimized and the reliability of the link is increased,[7], [11]–[14].

In the current work, the aim is to investigate the performance of a terrestrial SIMO FSO system, which operates under saturated turbulence conditions with additional pointing errors effect. In section II, the necessary statistical study of the channel will be made by analyzing the chosen statistical models and the combined probability density function (PDF) will be extracted. The combined PDF will, then, be used in section III to obtain a new closed – form formula for the average block error rate of the system, in order to evaluate its performance. Finally, in section IV, the corresponding numerical results will be presented.

II. SYSTEM AND CHANNEL MODEL

The SIMO FSO system studied in the current work is using a spatial diversity scheme, which means that the signal is transmitted from the laser or LED source (transmitter) and is detected by

K photodetectors (receivers) on the other end of the link. The optical beam is assumed to propagate horizontally between the transmitter and the receivers, through a turbulent atmospheric channel with additive white Gaussian noise (AWGN). It is, also, assumed that an intensity modulation / direct detection scheme is employed, while the channel is considered to be memoryless, stationary and ergodic. Under these assumptions, the FSO signal reaching each detector can take the form,[11]:

$$y_l = \eta_l x I_l + n_l, \qquad l = 1, 2, ..., K \tag{1}$$

where y_l is the signal arriving at the *l-th* receiver, η_l is the quantum efficiency of the detector, x is the modulated signal and n_l represents the AWGN with power spectral density σ_l^2. Parameter I_l is the normalized received irradiance and assuming that the optical pulse suffers from the independent effects of turbulence and pointing errors, it can be written as, [7], [15]:

$$I_l = I_{t,l} I_{p,l} \tag{2}$$

where $I_{t,l}$ and $I_{p,l}$ are the received irradiances at the *K-th* receiver, considering separately the degradations induced by turbulence and pointing errors, respectively.

During the propagation of the pulse, the signal is degraded by the atmospheric turbulence. In the case of strong and even saturated turbulence, the effect on the irradiance of the received pulse at the *K-th* receiver, $I_{t,l}$, can be statistically described by the negative exponential distribution, and the probability density function (PDF) is given as, [15]–[17]:

$$f_{I_{t,l}}\left(I_{t,l}\right) = \exp\left(-I_{t,l}\right) \tag{3}$$

Apart from turbulence, the other phenomenon that greatly affects the quality of the FSO link is the pointing error effect. Considering that the detector is equipped with a circular aperture of radius R and the beam reaching this aperture has a Gaussian intensity profile, [18], the irradiance collected by the detector can be approximated by the Gaussian form, [18]:

$$I_{p,l}\left(r_l\right) \approx A_{0,l} \exp\left(-\frac{2r_l^2}{w_{z,l,eq}^2}\right) \tag{4}$$

where r is the radial displacement of the footprint of the beam from the center of the detector's aperture after propagation distance z and $A_{0,l} = \left[erf\left(\upsilon_l\right)\right]^2$ is the fraction of the beam's power collected at $r_l = 0$, with υ_l given by $\upsilon_l = \left(\sqrt{\pi}R\right) / \left(\sqrt{2}w_{z,l}\right)$, while $w_{z,l}$ is the beam width and $w_{z,l,eq}$ is the equivalent beam width, defined as, [10], [18]:

$$w_{z,l,eq}^2 = w_{z,l}^2 \frac{\sqrt{\pi} erf\left(\upsilon_l\right)}{2\upsilon_l \exp\left(-\upsilon_l^2\right)} \tag{5}$$

If the vertical and horizontal parts of the displacement are modeled by independent identical Gaussian distributions, the radial displacement can be expressed by the Rayleigh distribution with PDF, [18]:

ISSN:1791-4469

$$f_{r_l}(r_l) = \frac{r_l}{\sigma_{s,l}^2} \exp\left(-\frac{r_l^2}{2\sigma_{s,l}^2}\right) \tag{6}$$

for $r>0$, where $\sigma_s^2$is the jitter variance at the receiver. Equations (4) and (6) lead to the PDF describing the normalized received irradiance, due to pointing errors, I_p as, [10], [15], [18]:

$$f_{I_{p,l}}(I_{p,l}) = \frac{g_l^2}{A_{0,l}^{g_l^2}} I_{p,l}^{g_l^2-1} \tag{7}$$

for $0 \le I_{p,l} \le A_{0,l}$. In (7), $g_l = w_{z,l,eq}/2\sigma_{s,l}$ is the ratio between the equivalent beam and the displacement standard deviation and governs the intensity of the pointing error effect, with higher values corresponding to a weaker phenomenon.

The behavior of the FSO channel can be described by combining the PDFs (2) and (7), via the formula, [7], [15]:

$$f_{I_l}(I_l) = \int f_{I_l|I_{t,l}}(I_l \mid I_{t,l})\, f_{I_{t,l}}(I_{t,l})\, dI_{t,l} \tag{8}$$

where $f_{I_l|I_{t,l}}(I_l \mid I_{t,l})$ is the conditional probability given the turbulence affected irradiance, I_t, and is calculated by, [7], [15]

$$f_{I_l|I_{t,l}}(I_l \mid I_{t,l}) = \frac{g_l^2}{A_{0,l}^{g_l^2} I_{t,l}} \left(\frac{I_l}{I_{t,l}}\right)^{g_l^2-1} \tag{9}$$

for $0 \le I_l \le A_{0,l} I_{t,l}$. The combined PDF for the studied FSO channel is obtained from (2), (7) and (9) into (8) and takes the form, [15]:

$$f_{I_l}(I_l) = \frac{g_l^2}{A_{0,l}} G_{1,2}^{2,0}\left(\frac{I_l}{A_{0,l}}\middle| \begin{matrix} g_l^2 \\ g_l^2-1,\quad 0 \end{matrix}\right) \tag{10}$$

where $G_{u,v}^{m,n}(.)$ is the Meijer function, [19]. The above equation (10) can, also, be expressed in terms of the instantaneous received signal – to – noise ratio (SNR) of the pulse at the *K-th* receiver, γ_l, as:

$$f_{\gamma_l}(\gamma_l) = \frac{g_l^4 \Gamma(g_l^2)}{2A_{0,l}\Gamma(1+g_l^2)} \left(\frac{1}{\xi_l \gamma_l}\right)^{1/2} G_{1,2}^{2,0}\left(\frac{g_l^2 \Gamma(g_l^2)}{A_{0,l}\Gamma(1+g_l^2)} \left(\frac{\gamma_l}{\xi_l}\right)^{1/2} \middle| \begin{matrix} g_l^2 \\ g_l^2-1,\quad 0 \end{matrix}\right) \tag{11}$$

where γ_l is given by, [16]:

$$\gamma_l = \frac{\eta_l^2 I_l^2}{2\sigma_l^2} \tag{12}$$

and $\xi_l$is the expected SNR at the *K-th* receiver, [16]:

$$\xi_l = \frac{\eta_l^2 \; E\; I_l}{2\sigma_l^2}^2 \tag{13}$$

with $E[I_l]$the expected value of the normalized irradiance I_l, which in the case of the studied channel is equal to:

$$E[I_l]=\frac{g_l^2\Gamma(g_l^2)}{\Gamma(1+g_l^2)} \tag{14}$$

III. AVERAGE BLER OF THE SIMO FSO SYSTEM

The estimation of the performance of the SIMO FSO system can be achieved by calculating the average block error rate (ABLER), which is the probability of more than M bit errors occurring in a block of N bits. This criterion constitutes a great indicator of the reliability of the system and the quality of the provided communication. Assuming that the system transmits the information in blocks of N bits, the probability of M errors bits reaching the receiver is expressed as,[20], [21]:

$$P(M,N;\gamma)=\sum_{m=M+1}^{N}\binom{N}{m}p^m(1-p)^{N-m} \tag{15}$$

where p is the probability of receiving a single error bit. For a SIMO system employing K receivers' diversity scheme with maximum ratio combining (MRC) and OOK modulation scheme, p is given by the following equation, [12]:

$$p=Q\left(\sqrt{\sum_{l=1}^{K}\gamma_l}\right) \tag{16}$$

The ABLER of the system can be extracted by averaging the BLER given in (15), which leads to the equation, [20]:

$$ABLER=\int_{\vec{\gamma}}P(M,N;\vec{\gamma})f_{\vec{\gamma}}(\vec{\gamma})d\vec{\gamma} \tag{17}$$

where $\vec{\gamma}=(\gamma_1,\gamma_2,...,\gamma_K)$ is the vector signal consisting of the K separate signals reaching the receiver. The substitution of (15) and (16) into (17) results in the following expression for the ABLER:

$$ABLER=\int_{\vec{\gamma}}\sum_{m=M+1}^{N}\binom{N}{m}Q\left(\sqrt{\sum_{l=1}^{K}\gamma_l}\right)^m\left[1-Q\left(\sqrt{\sum_{l=1}^{K}\gamma_l}\right)^{N-m}\right]f_{\vec{\gamma}}(\vec{\gamma})d\vec{\gamma} \tag{18}$$

In order to simplify the integral of (18) two steps are followed. Firstly, the approximation of the Q function given by, [22]

$$Q(x)\approx\frac{1}{12}\left[\exp\left(-\frac{x^2}{2}\right)+3\exp\left(-\frac{2x^2}{3}\right)\right] \tag{19}$$

is used, an approximation that is simple and very accurate, and then the binomial expansion and multinomial formulae are applied. Also, taking into account that the separate SNRs γ_l are independent, the ABLER of the system takes the form:

ISSN:1791-4469

$$ABLER \approx \prod_{l=1}^{K}\left[\int_0^{\infty}\sum_{m=M+1}^{N}\binom{N}{m}\sum_{j=0}^{N-m}\binom{N-m}{j}\sum_{r=0}^{m+j}\binom{m+j}{r}\frac{(-1)^j}{12^{m+j-r}4^r}\times \right.$$
$$\left.\times\exp\left(-\frac{\gamma_l(3m+3j+r)}{12}\right)f_{\gamma_l}(\gamma_l)d\gamma_l\right] \quad (20)$$

By substituting the combined PDF of the system (11) into (20) and the ABLER can be written as:

$$ABLER \approx \prod_{l=1}^{K}\left[\sum_{m=M+1}^{N}\binom{N}{m}\sum_{j=0}^{N-m}\binom{N-m}{j}\sum_{r=0}^{m+j}\binom{m+j}{r}\frac{(-1)^j}{12^{m+j-r}4^r}\frac{g_l^4\Gamma\left(g_l^2\right)}{A_{0,l}\Gamma\left(1+g_l^2\right)\sqrt{\xi_l}}\times \right.$$
$$\left.\times\int_0^{\infty}\gamma_l^{-1/2}\exp\left(-\frac{3m+3j+r}{12}\gamma_l\right)G_{1,2}^{2,0}\left(\frac{g_l^2\Gamma\left(g_l^2\right)}{A_{0,l}\Gamma\left(1+g_l^2\right)\sqrt{\xi_l}}\sqrt{\gamma_l}\,\middle|\,\begin{matrix}g_l^2\\ g_l^2-1,\ 0\end{matrix}\right)d\gamma_l\right] \quad (21)$$

The final form of the ABLER can be obtained by solving the integral of (21) and is given by the following formula:

$$ABLER \approx \prod_{l=1}^{K}\left[\sum_{m=M+1}^{N}\binom{N}{m}\sum_{j=0}^{N-m}\binom{N-m}{j}\sum_{r=0}^{m+j}\binom{m+j}{r}\frac{(-1)^j}{12^{m+j-r}4^r}\times \right.$$
$$\times\frac{g_l^4\Gamma\left(g_l^2\right)}{4\sqrt{\pi\xi}A_{0,l}\Gamma\left(1+g_l^2\right)}\left(\frac{12}{3m+3j+r}\right)^{1/2}\times \quad (22)$$
$$\left.\times G_{3,4}^{4,1}\left(\left(\frac{g_l^2\Gamma\left(g_l^2\right)}{A_{0,l}\Gamma\left(1+g_l^2\right)}\right)^2\frac{3}{(3m+3j+r)\xi}\,\middle|\,\begin{matrix}\frac{1}{2},\ \frac{g_l^2}{2},\ \frac{g_l^2+1}{2}\\ \frac{g_l^2-1}{2},\ \frac{g_l^2}{2},\ 0,\ \frac{1}{2}\end{matrix}\right)\right]$$

IV. NUMERICAL RESULTS

In this section the average BLER of an FSO system with multiple receivers over saturated turbulence strength and pointing errors will be estimated using equation (22). We assume that the bit blocks consist of N=4 or 5 bits and a block will be considered erroneous in case more than 2 or 3 bits are faulty. The main parameters of the FSO link are presented in the following table:

Parameter	Value
ratio equivalent beam and displacement standard deviation (g)	2.52
Fraction of collected beam power (A_0)	0.039

TABLE 1: Parameters of the FSO link

The results will be extracted in case of a SISO system, K=1 and for the case of SIMO scheme, two receivers will be used, K=2. For simplicity, it can be assumed that the instantaneous SNR at the receivers are the same equal, i.e $\gamma_1 = \gamma_2 = ... = \gamma_K$.

In Figure 1, the average BLER results are presented for a SISO system. It is clear that as the number of acceptable erroneous bits in a certain number of bit blocks increases, the system has better performance as the block error probability decreases. This improvement can be more than one order of magnitude.

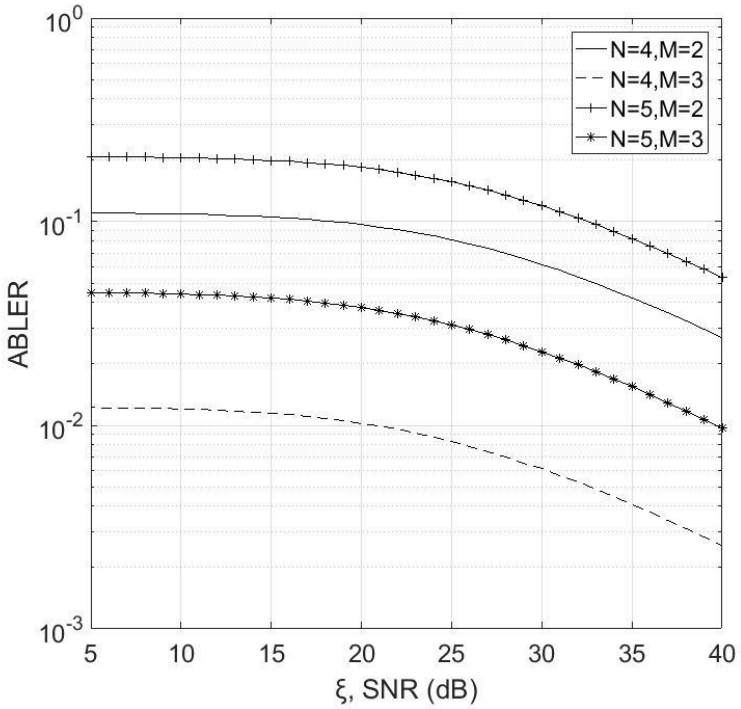

FIGURE 1: ABLER versus the expected SNR, ξ, for saturated turbulence and pointing errors for a SISO FSO system.

In Figure 2, the corresponding results for a SIMO system with two receivers are presented. Similarly to Figure 1, the BLER improves as the number of accepted erroneous bits in one block increases.

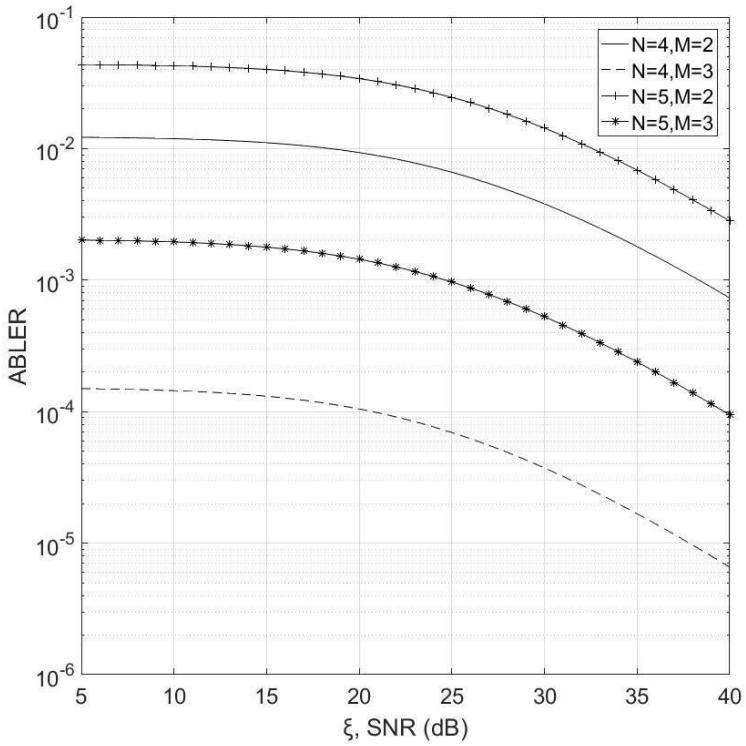

FIGURE 2: ABLER versus the expected SNR for saturated turbulence and pointing errors for a SIMO FSO system.

Comparing Figures 1 and 2 we can notice the remarkable improvement of system's performance as the number of receivers increases. This technique can achieve more than 2 orders of magnitudes lower BLER. More specifically, the percentage of the reduction in the BLER achieved by the SIMO system is presented in Figure 3, as a function of the expected SNR. So, even under strong turbulence conditions with pointing errors, the FSO link can perform reliably and securely satisfying even the most demanding links in modern networks.

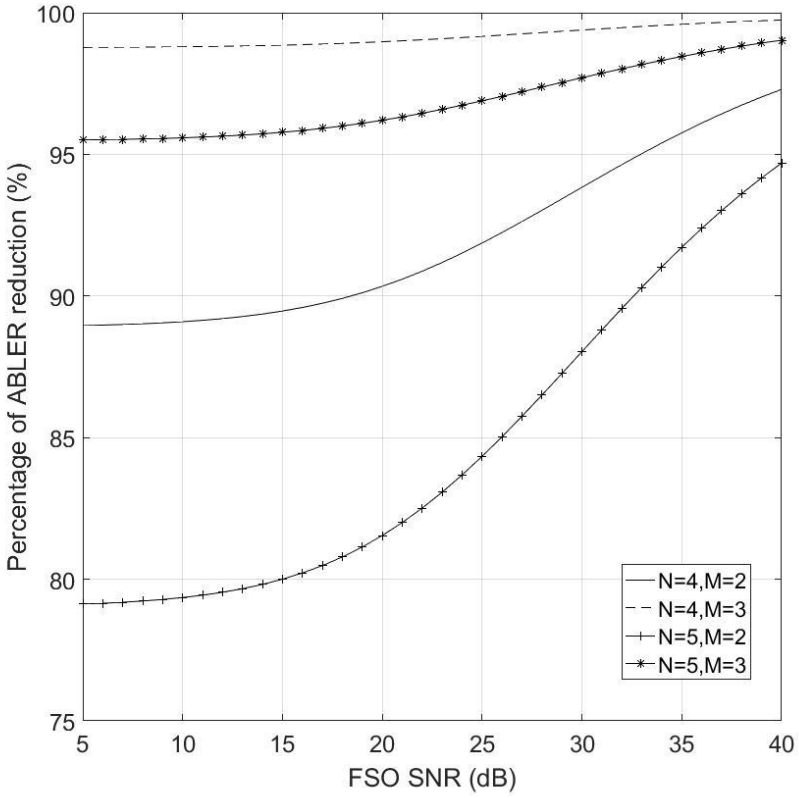

FIGURE 3: Percentage of the ABLER reduction achieved by the SIMO system compared to the SISO one, as a function of the expected SNR.

V. CONCLUSION

In this work, the performance of a SIMO FSO link under strong turbulence with pointing errors was investigated. a new mathematical expression for the average block error rate was derived, a metric that is very useful in order to implement a modern network. according to the results that were extracted, SIMO technique can further increase the performance and the reliability of an FSO system, providing high quality of service even under severe atmospheric conditions.

ACKNOWLEDGMENTS

This research is co-financed by Greece and the European Union (European Social Fund- ESF) through the Operational Programme «Human Resources Development, Education and Lifelong Learning» in the context of the project “Strengthening Human Resources Research Potential via Doctorate Research” (MIS-5000432), implemented by the State Scholarships Foundation (IKY).

REFERENCES

1. X. Z. X. Zhu and J. M. Kahn, "Free-space optical communication through atmospheric turbulence channels," *IEEE Trans. Commun.*, vol. 50, no. 8, pp. 1293–1300, 2002.
2. M. A. Al-Habash, L. C. Andrews, and R. L. Phillips, "Mathematical model for the irradiance probability density function of a laser beam propagating through turbulent media," *Opt. Eng.*, vol. 40, no. 8, p. 1554, Aug. 2001.
3. L. C. Andrews and R. L. Phillips, *Laser Beam Propagation through Random Media*. 1000 20th Street, Bellingham, WA 98227-0010 USA: SPIE, 2005.
4. G. Aarthi and G. Ramachandra Reddy, "Average spectral efficiency analysis of FSO links over turbulence channel with adaptive transmissions and aperture averaging," *Opt. Commun.*, vol. 410, no. December 2017, pp. 896–902, 2018.
5. R. Kaushik, V. Khandelwal, and R. C. Jain, "A New Closed Form Approximation for BER for Optical Wireless Systems in Weak Atmospheric Turbulence," *J. Opt. Commun.*, vol. 39, no. 2, pp. 247–253, Apr. 2018.
6. H. E. Nistazakis, T. A. Tsiftsis, and G. S. Tombras, "Performance analysis of free-space optical communication systems over atmospheric turbulence channels," *IET Commun.*, vol. 3, no. 8, p. 1402, 2009.
7. G. K. Varotsos, H. E. Nistazakis, M. I. Petkovic, G. T. Djordjevic, and G. S. Tombras, "SIMO optical wireless links with nonzero boresight pointing errors over M modeled turbulence channels," *Opt. Commun.*, vol. 403, no. February, pp. 391–400, 2017.
8. H. G. Sandalidis, T. A. Tsiftsis, G. K. Karagiannidis, and M. Uysal, "BER Performance of FSO Links over Strong Atmospheric Turbulence Channels with Pointing Errors," *IEEE Commun. Lett.*, vol. 12, no. 1, pp. 44–46, Jan. 2008.
9. R. Boluda-Ruiz, A. García-Zambrana, C. Castillo-Vázquez, and B. Castillo-Vázquez, "Novel approximation of misalignment fading modeled by Beckmann distribution on free-space optical links," *Opt. Express*, vol. 24, no. 20, p. 22635, 2016.
10. W. Gappmair and H. E. Nistazakis, "Subcarrier PSK Performance in Terrestrial FSO Links Impaired by Gamma-Gamma Fading, Pointing Errors, and Phase Noise," *J. Light. Technol.*, vol. 35, no. 9, pp. 1624–1632, 2017.
11. S. M. Navidpour, M. Uysal, and M. Kavehrad, "BER performance of free-space optical transmission with spatial diversity," *IEEE Trans. Wirel. Commun.*, vol. 6, no. 8, pp. 2813–2819, 2007.
12. N. D. Chatzidiamantis, G. K. Karagiannidis, E. E. Kriezis, and M. Matthaiou, "Diversity combining in hybrid RF/FSO systems with PSK modulation," *IEEE Int. Conf. Commun.*, 2011.
13. G. K. Varotsos, H. E. Nistazakis, C. K. Volos, and G. S. Tombras, "FSO links with diversity pointing errors and temporal broadening of the pulses over weak to strong atmospheric turbulence channels," *Optik (Stuttg).*, vol. 127, no. 6, pp. 3402–3409, 2016.
14. L. Han, H. Jiang, Y. You, and Z. Ghassemlooy, "On the performance of a mixed RF/MIMO FSO variable gain dual-hop transmission system," *Opt. Commun.*, vol. 420, no. March, pp. 59–64, 2018.
15. M. P. Ninos, H. E. Nistazakis, and G. S. Tombras, "On the BER performance of FSO links with multiple receivers and spatial jitter over gamma-gamma or exponential turbulence channels," *Optik (Stuttg).*, vol. 138, pp. 269–279, 2017.
16. H. E. Nistazakis, "A time-diversity scheme for wireless optical links over exponentially modeled turbulence channels," *Optik (Stuttg).*, vol. 124, no. 13, pp. 1386–1391, 2013.
17. A. K. Majumdar, *Advanced Free Space Optics (Fso) - a System Approach*, vol. 140. 2015.
18. A. A. Farid and S. Hranilovic, "Outage capacity optimization for free-space optical links with pointing errors," *J. Light. Technol.*, vol. 25, no. 7, pp. 1702–1710, 2007.
19. I. S. Gradshteĭn and I. M. Ryzhik, *Table of Integrals, Series, and Products*. Elsevier, 2014.

20. K. O. Odeyemi, P. A. Owolawi and V. M. Srivastava, “Performance analysis of Block Error Rate for SIM-FSO system with spatial diversity over Gamma-Gamma fading and pointing error channel,” *2017 IEEE AFRICON Sci. Technol. Innov. Africa, AFRICON 2017*, pp. 115–120, 2017.
21. Q. Zhang, J. Cheng and G. K. Karagiannidis, “Block error rate of optical wireless communication systems over atmospheric turbulence channels,” *IET Commun.*, vol. 8, no. 5, pp. 616–625, Mar. 2014.
22. M. Chiani, D. Dardari and M. K. Simon, “New exponential bounds and approximations for the computation of error probability in fading channels,” *IEEE Trans. Wirel. Commun.*, vol. 24, no. 5, pp. 840–845, May 2003.

ISSN:1791-4469

Substrate Thickness Impact in Ka-Band-Pass Filter Design Methodology

Th. Mpountas[a], E. Pantazopoulos[b], E. Karagianni[b], J. Papananos[a] and D. Kaklamani[a]

[a]*National Technical University of Athens, School of Electrical & Computer Engineering*
[b]*Hellenic Naval Academy*

Abstract. A high performance band pass filter (BPF), with the assistance of the Richards-Kuroda Transformation method, on the basis of the known Chebyshev-Lowpass Filter, is presented. This suggested filter consists of six edge-coupled striplines. The filter operates at Ka-band from 37 GHz to 40 GHz. The proposed circuit is simulated using Laminate R-5785(N) with dielectric constant of 3.34, substrate height of 500um and 750 um and thickness of 17 um. According to the simulation results, the filter is suitable for being integrated within various microwave subsystems.

Keywords: Band Pass Filter, Chebyshev, Edge-coupled, Stripline.

INTRODUCTION

Stripline filters play an important role in many RF applications. As technologies advances, more stringent requirements of filters are required. One of the requirements is the compactness of filters [10]-[11]. For microwave frequencies (>3GHz), passive filter is usually realized using distributed circuit elements such as transmission line sections.

Many research articles have used waveguides for transmission line filter. However, waveguides systems are bulky and expensive. Low-power and cheaper alternatives are stripline and microstrip. These transmission lines are compact [12]. Edge-coupled stripline is used instead of microstrip line as stripline does not suffer from dispersion and its propagation mode is pure TEM mode. Hence it is the preferred structured for coupled-line filters.

Therefore, a fifth order Chebyshev edge-coupled stripline filter is designed and presented in the article. The band pass filter is simulated by using Advanced Design System software.

FILTER TYPES

Several mathematical models and circuits have been developed for the mathematical analysis of the filters, in order to achieve the best possible simulation of an ideal filter behavior. These mathematical models are categorized into the following basic types: Butterworth filters, Chebyshev filters and Bessel filters [1] [3].

The Butterworth filter is a medium-Q filter that is used in designs that require the amplitude response of the filter to be as flat as possible. The Butterworth response is the flattest passband response available and contains no ripple. Since the Butterworth response is only a medium-Q filter, its initial attenuation steepness is not as good as some filters but it is better than others. This characteristic often causes the Butterworth response to be called a middle-of-the-road design.

ISSN:1791-4469

The Chebyshev filter is a high-Q filter that is used when: (1) a steeper initial descent into the stopband is required, and (2) the passband response is no longer required to be flat. With this type of requirement, ripple can be allowed in the passband. As more ripple is introduced, the initial slope at the beginning of the stopband is increased and produces a more rectangular attenuation curve when compared to the rounded Butterworth response.

The initial stopband attenuation of the Bessel filter is very poor and can be approximated by:

$$A_{dB} = 3\left(\frac{\omega}{\omega_c}\right)^2 \quad (1)$$

This expression, however, is not very accurate above an ω/ωc that is equal to about 2. For values of ω/ωc greater than 2, a straight-line approximation of 6 dB per octave per element can be made. However, the Bessel filter was originally optimized to obtain a maximally flat group delay or linear phase characteristic in the filter's passband. Thus, selectivity or stopband attenuation is not a primary concern when dealing with the Bessel filter.

METHODOLOGY

The requirements for the design of the band pass filter are presented in Table 1. The specification of dielectric material is obtained from Laminate R-5785(N) (Table 2).

Since Chebyshev filter haw steeper initial descent into the stopband than other filter types, this type of filter is chosen in this research work. The filter has been designed by following the five steps: (I) Determining the order and the type of approximation functions to be used (ii) Finding the corresponding low-pass prototype (iii) transforming the low-pass network into bandpass filter (iv) Scaling the bandpass filter in both impedance and frequency and (v) Transforming the lumped elements into distributed realization.

TABLE 1. Requirements of band pass filter

Frequency	**Loss**
31.3 GHz – 31.8 GHz	>54 dB
31.8 GHz – 35.5 GHz	>30 dB
37 GHz – 40 GHz	<3 dB (passband)
>41.5 GHz	>30 dB

TABLE 2. Specifications of substrate and dielectric material

Dielectric material used	Laminate R-5785(N)
Dielectric constant	3.34
Loss tanget, tanδ	0.003
Substate height	500um / 750um
Copper thickness	17um

TABLE 3. Prototype G values

Order	G[0]	G[1]	G[2]	G[3]	G[4]	G[5]
5th	0.8472	1.3449	1.67	1.34	0.85	1

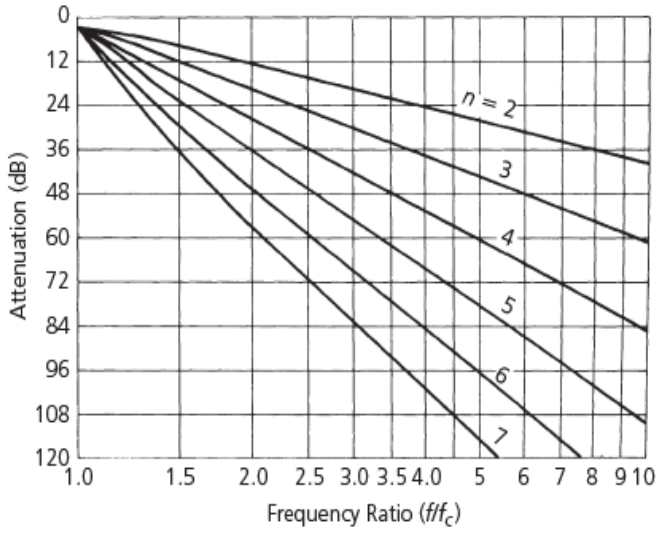

FIGURE 1. Attenuation characteristics for a Chebyshev filter with 0.01-dB ripple

The order of the band pass Chebyshev filter can be determined by using the attenuation characteristics for 0.01dB ripple shown in Fig. 1. In order to find the order of the band pass filter, we have to compute the following expression:

$$\frac{BW}{BW_c} = \frac{f}{f_c} \tag{2}$$

Where, BW is the bandwidth at the required value of attenuation and the BWc is the 3-dB bandwidth of bandpass filter. For the filter of this research work, it is revealed that a 5-element filter will provide more than 54dB of attenuation, which is more than adequate.

The element values for the fifth-order are taken from the Table 3 of normalized values of 0.01dB equal ripple lowpass prototype. The lowpass prototype is presented in Fig.2.

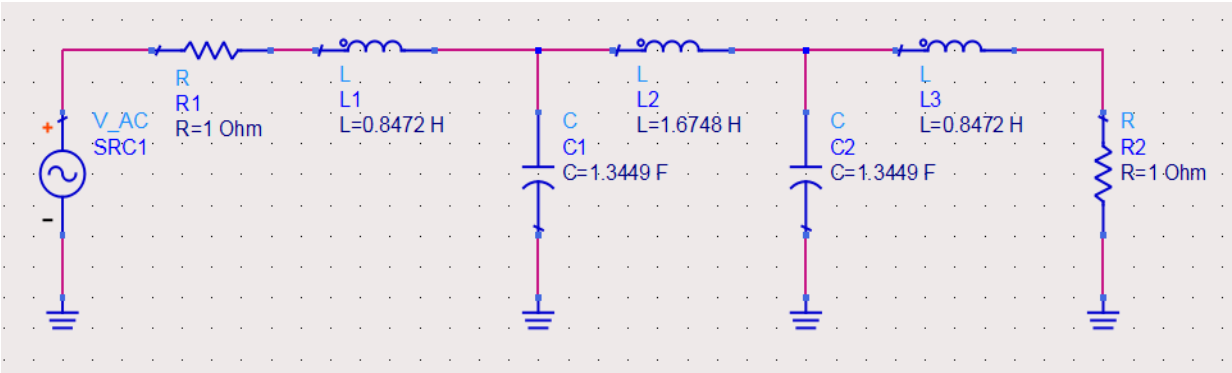

FIGURE 2. Low pass prototype filter 5th order

The actual conversion from the low pass prototype to the bandpass filter is achieved by adding to each branch of the low pass filter an element of the opposite type at the same value. The

conversion of the low pass prototype filter into a band pass Chebyshev type filter is shown in Fig. 3.

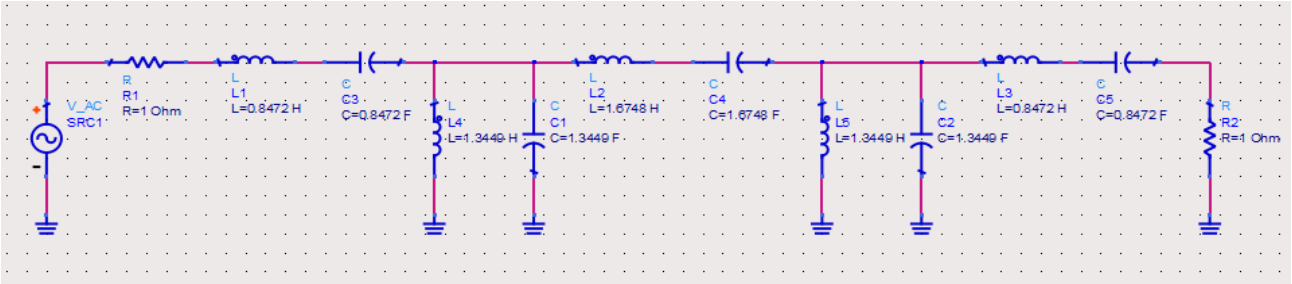

FIGURE 3. Band pass Chebyshev type filter 5th order after conversion

Subsequently, we are scaling the bandpass filter in both impedance and frequency, by using the following mathematical formulas. For parallel-resonant branches,

$$C = \frac{C_n}{2\pi RB} \tag{3}$$

$$L = \frac{RB}{2\pi L_n f_0^2} \tag{4}$$

and for series-resonant branches,

$$C = \frac{B}{2\pi f_0^2 C_n R} \tag{5}$$

$$L = \frac{RL_n}{2\pi B} \tag{6}$$

where,

C=the final capacitor value,
L=the final inductor value,
B=the 3-dB bandwidth,
R=the final load resistance,
fo=the geometric center frequency,
Cn=the normalized capacitor band-reject element value,
Ln=the normalized inductor band-reject element value.

The results are presented in Fig.4.

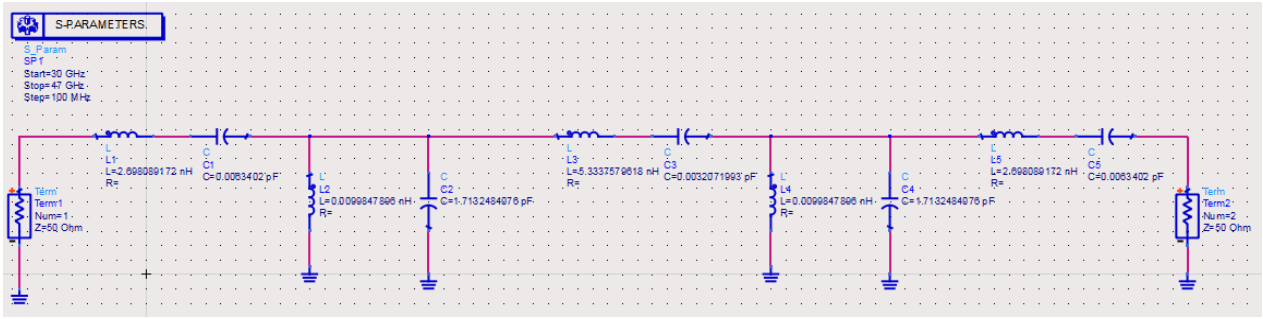

FIGURE 4. Band pass prototype Chebyshev type filter 5th order after scaling the bandpass filter in both impedance and frequency

Richard's tranformation and Kuroda's identities are used to accomplish from the lumped to distributed circuit designs. The explanation of Richard's transformation and Kurada's identities are in [2]. Each section of coupled stripline contains three parameters: S (seperation of two striplines), W (width of stripline) and h (height of substrate). These three parameters are determined from the odd and even mode impendance (Zoo and Zoe) of each coupled-line. Zoo and Zoe are in turn depends on the gain of the corresponding admittance inverter J.

$$J_1 = \frac{1}{Z_0}\sqrt{\frac{\pi\Delta}{2g_1}} \tag{7}$$

$$J_n = \frac{1}{2Z_0}\frac{\pi\Delta}{\sqrt{g_{n-1}\,g_n}} \tag{8}$$

$$J_{n+1} = \frac{1}{Z_0}\sqrt{\frac{\pi\Delta}{(2g_N\,g_{N+1})}} \tag{9}$$

$$\Delta = \frac{f_2 - f_1}{f_0} \tag{10}$$

$$Z_{oe} = Z_o(1 + JZ_0 + (JZ_0)^2) \tag{11}$$

$$Z_{oo} = Z_o(1 - JZ_0 + (JZ_0)^2) \tag{12}$$

The values of the parameters W, S and L (Length of stripline) are presented in the Table 4 for two different substrate heights 500um and 750 um.

TABLE 4. Dimensions for striplines for substrate height 500um and 750um

Dimensions	Substrate height 500um	Substrate height 750um
W[1]	186 um	291 um
W[2]	254 um	396 um
W[3]	259 um	403 um
S[1]	48 um	68 um
S[2]	183 um	267 um
S[3]	233 um	343 um
L	1069 um	1069 um

ISSN:1791-4469

SIMULATION RESULTS

The band pass filter is simulated with ADS software tool in order to predict the performance of the filter. According to the simulation results, the insertion loss is less than 3 dB in passband. Also the response is almost flat over the entire passband. In addition, the simulated response has the attenuation of more than 30 dB at central frequency. The simulation results for both substrate thicknesses (500um and 750u) are presented in Fig.5 and Fig.6. We observe that for higher substrate thickness the results meet the requirements. Finally, the layout of bandpass filter is at Fig.6.

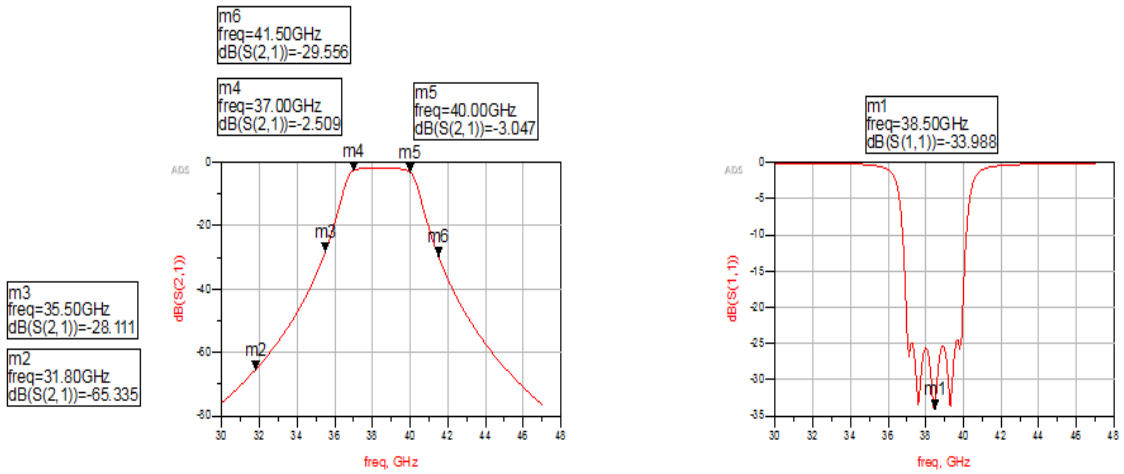

FIGURE 5. Simulation results from ADS for substrate height 500um

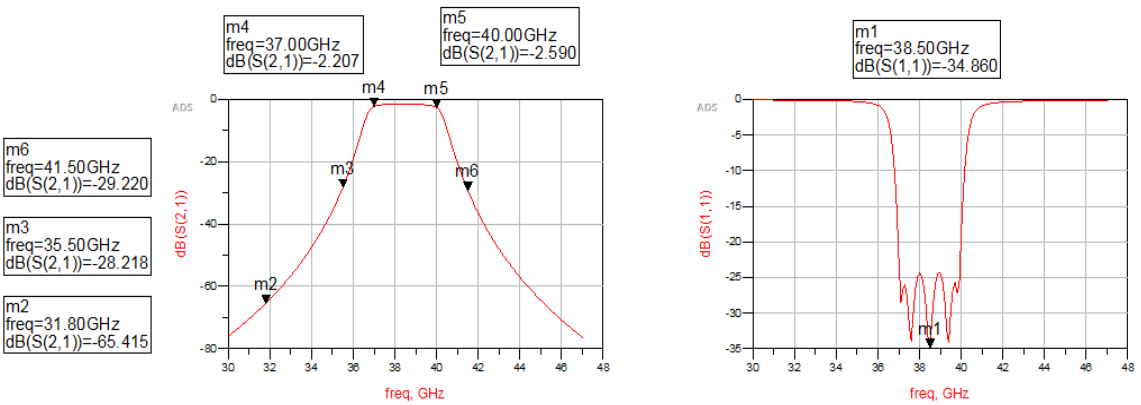

FIGURE 5. Simulation results from ADS for substrate height 750um

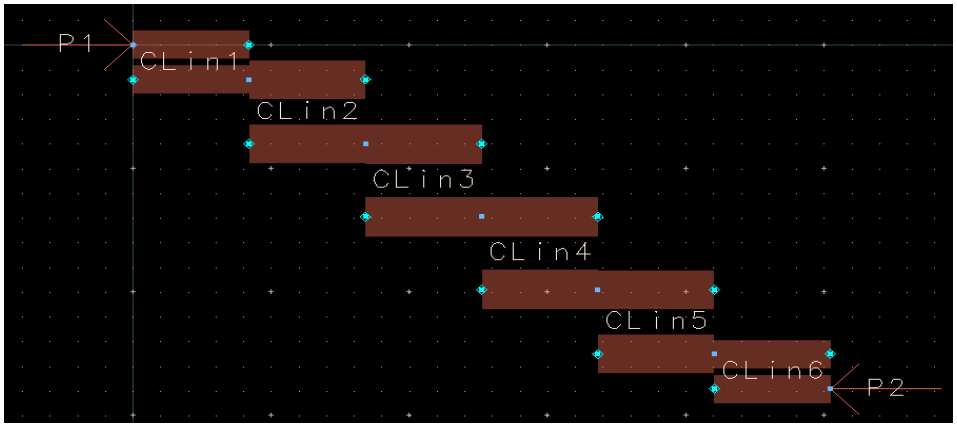

FIGURE 6. Layout

CONCLUSION

This paper describes a procedure for designing a band pass filter with central frequency at 38.5GHz, with 3dB maximum ripple in passband. It was presented step-by-step the construction of the band pass Chebyshev type filter. The requirements for the design of the filter were met in both passband and stopband. Finally, in this article it is proved that the higher the substrate thickness, the better the response of the filter.

REFERENCES

1. "Filter Design", in RF Circuit Design, edited by Chris Bowick
2. "Filters with Distributed Elements ", in Analog Filters Using Matlab, edited by Lars Wanhammar
3. "RF/MMIC", edited by E. Karagianni
4. D.E. Tsigkas, D.S. Alysandratou and E.A. Karagianni, "Butterworth Filter Design at RF and X-band Using Lumped and Step Impedance Techniques", International Journal of Advanced Research in Electronics and Communication Engineering, Volume 3, Issue 4, April 2014.
5. Zisis S., Karagianni E., Nistazakis H.E., Vazouras Ch., Tsigopoulos A.D., Fafalios M., "Maximally Flat Microstrip Band-Pass Filter Design for UWB Applications Using Step Impedance Techniques and Quarter-Wave Structures", , International Conference from Scientific Computing to Computational Engineering, 7th IC-SCCE, 2016
6. Kasapoglu, G.B.; Karagianni, E.A.; Fafalios, M.E.; Koukos, I.A., "Coefficients Calculation in Pascal Approximation for Passive Filter Design". Computation 2018, 6, 18
7. Viswanadha K., Raghava N.S., "Design of a Narrow-Band Pass Asymmetric Microstrip Coupled-Line Filter with Distributed Amplifiers at 5.5 GHz for WLAN Applications", Applications of Artificial Intelligence Techniques in Engineering, Advances in Intelligent Systems and Computing, vol 697, Springer (2019)
8. Evangelia A Karagianni, Yorgos E Stratakos, Christos N Vazouras, Michael E Fafalios, "Design and Fabrication of a Microstrip Hairpin-Line Filter by Appropriate Adaptation of Stripline Design Techniques", Symposium on Microwave and Optical Technology
9. "Comparative performance of some polynomial-based lowpass filters for microwave/digital transmission applications", International Journal of Electronics, Volume 106, 2019

ISSN:1791-4469

10. Y. M. Yan, Y. T. Chang, H. Wang, R. B. Wu, a nd C. H. Chen, "Highly selective microstrip bandpass filters in Ka- band, " in 32th Eur. Microwave Conf. Proc., 2002, pp. 1137-1140.
11. W.Lars, Design and Optimization of Low Pass Filter Using Microstrip Lines, Analog Filters Using MATLAB, 2009.
13. A Kumar, AK Verma, "Comparative performance of some polynomial-based lowpass filters for microwave/digital transmission applications", International Journal of Electronics, 2019
14. K Viswanadha, NS Raghava, "Design of a Narrow-Band Pass Asymmetric Microstrip Coupled-Line Filter with Distributed Amplifiers at 5.5 GHz for WLAN Applications", - Applications of Artificial Intelligence Techniques in Engineering, 2018

Microstrip RFID Antenna Design at 5.1 GHz

T.J. Korfiati[a], E.A. Karagianni[b], A.T. Arapoyianni[a], C.N. Vazouras[b], A.D. Tsigopoulos[b]

[a] *National and Kapodistrian University of Athens*
[b]*Hellenic Naval Academy*

Abstract. A design of a microstrip tag antenna with a configurable design is introduce for the C frequency band. The coupling between the microstrip lines is achieved by reducing the distance between the lines. The tag antenna has a good impedance input matching with -20.016dB return loss at 5.1 GHz.

Keywords: Antennas; Coupled lines; Microstrip lines; RFID; Spiral Antenna; Tag

1. INTRODUCTION

Radio Frequency Identification (RFID) is currently one of the most promising and discussed auto-identification and data capture technologies. Although it is not a new technology it has become a mainstream and remains in the front end of the general research and development sector concerning the remotely receiving and transmitting data using RF waves. In the ultra-high frequencies (UHF) band there are many applications in which an RFID antenna can be used, such as object identification, accessing control, satellite communication, millimeter wave wireless technologies. A RFID system consists of three parts namely reader, tag and the data processing system [1], [2]. One of the notable challenges in RFID technologies is the small-sized tag antennas design with high impedance matching for IC chips. So, in this paper we focus on the tag antenna RFID and a design of a microstrip RFID antenna is presented. A microstrip line has become the best known and most widely used planar transmission line for RF and Microwave circuits. In simple terms, microstrip is a printed circuit version of a wire over a ground plane, and thus it tends to radiate as the spacing between the ground plane and the strip increases [3]. Coupled microstrip lines are formed by two transmission lines which are positioned parallel to each other, as it is presented in Figure 1. In such a unit there is a continuous coupling between the lines because of the presence of electromagnetic field. The coupled lines are used widely as key elements of direction couplers, filters and a variety of electronic circuits. Because of the coupling of electromagnetic fields, a pair of coupled lines can support two different modes [4], [5].

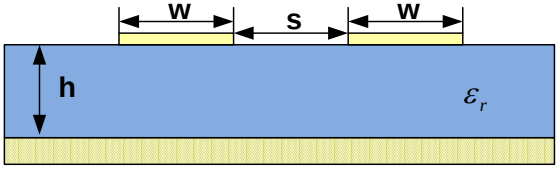

FIGURE 1. Coupled Microstrip Lines

ISSN:1791-4469

2. ANTENNA DESIGN

A pair of equal width microstrip lines is presented in Figure 2 labeled as 1 and 2 for each strip line, with constant spacing between them. The characteristic impedance Z0 is defined by the self-inductance L11, and self-capacitance C11 with respect to the ground, in the case that the voltages in the conductors are equal. If spacing between the transmission lines is decreased, there will be electromagnetic coupling, which is defined by the mutual inductance L12 and mutual capacitance C12. Also, in Figure 2 the physical interpretation of equivalent capacitances of odd mode is represented. The odd mode corresponds to an antisymmetric stimulation (the even mode has symmetric stimulation) which means that the voltages of the two microstrips lines are equal and opposite. Also we have capacitances that are the result of edge phenomenon and capacitances of adjacency. It is important to note that the capacitances of adjacency are appearing because of the odd mode [5], [6].

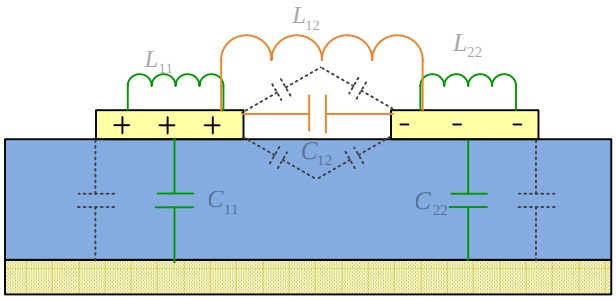

FIGURE 2. Coupled Microstrip Lines with capacitances.

The characteristic impedances Zce for even and Zco for odd mode can be obtain from the following equations (1), (2) [6].

$$Z_{ce} = \left(c \cdot \sqrt{C_e^a \cdot C_e}\right)^{-1} \quad (1)$$

$$Z_{co} = \left(c \cdot \sqrt{C_o^a \cdot C_o}\right)^{-1} \quad (2)$$

$$C_e = C_p + C_f + C_{f'} \quad (3)$$

$$C_o = C_p + C_f + C_{gd} + C_{ga} \quad (4)$$

$$C^a = \varepsilon / h \quad (5)$$

Where Co, Ce are the even and odd mode capacitance, Cα is capacitance for air dielectric (ε is dielectric constant of the material and h thickness of the material), Cp is the parallel capacitance between strip and ground plane, Cf is the fringe capacitance, Cf ‘ is the modification of fringe capacitance Cf of a single line due the presence of another line, Cgd and Cga are the adjacency capacitance [6].

Selecting rectangular spiral shape to implement the tag antenna was the fact that, as the dimensions are minimized, result is saving space. Hence, the spiral shape ensures antenna small dimensions while the total line length is adequate to achieve antenna resonance at the desire frequency.

The design consists of a coil with a given number of turns and a given size. The tag has two layers. The first one consists of GaAs dielectric and the second of copper with a given thickness,

also. Although the length, the width, the thickness and the space between the copper strips and the thickness of the dielectric layer have been created with specific dimensions initially, they all could be changed so that our design can be parameterized for any value under specific limitations. Figure 4 represents the initial RFID design with the configurable size parameters. The total size is initially equal to x0*y0=35x35 mm^2. The microstrip line is of x = 1.5 mm width. The thickness of copper is bcop = 0.04 mm and the space between lines is s = 0.5mm. Also, bsp = 0.18 mm, bsub = 0.32mm is the substrate thickness, those variables representing in a layout view in Figure (3a). The space between strip line 5 and strip line 1 as represent in Figure (3b) is k = 7mm.

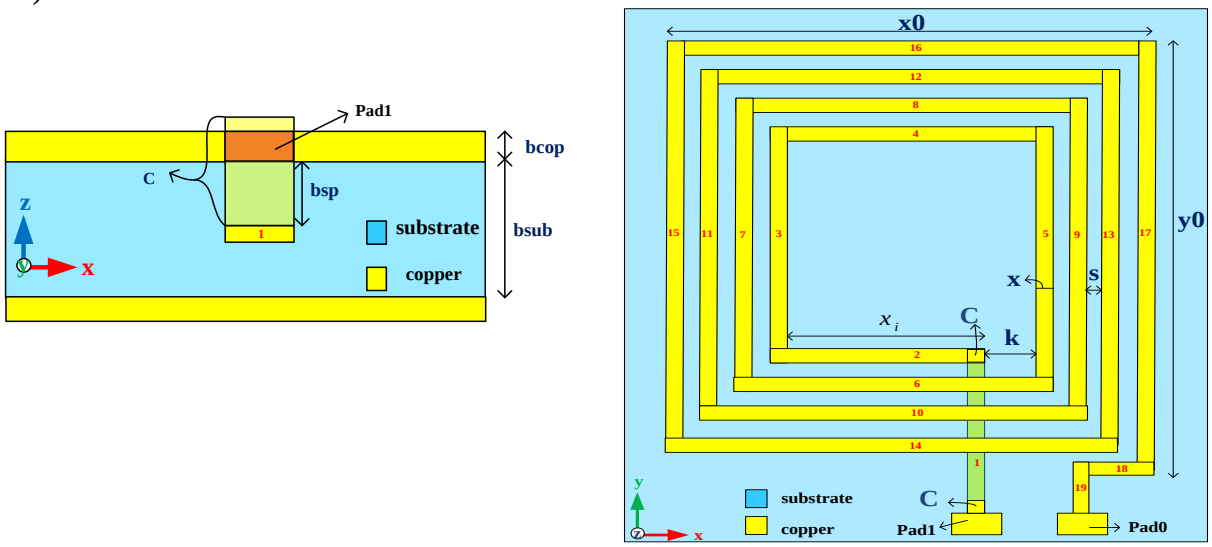

(a) (b)

FIGURE 3. (a) Variable representation at the z,x view, (b) RFID design

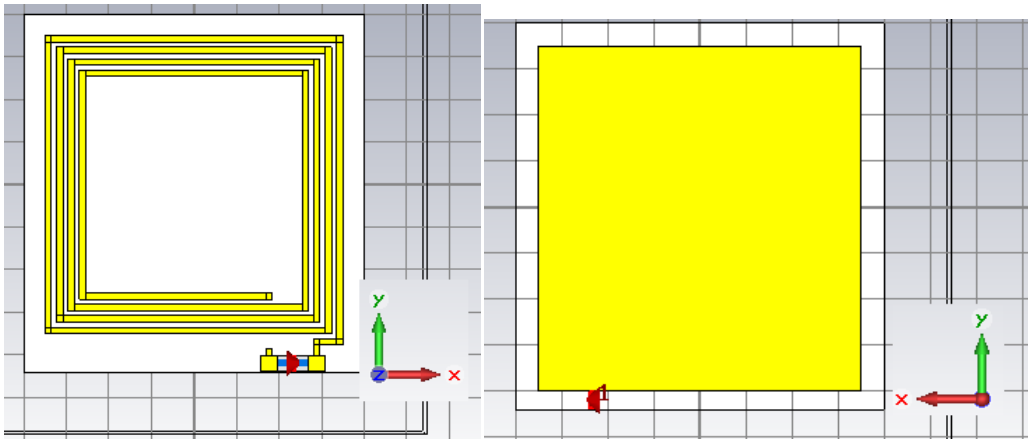

(a) (b)

FIGURE 4. RFID design in CST Studio (a) front area of RFID, (b) back area of RFID

The reactance of the coil for resonance frequency F is given by the following equation (6).

$$X_L = 2\,\pi\,F\,L \tag{6}$$

Considering that the circular shaped inductor and the square shaped inductor have equivalent model equations regarding x, s, x0, y0 (6), (7), (8), we can use the equation (7) to calculate the inductance L for the square spiral inductor with n number of turns,

$$L(nH) = 0.03937 \cdot \frac{a^2 \cdot n^2}{8 \cdot a + 11 \cdot c} \cdot Kg \tag{7}$$

Kg is a correction factor depended on the ratio w/h. In our case where x/bsub > 0.05 the Kg is given by (10), and α and c given by (8) and (9) respectively.

$$a = \frac{x_0 + x_i}{4} = \frac{x_0 + y_0 - 4 \cdot x - 3 \cdot s - k}{4} \tag{8}$$

$$c = \frac{x_0 - x_i}{2} = \frac{x_0 - (y_0 - 4 \cdot x - 3 \cdot s - k)}{2} \tag{9}$$

$$K_g = 0.057 - 0.145 \cdot \ln\left(\frac{x}{bsub}\right) \tag{10}$$

With the above equations (6), (7) if we change the parameters bcop, s and x the behavior of this antenna will be changed regarding matching, coupling and resonance frequency.

3. SIMULATION RESULTS

In this section the results of simulations of the tag design, by using the CST Studio are presented. Figure 5 represents the results of the input reflection coefficient S11 with the parameter Bsub ranging from Bsub = 0.32mm to Bsub = 64mm, while all the other parameters remain constant. Notice that the substrate material is GaAs at this antenna design. At this point, according to the results, it is should be noted, that the changes in substrate thickness affect the S11 value over frequency. So, with that result we can optimize the antenna to the desired `frequency. A passive RFID tag antenna with the minimum space between the microstrip lines s = 1.2mm, the maximum line's width x = 1.5mm, the maximum occupied area x0*y0 = 35mm^2. The S11 has a very good value of -20.016 dB at 5.103GHz. The value of s parameter was chosen to be that it is, as result the best gain and S11.

TABLE 1. Parameters of the design and results of the antenna

Parameters	**(mm)**
Bcop	0.04
Bsp	018
Bsub	0.72
K	7
S	1.2
X	1.5
X0	35
Y0	35
S11 (dB)	-20.016
Gain (dBi)	1.286
Directivity (dB)	5.217

S11 values in conjunction with gain and directivity values at 5.1GHz are represented in Table 1. Respectively we have a 1.286 dB gain, 5.217 dBi directivity, with these two values we can get the efficiency of the antenna n = 0.24 or 24% (n=Gain/Directivity).

Table 2 shows the comparison between the various parameters of antenna i.e. dimensions, substrate material, gain. It can be easily seen that the proposed antenna is a good candidate as with GaAs substrate can support IC. Also can take place in WLAN applications.

TABLE 2. Comparison of proposed antenna to previously reported antenna

Ref.	**Dimensions (mm)**	**Frequency (GHz)**	**Substrate**	**Gain(dBi)**
[12]	40.4 x 37.8	5.1	FR-4	0.65-1.91
[13]	10 x 13	5.1 - 5.5	FR-4	0-2.09
[14]	32 x 36	5.65 – 6.7	FR-4	1.72
Proposed Antenna	35 x 35	5.1	GaAs	1.286

ISSN:1791-4469

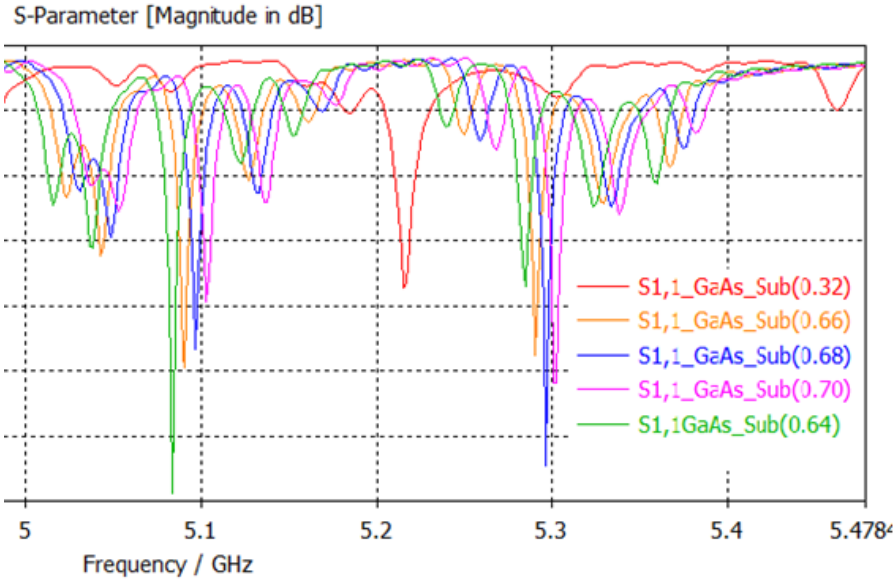

FIGURE 5. Simulation Results S11, with Bsub varied from Bsub = 0.32mm to Bsub = 64mm

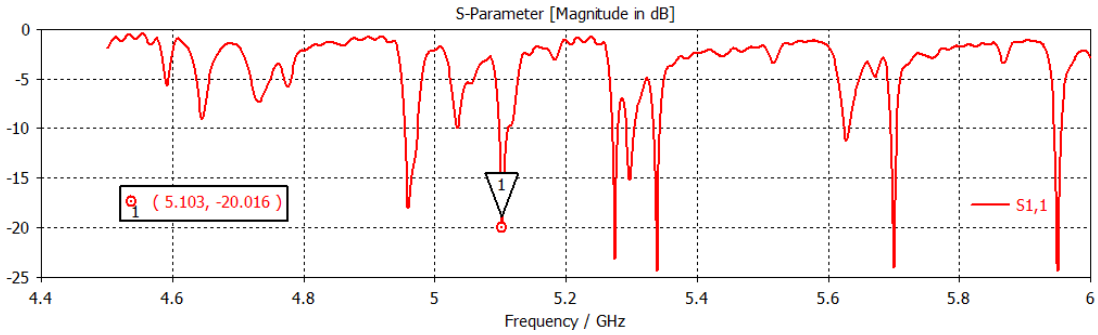

FIGURE 6. Simulation Results S11, at 5.1GHz

5. CONCLUSIONS

A RFID microstrip antenna that operates at the C frequency band has been introduced. In order to investigate and achieve optimum dimensions over the desire frequency range, the design has been parameterized having the flexibility in changing its dimensions. CST software has been used for analytical modelling and simulation. A balanced passive C-band RFID tag antenna with the minimum distance between the microstrip lines s = 1.2mm, the maximum line's width x = 1.5mm, the maximum occupied area x0*y0 = 35mm^2, is presented in Figure 7. It resonates at frequency 5.103GHz having a very good value of S11 as presented in Figure 8. The proposed RFID tag antenna has an impedance of 48.378-j15.42. Ω at 5.1GHz. A S11 of -20.016 dB is achieved at this frequency. 3D antenna radiation pattern is represent in Figure 9. The antenna gain is 1.286 dB, the directivity is 5.217 dBi and the efficiency of the antenna is n = 0.24 or 24%. In the chosen frequency band 5.1 GHz, witch is include in range 5.15 to 5.35 GHz, can be used for IEEE 802.11A Wi-Fi wireless computer networks [15]. Future work could focus to the optimization of the efficiency of antenna, so that a very good performance is achieved at the desired frequency.

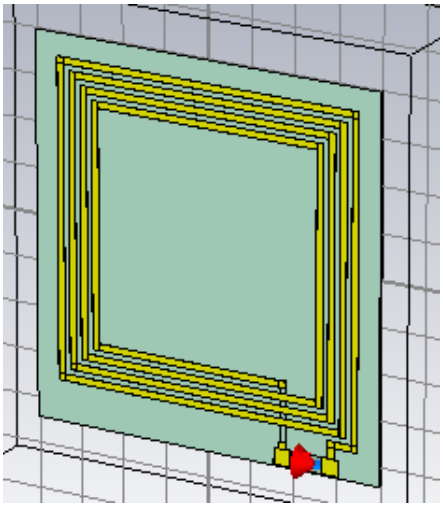

FIGURE 7. RFID Antenna

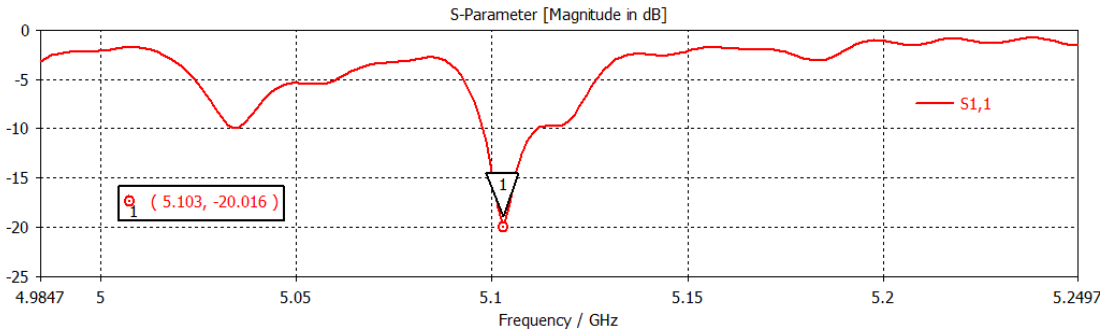

FIGURE 8. Simulation Results S11, at 5.1GHz

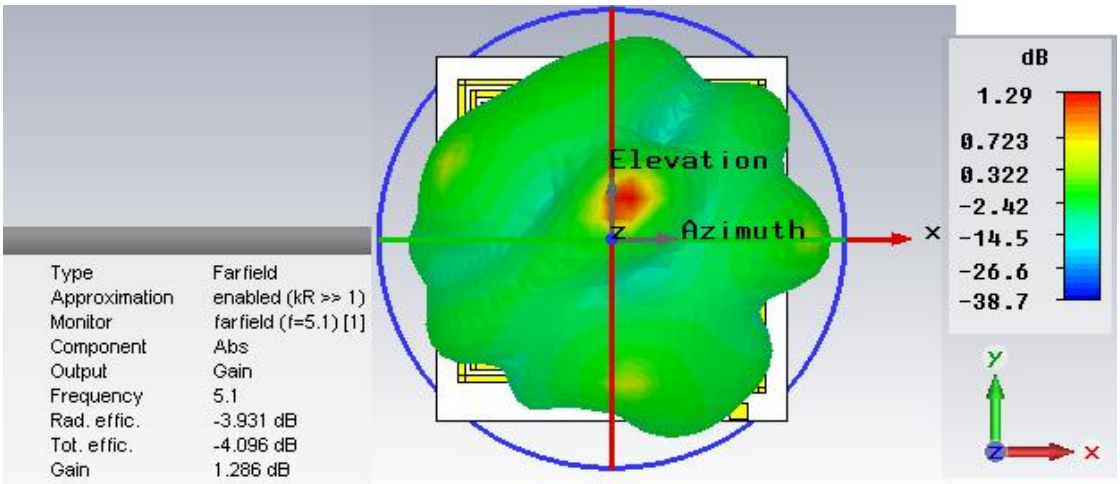

FIGURE 9. 3D Radiation Pattern at 5.1GHz in CST Studio

ISSN:1791-4469

REFERENCES

1. Huy Hung Tran, Ikmo Park "Compact Crossed Dipole Antenna for a Broadband UHF-RFID Tag", IEEE Antenna Technology (iWAT), 2015 International Workshop on.
2. Sotirios K. Goudos, Katherine Siakavara, John N. Sahalos, Life Fellow, IEEE "Novel Spiral Antenna Design Using Artificial Bee Colony Optimization for UHF RFID Applications", IEEE Antennas and Wireless Propagation Letters Vol. 13, 2014.
3. Iulian Rosu, "Microstrip, Stripline, and CPW Design", http://www.qsl.net/va3iul/.
4. Constandine A. Balanis, "Antennas Analysis and Design", 2005.
5. K. C. Gupta, R. Garg, I. Bahl, and P. Bhartia, "Microstrip Lines and Slotlines", Boston, Artech House, 1996.
6. Jia-Sheng Hong, M.J.Lancaster, "Microstrip Filters for RF Microwave Aplications", John Wiley and Sons, 2001.
7. "RFID Radio Frequency Identification", OECD Minosterial Meeting on the Future of the Internet Economy, 2008.
8. Ramiro A. Ramirez and Thomas M. Weller, "Dielectric-Loaded End-Fire Slot Antenna With Low Back-Lobe Radiation for UHF RFID Applications", International Workshop on Antenna Technology (iWAT), 2016
9. Tingqiang Wu, Hua Su, Liyun Gan, Huizhu Chen, Jingyao Huang, and Huaiwu Zhang, "A Compact and Broadband Microstrip Stacked Patch Antenna With Circular Polarization for 2.45-GHz Mobile RFID Reader", IEEE Antennas and Wireless Propagation Letters, Vol. 12, 2013.
10. Jinxi Chen and Sungkyun Lim, "An Unbalanced, Electrically Small Tag Antenna for Passive UHF RFID", SoutheastCon IEEE Conference, 2016.
11. Li Yang, Amin Rida, Rushi Vyas, Manos M. Tentzeris "RFID Tag and RF Structures on a Paper Substrate Using Inkjet-Printing Technology", IEEE Transactions on Microwave Theory and Technoques, Vol. 55, No. 12, 2011.
12. Kumar, P., Dwari, S., Saini, R. K., & Mandal, M. K. (2018). "Dual-Band Dual-Sense Polarization Reconfigurable Circularly Polarized Antenna". IEEE Antennas and Wireless Propagation Letters.
13. Keshwala, U., Rawat, S., Ray, K., Nair, N., & Yadav, S. (2018). "Compact circular monopole antenna with band notch characteristics for UWB applications ". 2018 5th International Conference on Signal Processing and Integrated Networks (SPIN).
14. Praveen Kumar Rao, Rajan Mishra (2018). "Multi Band Antenna with Multi Band Notch2.5/3.7/6.4/8.1/12.4/14.4GHz Characteristics". (2018) 5th IEEE Uttar Pradesh Section International Conference on Electrical, Electronics and Computer Engineering (UPCON).
15. https://en.wikipedia.org/wiki/C_band_(IEEE)

Tropospheric Propagation Modeling in the Modern Air Defense Environment

Th. Papastamatis[a], K. Ioannou[b], I. Koukos[c] and E. Papageorgiou[d]

[a]*Hellenic Air Force, Lieutenant & PhD Candidate, Aristotle University of Thessaloniki, Greece*

[b]*Hellenic Navy, Lieutenant Junior Grade & PhD Candidate, Aristotle University of Thessaloniki, Greece*

[c] *Combat Systems Sector, Hellenic Naval Academy, Piraeus, Greece*

[d] *Mathematics Sector, Hellenic Naval Academy, Piraeus, Greece*

Abstract. The threat faced by a modern Air Defense System has become very diverse. Traditional threats of bomber and fighter-bomber aircraft remain, but more nations are obtaining access to ballistic missiles and cruise missiles, which could attack from unexpected directions and in large numbers, saturating defenses. Advanced technologies for stealth and navigation are making the threat from conventional weapon systems even greater. Modern Air Defense Systems in the era of stealth aircraft become increasingly sophisticated in order to exploit the geographic aspect of the radiocoverage of the wide theater of operations. The monostatic radar of the 20th century will be replaced rapidly by hybrid multistatic clusters involving active and passive sensing of a multimode network centric Air Defense Model. Therefore the classic tropospheric propagation modeling has to be reexamined in order to optimize the radiocoverage of the defense networks that are confronted by stealthy aircrafts along with the weapons delivered. This paper reviews the advantages and the difficulties of safeguarding the effective operation of a defense network from an electromagnetic point of view.

Keywords: Refraction effects prediction, radar radio coverage.

ISSN:1791-4469

1. INTRODUCTION

Refraction is an omnipresent natural phenomenon occurring wherever there is a transmission medium of variable density which affects the velocity of a wave propagation. In the troposphere, the lowest part of the atmosphere named from the existence of weather phenomena which extend up to 10 km, the wireless transmission of signals either from radar or telecom transceivers is affected by refraction due to changes in the refractive index n that depends on the air temperature, pressure and humidity as shown in the ITU RECOMMENDATION ITU-R P.453-9 [5].

The refractive index n is defined as the ratio of the speed of radio waves in vacuum to the speed in the medium under consideration. The atmospheric radio refractive index, n, can be computed by the following formula**:**

$$n = 1 + N\ x\ 10^{-6} \tag{1}$$

where N is the radio refractivity expressed by:

$$N = N_{dry} + N_{wet} = \frac{77,6}{T}(P + 4810\frac{e}{T}) \tag{2}$$

The dry component N_{dry} of radio refractivity is given by

$$N_{dry} = 77,6\frac{P}{T} \tag{3}$$

and the wet component

$$N_{wet} = 3,732 \times 105\frac{e}{T^2} \tag{4}$$

where P is the atmospheric pressure (hPa), e is the water vapor pressure (hPa) and T is the absolute temperature (K). This expressions for frequencies up to 100 GHz contain error less than 0,5%, therefore are acceptable for use.

An atmosphere having a standard refractivity gradient $\frac{dN}{dh} = -40$, the effective radius of the Earth is about $4/3$ that of the actual radius, which corresponds to approximately 8 500 km and is called commonly as the "$4/3$ earth approximation".

The Standard radio atmosphere is defined as an atmosphere having the standard refractivity gradient. The refractivity gradient variations from the standard value -40 correspond to significant refractive phenomena severely affecting the electromagnetic ray paths. Thus we call **Sub-refraction** the refraction for which the refractivity gradient is greater (i.e. positive or less negative) than the standard refractivity gradient. Similarly we call **Super-refraction** the refraction for which the refractivity gradient is less (i.e. more negative) than the standard refractivity gradient.

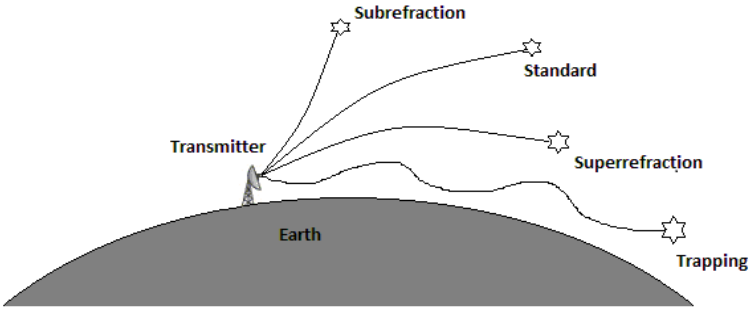

Figure 1. Types of refraction compared to the standard refraction with gradient = -40 corresponding to the 4/3 Earth Approximation

The trapping or ducting phenomenon occurs when overlapping atmospheric slabs rather reflect than refract rays ie. angle of refraction$a_i \leq 0^0$, because of abrupt temperature and pressure variations. Thus a ray is captured within a long path forming a parallel plate waveguide above the earth's surface that carries the electromagnetic wave far beyond line-of-sight distances. A duct is formed when temperature increases near surface abruptly (temperature inversion) or the humidity decreases (moisture lapse) with height.

A radar processor measures target ranges assuming straight line ray propagation. Because of ray bending that is not a correct assumption, thus radar senses only an apparent range and an apparent angle of elevation that differ from their true values as indicated in the Figure 2 below:

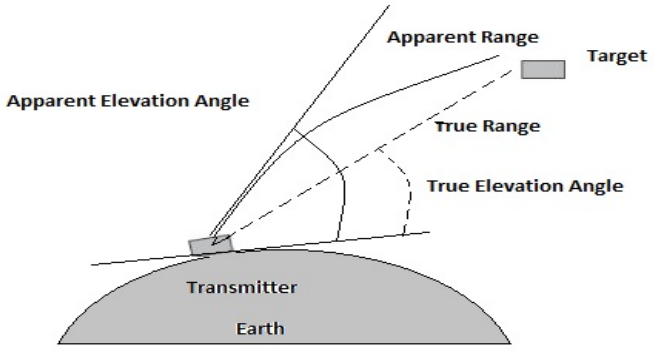

Figure 2. Apparent Target Range and Angle of Elevation due to ray bending as compared to True Values assuming (nonexistent) straight ray propagation

The calculation of the induced range and elevation errors is depicted in Figure 3.

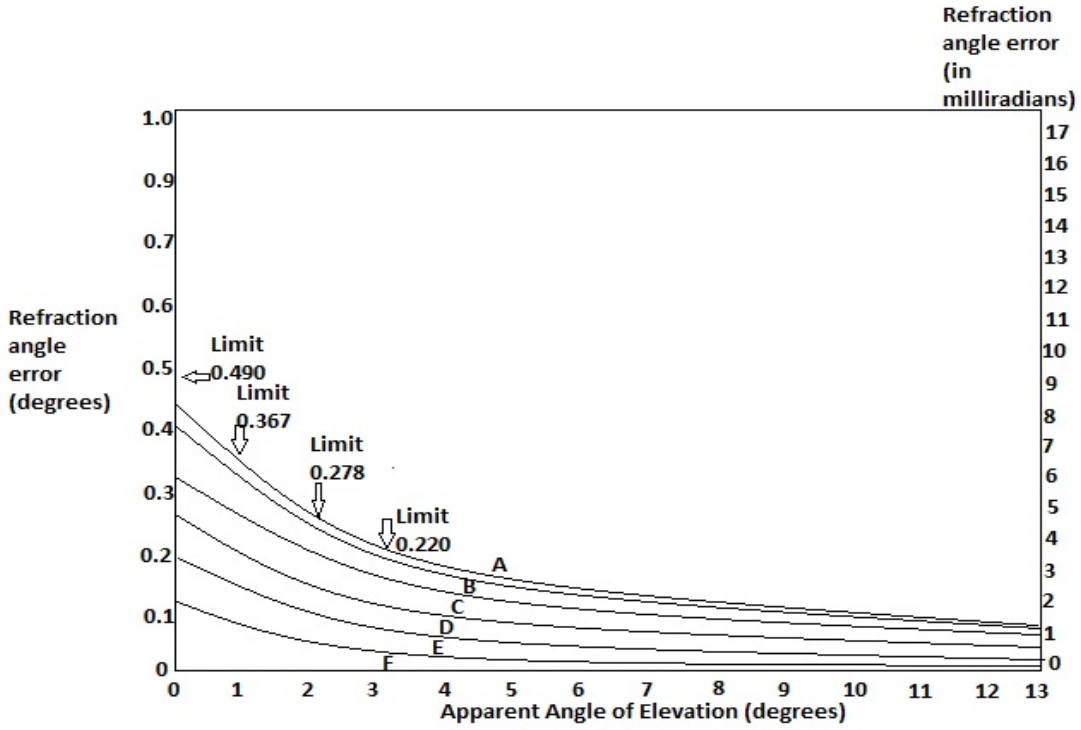

Figure 3. Normal refraction errors in range (right axis) and angle (left axis) vs apparent angle of elevation

In the ITU-R P.453-9 recommendation the long-term mean dependence of the refractive index n upon the height h is well expressed by an exponential law:

$$n(h) \;=\; 1 + N_0 \times 10^{-6} \times e^{-\frac{h}{h_0}} \tag{5}$$

where, N_0 is the average value of atmospheric refractivity extrapolated to sea level and h_0 is the scale height (km). N_0 and h_0 can be determined statistically for different climates. For reference purposes a global mean of the height profile of refractivity may be defined by: $N_0 = 315$ and $h_0 = 7.35$ Km.These numerical values apply only for terrestrial paths. This reference profile may be used to compute the value of refractivity N_s at the Earth's surface from N_0 as follows:

$$N_s = N_0 \times e^{-\frac{h_s}{h_0}} \tag{6}$$

Where, h_s= height of the Earth's surface above sea level (km).
In order to examine the N gradients, the modified refractivity index issued. It is defined as:

$$M = \left(n - 1 + \frac{h}{R_e}\right) \times 10^6 = N + 0{,}157 \tag{7}$$

The computation of the refractive conditions, characterized as Subrefraction, Standard, Superrefraction and Trapping is achieved by its gradient $\frac{dM}{dh}$ as shown in the table below. Tropospheric ducting phenomena occur when either inequality $\frac{dM}{dh} < 0$ or $\frac{dN}{dh} < -157$ is satisfied.

Refraction	**Sub-refraction**	**Standard**	**Super-refraction**	**Trapping**
$\frac{dM}{dh}, \frac{M-Units}{km}$	$\frac{dM}{dh} < 157$	$78 < \frac{dM}{dh} \leq 157$	$0 < \frac{dM}{dh} \leq 78$	$\frac{dM}{dh} \leq 0$
$\frac{dN}{dh}, \frac{N-Units}{km}$	$\frac{dN}{dh} > 0$	$-79 < \frac{dN}{dh} \leq 0$	$-157 < \frac{dN}{dh} \leq -79$	$\frac{dN}{dh} \leq -157$

Table 1. Computation of the refractive conditions, characterized as Subrefraction, Standard, Super-refraction and Trapping

Of great importance for radar propagation near sea surface are the evaporation ducts. An evaporation duct is a tropospheric phenomenon that primarily occurs immediately above the surface of the sea and other large bodies of water and exists because the amount of water vapor present in the air decreases rapidly with height in the first few meters above the surface of the water. By virtue of its nature of formation, an evaporation duct is a nearly permanent feature. The height of an evaporation duct is typically of the order of only a few meters (the world average evaporation duct height is reported to be approximately 13 m, however this can vary considerably with geographical location and changes in atmospheric parameters such as humidity, temperature and wind speed. The evaporation duct height is often used as an indicator of its strength and its ability to trap radio waves [2].

2. A DIFFERENT APPROACH OF MODELING THE REFRACTION INDEX VARIATIONS ON RADIOWAVE PROPAGATION

It has been observed that in the troposphere, the relative dielectric constant is slightly higher than unity due to the presence of the atmosphere and, in particular, water vapor. The tropospheric region extends from the surface of the earth to a height of about 6 km at the poles and 18 km at the equator. The relative dielectric constant is a function of the temperature, pressure, and humidity (or water vapor pressure). The typical value of $\varepsilon_r$at the surface of the earth is found to be 1.000579 [1]. The value decreases as a function of height above the surface of the earth.

ISSN:1791-4469

$$v = \frac{c}{\sqrt{\varepsilon_r}} = \frac{c}{n} \tag{8}$$

where c is the velocity in vacuum and $n = \sqrt{\varepsilon_r}$ is the refractive index of the medium. At the surface of the earth (mean sea level), the refractive index of air is 1.000289. Therefore, it is common practice to work with a parameter known as the refractivity, N. The refractivity is related to refractive index by the following equation.

$$N = (n - 1) \times 10^6 \tag{9}$$

Thus, at the surface of the earth, the refractivity is equal to 289. For a standard atmosphere, the refractivity falls off linearly up to a height of 2 km above the surface of the earth and is expressed by the following equation

$$N = 289 - 39h \tag{10}$$

where h is the height in km. This is known as the standard atmosphere or normal atmosphere. The refractive index of the standard atmosphere is given by

$$n = 1 + (289 - 39h) \times 10^6 \tag{11}$$

Let us now derive an equation for the path of a wave propagating in a medium wherein the refractive index is a continuous function of height. For this derivation, let us assume that the earth is flat and the troposphere is made up of stratified layers parallel to the surface of the earth, i.e., the refractive index is a function of height only. Let the refractive index be a constant within each layer. Consider a layer that has a height dh with refractive index $(n + dn)$ (Figure 4). A ray incident from the lower layer at point P is refracted through the layer dh and touches the upper layer at point Q. Let θ be the angle of incidence with the normal drawn to the plane at P and $(\theta + d\theta)$ be the angle of refraction at$P$. In order to calculate the radius of curvature r, of the ray, draw angle bisectors at $P$and Q. Let them meet each other at O. From the inset in Fig. 4

$$\angle APQ = \pi - d\theta \tag{12}$$

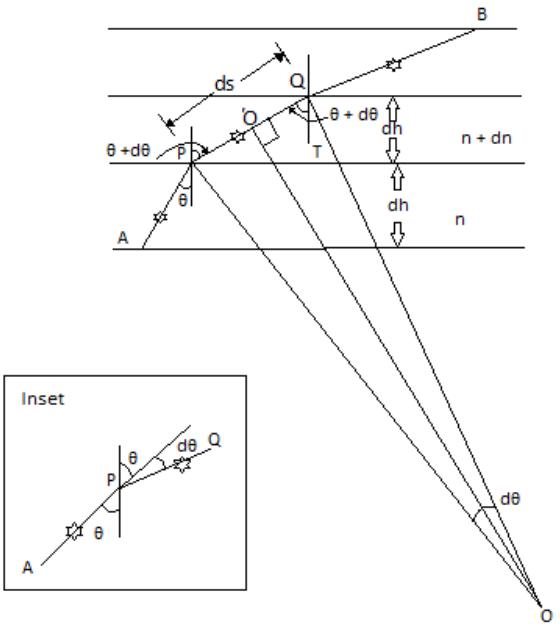

Figure 4. Wave propagation in a stratified medium

Since OP bisects $\angle APQ$

$$\angle OPQ = \frac{1}{2}\angle APQ = \frac{\pi}{2} - \frac{d\theta}{2} \tag{13}$$

Draw O′O perpendicular to PQ. In $\Delta PO'O$

$$\angle PO'O = \frac{\pi}{2} - \angle OPQ = \frac{d\theta}{2} \tag{14}$$

The angle subtended by the segment ds at O is

$$\angle OPQ = 2\angle PO'O = d\theta \tag{15}$$

and hence the length ds is given by

$$ds = rd \tag{16}$$

From ΔPQT

$$ds = \frac{dh}{\cos(\theta+d\theta)} \cong \frac{dh}{\cos\theta} \text{ for small } d\theta \tag{17}$$

Substituting the value of ds from Equation (16) into Equation (17)

ISSN:1791-4469

$$r = \frac{ds}{d\theta} = \frac{dh}{cos\theta d\theta} \tag{18}$$

The law of refraction can now be applied to the two points P and Q

$$nsin\theta = (n + dn)\sin(\theta + d\theta) \tag{19}$$

Expanding the right hand side

$$nsin\theta = (n + dn)(sin\theta cosd\theta + cos\theta sind\theta) \tag{20}$$

which can be written as

$$cos\theta d\theta = -\frac{sin\theta dn}{n} \tag{21}$$

Substituting Equation (21) in Equation (18)

$$r = \frac{dh}{-sin\theta\frac{dn}{n}} = \frac{n}{sin\theta(-\frac{dn}{dh})} \tag{22}$$

The radius of curvature can also be written in terms of the grazing angle, φ.This is the angle that the ray makes with the horizontal and is related toθ by the equation

$$\theta = \frac{\pi}{2} - \varphi \tag{23}$$

The radius of curvature can be written in terms of φ as

$$r = \frac{n}{cos\varphi(-\frac{dn}{dh})} \tag{24}$$

Consider a ray launched with a low grazing angle,$(\varphi \cong 0)$, for which $cos\varphi \cong 1$. Since the refractive index is also very close to unity, the radius of curvature reduces to

$$r = \frac{1}{-\frac{dn}{dh}} \tag{25}$$

We can express the radius of curvature in terms of the refractivity gradient, dN/dh, as

$$r = \frac{10^6}{-\frac{dN}{dh}} \tag{26}$$

If this ray is propagating in the standard atmosphere described by the refractivity profile given by Equation (10), we have

$$\frac{dN}{dh} = -39/km \tag{27}$$

and the radius of curvature of the ray path is

$$r = \frac{1}{39\times10^{-6}} \cong 25641km \tag{28}$$

The ray droops towards the surface of the earth. If the refractivity does not change with the height, that is, $dN/dh = 0$, the radio wave does not undergo refraction hence it follows a straight

line path. Figure 5 depicts the propagation of a radio wave launched at low grazing angles for various values of refractivity gradients (dN/dh). If the refractivity gradient is between 39/km and 0, the refraction of the electromagnetic wave is lower than that in the standard atmosphere and is known as sub-refraction. If the refractivity slope is less than that of the standard atmosphere, i.e., $dN/dh < -39/km$the wave is refracted more than that in a standard atmosphere and is known as super refraction. For $dN/dh = -157/km$, the radius of curvature of the ray is

$$r = \frac{1}{157\times10^{-6}} \cong 6370km \tag{29}$$

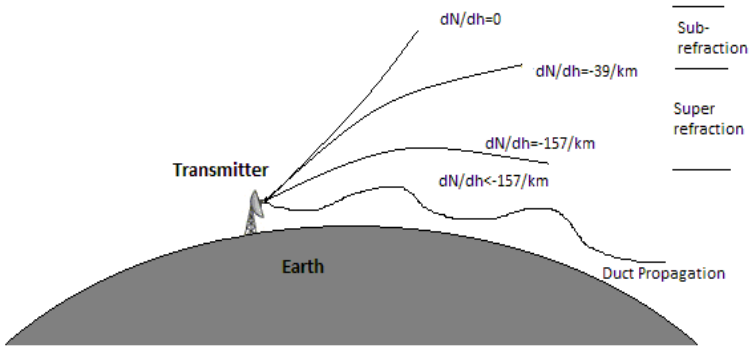

Figure 5. Wave propagation through a stratified medium above the spherical earth

which is equal to the radius of the earth, and hence a horizontally incident wave travels parallel to the surface of the earth. If $dN/dh = -157/km$, the radius of curvature of the ray is smaller than the radius of the earth. The ray can, therefore, touch the surface of the earth and get reflected from the surface. This is known as tropospheric duct propagation. The regions corresponding to sub-refraction, super refraction, and duct propagation are shown in Figure 6 on an $N - h$ plot. On a spherical earth, the maximum possible direct wave communication distance depends on the heights of the transmit and the receive antennas as well as the atmospheric conditions. For propagation calculations, a mean value of $r_0 = 6370km$ is chosen to be the radius of the earth. With $dN/dh = 0$, the radio waves travel along straight lines. Therefore, the maximum range is obtained when the straight line, joining the two antennas, grazes the surface of the earth.

ISSN:1791-4469

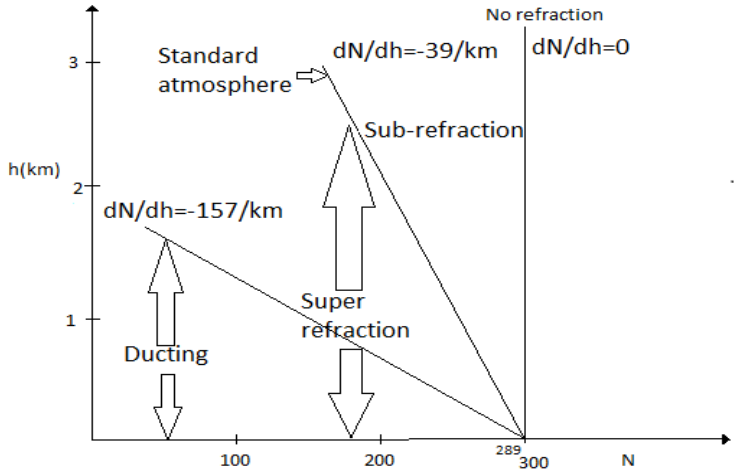

Figure 6. Depiction of regions of super refraction, sub-refraction, and duct propagation on an N-h plot.

3. PARABOLIC EQUATION MODELING

In this section we apply the finite-difference scheme of the Crank-Nicolson type on the Parabolic Equation [4] [7]. This technique permits the modelling with arbitrary boundaries.For the sake of initial simplicity, we choose to work with range vs height coordinates (x, z) assuming that the transverse coordinate y presents no variations on its own in the electromagnetic fields.The electric field E has only one non-zero component E_y, in horizontal polarization, while the magnetic field H has only one non-zero component H_y in vertical polarization. Thus we form a general variable field component ψ defined as $\psi(x,z) = E_y(x,z)$ for horizontal polarization or $\psi(x,z) = H_y(x,z)$ for vertical polarization. We assume a domain where the refractive index $n(x,z)$ has smooth variations, with suitable boundary conditions.We solve the wave equation where energy propagates at small angles from a preferred direction, called the paraxial direction. Let's choose the positive x-direction as the paraxial direction as shown in Figure 7.

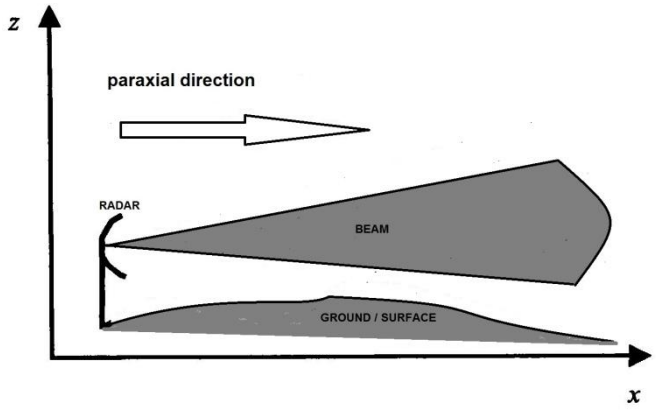

Figure 7. Tropospheric propagation of a radar beam in the x-paraxial direction [7]

For a homogeneous propagation medium with refractive index n, the field component ψ variations are modeled with a two-dimensional scalar wave equation:

$$\frac{\partial^2\psi}{\partial x^2} + \frac{\partial^2\psi}{\partial z^2} + k^2 n^2 \psi = 0 \tag{30}$$

where k is the wave number in vacuum. In reality, the refractive index varies with range x and height z, so the above equation is not accurate, but we use it as a first good approximation if the variations of n are slow compared to a wavelength. To further proceed in solving Equation (30) we introduce an auxiliary variable $u(x,z) = e^{-ikx}\psi(x,z)$ slowly varying in range for signal propagating at angles close to the paraxial direction, forming a new equation with convenient numerical properties :

$$\frac{\partial^2 u}{\partial z^2}(x,z) + 2ik\frac{\partial u}{\partial x}(x,z) + k^2(n^2(x,z) - 1)u(x,z) = 0 \tag{31}$$

The solution for the above equation is the numerical values that u takes on a grid of (x,z) values placed over the domain. The u is assumed to be smooth almost everywhere such that it gets values for arbitrary x, z. The domain that we will work on is rectangular with x ranging from x_{min} to x_{max} and z ranging from 0 to N. Divide the intervals $[0, N]$and $[x_{min}, x_{max}]$ to J and N equally subintervals respectively. The length of these intervals is m in the z direction and h in the x direction. We denote with u_j^n the approximation at the grid point where $x_n = x_{min} + nh$, $z_j = jm$. To avoid the case that the numerical solution would be unstable we use the Crank-Nicholson algorithm that is unconditionally stable and also is second order accurate in both the x and z directions. The algorithm uses difference expressions for the partial derivatives that are centered around $x + \frac{h}{2}$ rather than around x. Thus the u, u_{zz} are averages of values of PE equation at time $n - 1$ and n.

ISSN:1791-4469

$$u = \frac{u_j^{n-1} + u_j^n}{2} \tag{32}$$

$$\frac{\partial u}{\partial x} \approx \frac{u_j^n - u_j^{n-1}}{h} \tag{33}$$

$$\frac{\partial^2 u}{\partial z^2} \approx \frac{u_{j+1}^n + u_{j-1}^n - 2u_j^n}{m^2} \tag{34}$$

Substituting the above equations into the equation (30), we have

$$\frac{u_{j+1}^n + u_{j-1}^n - 2u_j^n}{m^2} + 2ik\frac{u_j^n - u_j^{n-1}}{h} + k^2\left(n^2(x_n, z_j) - 1\right)u_j^n = 0 \tag{35}$$

To above equations we suppose that

$$b = 4ik\frac{m^2}{h} \tag{36}$$

$$a_j^n = k^2\left(n^2(x_n, z_j) - 1\right)m^2 \tag{37}$$

So we have

$$u_j^n(-2 + b + a_j^n) + u_{j+1}^n + u_{j-1}^n = u_j^{n-1}\left(2 + b - a_j^n\right) - u_{j+1}^{n-1} - u_{j-1}^{n-1} \tag{38}$$

For $j = 1 \cdots N - 1$. The above system will be written in more convenient structure in matrix form,

$$\begin{pmatrix} 1 & 0 & 0 & \cdots & 0 & 0 \\ 1 & a_1^n & 1 & \cdots & 0 & 0 \\ 0 & 1 & a_2^n & \cdots & 0 & 0 \\ \vdots & \vdots & \vdots & \cdots & \vdots & \vdots \\ 0 & 0 & 0 & \cdots & a_{N-1}^n & 1 \\ 0 & 0 & 0 & \cdots & 0 & 1 \end{pmatrix} \begin{pmatrix} u_0^n \\ u_1^n \\ u_2^n \\ \vdots \\ u_N^n \end{pmatrix} = \begin{pmatrix} 1 & 0 & 0 & \cdots & 0 & 0 \\ -1 & b_1^n & -1 & \cdots & 0 & 0 \\ 0 & -1 & b_2^n & \cdots & 0 & 0 \\ \vdots & \vdots & \vdots & \cdots & \vdots & \vdots \\ 0 & 0 & 0 & \cdots & b_{N-1}^n & -1 \\ 0 & 0 & 0 & \cdots & 0 & 1 \end{pmatrix} \begin{pmatrix} u_0^{n-1} \\ u_1^{n-1} \\ u_2^{n-1} \\ \vdots \\ u_N^{n-1} \end{pmatrix} \tag{39}$$

This system is easier to be solved by Gaussian elimination.

4. OTHER MODELING SCHEMES

Defense radar applications require predictions of the electromagnetic field variability in very large regions, up to several hundreds of km in range and several km in height. As Parabolic Equation (PE)integration times depend on frequency, propagation angles and domain size, calculations become prohibitively complex for such large domains. However, for most tropospheric problems, severe variations of the atmospheric refractive index never exist above a kilometre or so, and terrain irregularities are often limited to low altitudes resulting in

perturbations of the propagation medium to be usually confined in height. Also since the refractive index of the air remains very close to unity, anomalous atmospheric refraction effects are limited to small propagation angles from the horizontal. Thus we reserve the powerful, but relatively slow PE modeling for field calculations at low heights and propagation angles, and to use faster methods of solving at other angles and heights of interest.

The Radio Physical Optics (RPO) model [3] combines ray optics and parabolic equation methods to accelerate computations for propagation over flat terrain. The domain is dividedinto four regions, as shown in Figure 7. In the flat Earth region, a simple two-ray model is used, assuming the rays propagate in straight lines. The idea here is that refractive effects are negligible for rays launched at angles of more than a few degrees from the horizontal (a threshold value of 5° is proposed in [3]), and there is hence no point in using more expensive ray-tracing algorithms. This modeling has been employed in the Advanced Propagation Model (APM) used by the software packet AREPS (Advanced Refraction Effects Prediction System) of SPAWAR, San Diego, California. The AREPS program computes and displays a number of electromagnetic (EM) system performance assessment tactical decision aids. These are radar probability of detection, electronic surveillance measure (ESM) vulnerability, HF to EHF communications, simultaneous radar detection and ESM vulnerability, and surface-search detection ranges.

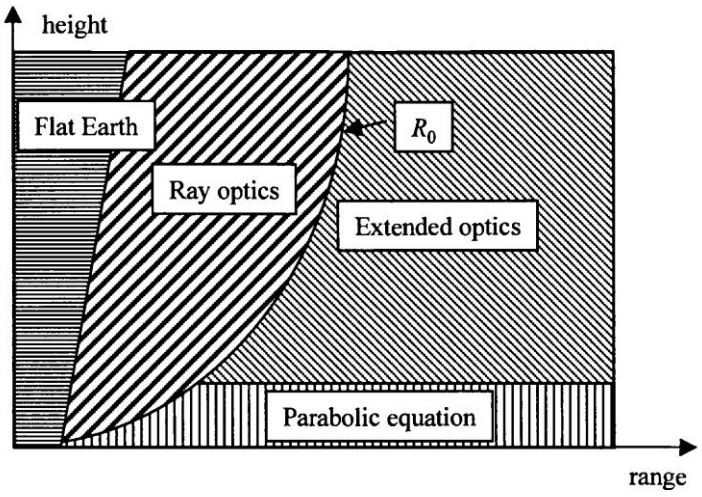

Figure 8. Regions used in AREPS [6].

5. CONCLUSIONS

Refraction or the bending of RF energy if not accounted for, can severely impact the performance of surface, littoral, naval or airborne radar and communication systems in a combat environment. These impacts influence operations, acquisition engineering, and prototype RF system testing. By combining modern numerical weather prediction models with RF system models, it is possible to create site and time-specific RF system performance forecasts that will ensure the survivability of any operating system in the future theatre of operations. Extensive numerical modeling leads to solutions that need to be validated with real time far field measurements of radar detection performance against target drones with known stereocopic RCS profiles.

REFERENCES

1. D. Griffiths, “Introduction to Elementary Particles”, 1987 John Wiley & Sons, Inc.
2. S. D. Gunashekar et al, “Long-term statistics related to evaporation duct propagation of 2 GHz radio waves in the English Channel”, http://onlinelibrary.wiley.com/doi/10.1029/2009RS004339/full.
3. H.V. Hitney, "Hybrid ray optics and parabolic equation methods for radar propagation modeling", Proceedings of Radar 92, IEE Conf. Pub., no. 365, pp. 58-61, 1992
4. S. A. Isaakidis and T. D. Xenos, “Parabolic Equation Solution of Tropospheric Wave Propagation Using FEM.” Progress In Electromagnetics Research, PIER 49, 257–271, 2004.
5. ITU RECOMMENDATION ITU-R P.453-9 : The radio refractive index: its formula and refractivity data.
6. W. L. Patterson, “Advanced Refractive Effects Prediction System (AREPS)”, SSC San Diego
7. M. Levy, Parabolic equation methods for electromagnetic wave propagation, IEE, 2000.

Performance analysis of wireless RF communication relay channels over a sea environment in a geographical area of an archipelagos

K. Ioannou[a], A.N. Stassinakis[b],Th. Papastamatis[c], I. Koukos[d] and T. Xenos[e]

[a] *Hellenic Navy & Aristotle University of Thessaloniki, Greece*
[b] *Department of Electronics, Computers, Telecommunications and Control, Faculty of Physics, National and Kapodistrian University of Athens.*
[c] *Hellenic Air Force, First Lieutenant, & PhD Candidate, Aristotle University of Thessaloniki, Greece.*
[d] *Combat Systems Sector, Hellenic Naval Academy, Piraeus, Greece.*
[e] *Aristotle University of Thessaloniki, Greece.*

Abstract: It is widely known that the wireless communication between stations that exist and operate in a maritime environment has many factors to overcome in order to reach a certain high level of Quality of Service (QoS), especially when it has to do with military applications, such as the weather conditions, the distance between the stations e.t.c. Modern approaches for the solution of the abovementioned malfunctions are the use of satellites and the use of more than one receiving antennas. In this paper, the performance analysis of Single Input Single Output (SISO)and Single Input Multiple Output (SIMO)communication relay links will be investigated taking into consideration the interaction between the Bit Error Rate (BER), the Bit Rate and the Signal to Noise Ratio (SNR) for the type of multiplexing and modulation of the transmitted signal. The main objective is the need to mitigate the effect of the multipath propagation over the wireless wideband maritime communication channel. Moreover, in this work is examined the use of Unmanned Air Systems (UAS) as relay nodes in order to overcome possible obstacles that prevent the communication between stations and to extend the coverage of a communication link.

Keywords: Wideband maritime communication channel, SISO, SIMO, UAS, Multipath effect.

1. Introduction

Modern wireless RF communication networks are rapidly introduced in military operation theaters due to the advantages they offer, such as Line Of Sight (LOS), non-LOS connectivity and high speed secure data communications[1, 2, 3, 4, 5] . On the other hand, wireless RF

ISSN:1791-4469

systems suffer from various factors that degrade their performance. The main factor is multipath effect, where the information signal arrives at the receiver many times but in different time slots following different trajectories due to reflections or refractions in the troposphere. Furthermore, the presence of obstacles, inside the Fresnel Zone, between the transmitter and the receiver, is responsible for performance deterioration of the communication system [3, 6, 7, 8, 9, 10, 11].

In order to increase the performance of the communication systems, various techniques have been proposed. The most effective is the use of multiple antennas at the receiver (SIMO) or the transmitter (Multiple Input Single Output, MISO) due to differential reception [12, 13, 14, 15]. Another technique used to avoid obstacles, is multihop communications, where transceiver nodes are placed between the transmitter and the receiver [11,16, 17, 18].

In this work, the reliability of a multihop SIMO system will be investigated under multipath effect and it will be estimated using the Rayleigh distribution. It is well known that using the Rayleigh distribution is achieved to create a model of the communication scheme when the signal is scattered from particles that exist in the environment (such as the sea waves) [9, 19]. In addition to this, due to the fact that the Rayleigh distribution describes fast fading statistics in the region of troposphere scattering waves, therefore it is more useful for communication during military operations. The communication system will imply the Orthogonal Frequency Division Multiplex (OFDM) which is an effective technique for broadband communication schemes and every subcarrier will be modulated using Quadrature Amplitude Modulation (QAM) [9, 20, 21, 22]. The metric that will be investigated, is the BER which is very important, as it indicates the reliability of the system. For Frequency Hopping (FH) a mechanism must be designed so that the data can be transmitted in a clear channel and avoid channel congestion [23, 24, 25, 26]. Compared to a narrowband signal, Spread Spectrum (SS) spreads the signal power over a wideband and the overall SNR is improved because only a small part of the signal is affected by interference. In a communication system, in both transmitter and receiver sides, one spreading generator has been located which, based on the spreading technique, they synchronize the received modulated spectrum. Employing the FHSS technology privacy, QoS is improved as it is difficult for the signal to be intercepted, the interference and multipath fading (distortion) is decreased whereas the signal capacity is increased, the SNR is improved, the efficiency of bandwidth is high and finally, this transmission can share a frequency band with many types of conventional transmissions with minimal interference.

2. System Model

The system consists of two warships that, due to obstacle between them that makes direct communication impossible, may communicate using a UAS creating a dual hop system. The UAS is assumed to be a Decode and Forward relay (DF) node, as it receives the direct and the overheard signals from the transmitter, it decodes them and then forwards them to the receiver.

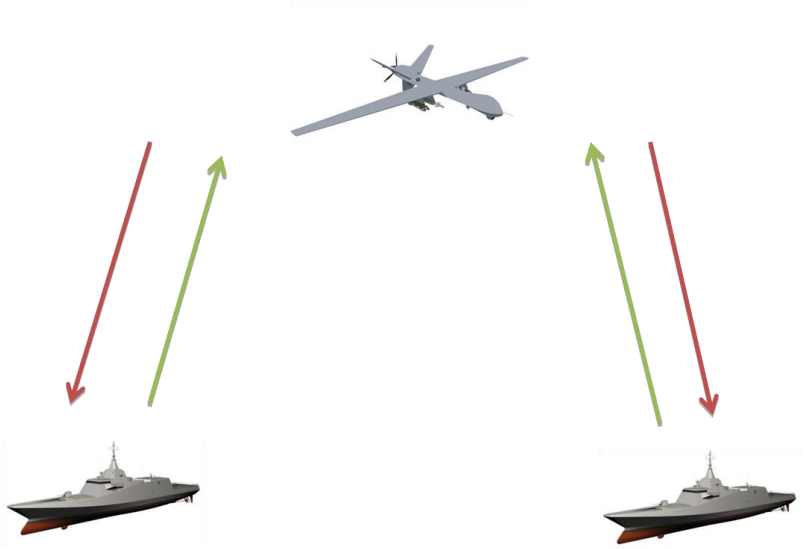

Fig. 1: UAS as relay communication node.

However the presence of this obstacle may still affect the performance of the system creating multipath effect. This effect can be investigated using various statistical distributions. In this work the Rayleigh distribution is employed since there is no dominant propagation along a LOS between the transmitter and receiver. The Probability Density Function (PDF) is given by the following equation [9, 19]:

$$P(\gamma)=\begin{cases}\dfrac{\gamma}{\sigma^2}e^{-\frac{\gamma^2}{2\sigma^2}}, & \gamma>0\\ 0, & \gamma\le 0\end{cases} \tag{1}$$

where γ is the envelope amplitude of the received signal and σis the standard deviation[8]. Furthermore, the system is assumed to employ the OFDM technique in order to eliminate the intersymbol interference (ISI), a very important factor that degrades the performance of an RF system. In OFDM, the transmitted signal will be given by the following equation [3, 9, 21, 22]:

$$x_l(t)=\sum_{k=\frac{N_s}{2}}^{\frac{N_s}{2}-1} S_{l,k}\,g(t-((i+1)T_s))\exp(j2\pi f_k t) \tag{2}$$

where N_s is the length of the block that $S_{l,k}$ complex symbols create, T_s is the period of one symbol and f_k is the frequency of the *k*th subcarrier.

Every subcarrier of the OFDM transmitted signal will be modulated using the QAM technique and the result will be given by the following equation [3, 9, 21, 22]:

$$s_m(t)=Am_i g(t)\cos 2\pi f_c t - Am_q g(t)\sin 2\pi f_c t, m=1,2,...,\mathrm{M} \tag{3}$$

ISSN:1791-4469

Moreover, in order to avoid greater obstacles, such as islets, and therefore extend the communication range between the transmitter and the receiver, the multihop technique can be applied using multiple UAS as DF relay nodes, where N is the number of the UAS employed. In this case the final structure is (Fig. 2):

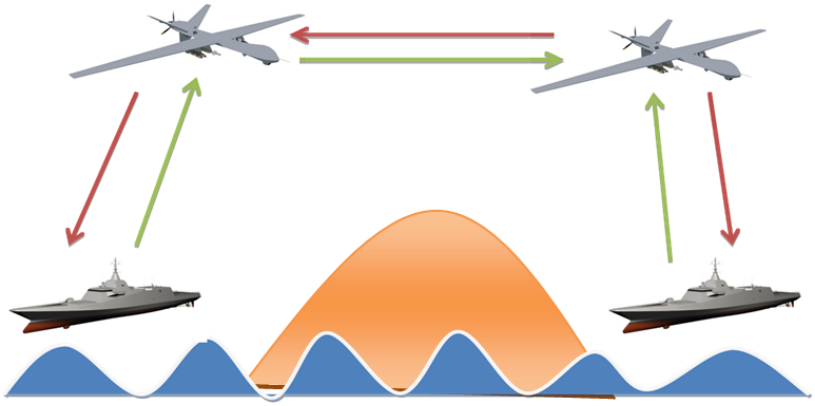

Fig. 2: UAS as relay DF node.

A cooperative multihop communications scheme is described in Fig.3:

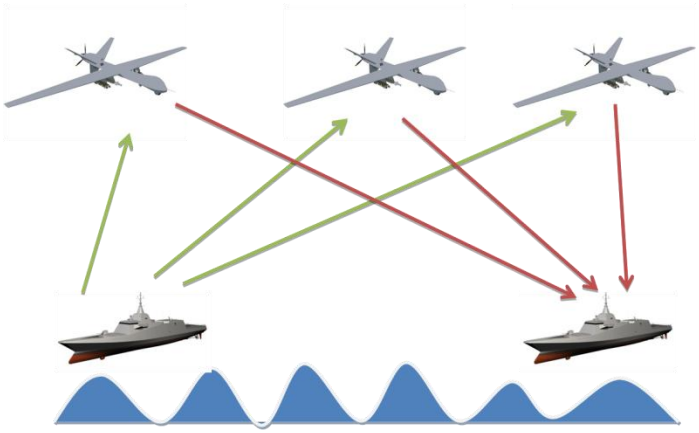

Fig. 3: Cooperative multihop communication scheme using 3 UAS as relay DF nodes.

The transmitter using N UAS as independent transponders, ensures that the receiver will get good signal quality, at least through one of the UAS. Moreover, this scheme works complementarily, as if one of the UAS gets destroyed or intercepted, the communication between the two warships will not break down. On the other hand, the receiver has to process all N received signals in order to obtain the information sent either by the cancelation or the superposition of the N received messages.

Instead of the simple SIMO technique, cooperative multihop scheme may be used, because in the simple multihop technique obstacles may be avoided, but degradation of the quality of the received signal, caused by the hops from UAS to UAS will be observed. Moreover, the more the nodes used, the better the system performance achieved, as long as, for a specific value of SNR, the BER decreases as the number of UAS increases.

Using the FHSS technique, the frequency of the carrier gets changed under a certain rate. Furthermore, Adaptive Frequency Hopping is implemented against frequency interference by avoiding congested frequency channels to be used in hopping sequence.

FH occurs over a frequency bandwidth covering numerous channels and is categorized into slow hopping and fast hopping. During slow hopping, more than one data symbol is transmitted in the same channel, whereas in the case of fast hopping, frequency changes several times per symbol. The hopping spectrum is called total hopping bandwidth. To generate a hopping sequence number as the channel number, that uplink "receiver" sends this number as feedback to downlink "transmitter", which can be shown in a linear equation [13] and assuming binary transmission the capacity of the feedback block is [23, 24, 26]:

$$C_f = N_a \log_2 N + C_{OH} + R_x \quad (4)$$

where N is the total available channels, N_a are the active channels, C_f are the chips on feedback, C_{OH} is the feedback overhead and R is the chip rate.

A general model of SS digital communication system can be seen in the following Fig:

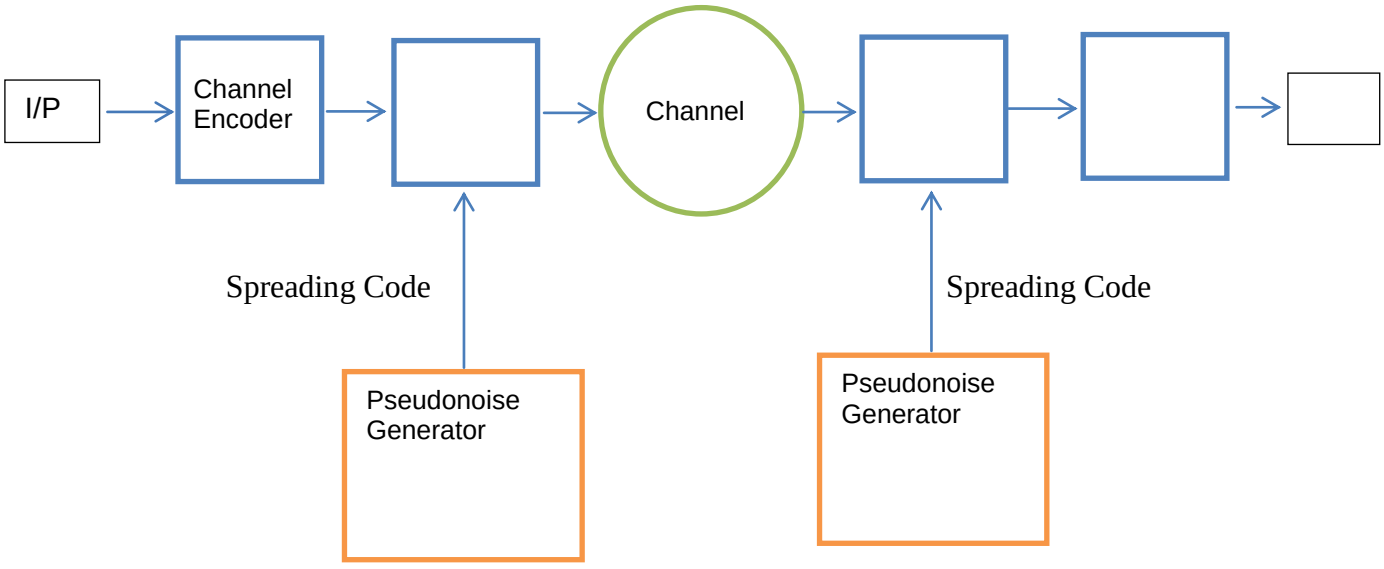

Fig. 4: A general model of SS digital communication system.

Taking advantage of all the above characteristics of the communications system proposed, we can proceed to the analysis of a SIMO system [15]. In a SIMO spatial divert system, one transmitter will send data to a number of receivers that present total aperture surface equal to the receiver of the SISO occasion.

3. Performance of multihop SISO system

Taking the *k*-th subband of the M-QAM modulation using the Rayleigh distribution, the BER of the Symbol Error Rate (SER) is given by [21, 27]:

$$\mathrm{P} = \int_0^{\infty} \{1-[1-\frac{2(\sqrt{M}-1)}{\sqrt{M}} Q(\sqrt{2\gamma})]^2\} \mathrm{p}(\gamma) d\gamma, \tag{5}$$

where Q(x) is the Gaussian tail function and γ is the SNR. Then, using equations (1) to (3) we can compute the BER of M-ary QAM in Rayleigh channel which is:

$$P_k = \prod_{k=1}^{N} \{\frac{M-1}{M \log_2 M}\left[1-\sqrt{\frac{(3\gamma_k \log_2 M)/(\mathrm{M}^2-1)}{[(3\gamma_k \log_2 M)/(\mathrm{M}^2-1)]+1}}\right]\} = \prod_{k=1}^{N} P_e(SISO) \tag{6}$$

In case N-UAS are employed as relay nodes, the BER can be calculated using the following equation [11, 17, 18] :

$$P_H = \sum_{i=1}^{H} [P(\mathrm{i}) \prod_{j=i+1}^{H} (1-2\,\mathrm{P(j)}), \tag{7}$$

where H is the number of the hops.

4. SIMO systems

A SIMO system is a spatial diversity technique where the signal is transmitted from a single transmitter to multiple (N) receivers. In this case, the probability of error will be given as [21]:

$$P_s = Q(\sum_{k=1}^{N} \sqrt{2\gamma_k})] \ . \tag{8}$$

So the BER will be given by:

$$\mathrm{P}_k = \int_0^{\infty} \{1-[1-\frac{2(\sqrt{M}-1)}{\sqrt{M}} Q(\sum_{k=1}^{N} \sqrt{2\gamma_k})]^2\} \mathrm{p}(\gamma_k) d\gamma_k \tag{9}$$

Finally, executing the integral of equation (9) and applying

$$Q(x) = \frac{1}{2} e^{-\frac{x^2}{2}} \tag{10}$$

equation (9), results in

$$P_k = \prod_{k=1}^{N} \{ \frac{M-1}{M \log_2 M} \left[1 - \sqrt{\frac{(3\gamma_k \log_2 M)/(\mathrm{M}^2-1)}{[(3\gamma_k \log_2 M)/(\mathrm{M}^2-1)]+1}} \right] \} = \prod_{k=1}^{N} P_e(SISO) . \tag{11}$$

5. Numerical Results

In this section the numerical results of the Multihop OFDM QAM system are presented.

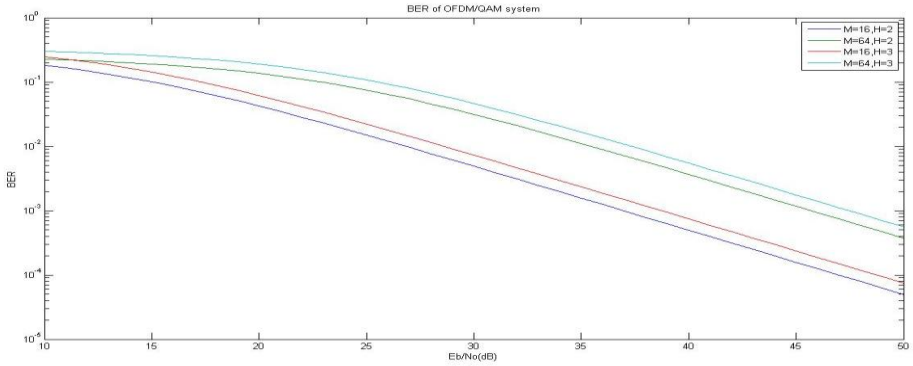

Fig 5: BER-Eb/No of OFDM/QAM SISO system.

In Fig. 5 a 16-QAM and a 64-QAM OFDM system are compared in terms of BER and Eb/No (SNR),where Eb is the energy per bit of the signal and No is the power of the noise . As it can be derived from Fig. 5,for both systems, as SNR increases, BER decreases and the system shows better performance, but needs more power to operate. In addition to this, for a certain value of SNR (i.e. 30 dB), as M increases, BER increases too and the system is less efficient. Moreover, as M increases the performance of the system deteriorates because the Euclidian distance between the points of the modulation constellation is more dense and there is high probability of error during the transmission.

Another aspect examined, is the number of UAS used. In dual-hop systems, (H=2) one UAS is used whereas in multihop systems two or more UAS are employed (e.g. H=3). It is obvious that the more the hops deployed, the higher the BER is, but longer distances of communication between the transmitter and the receiver can be achieved (beyond LOS).

ISSN:1791-4469

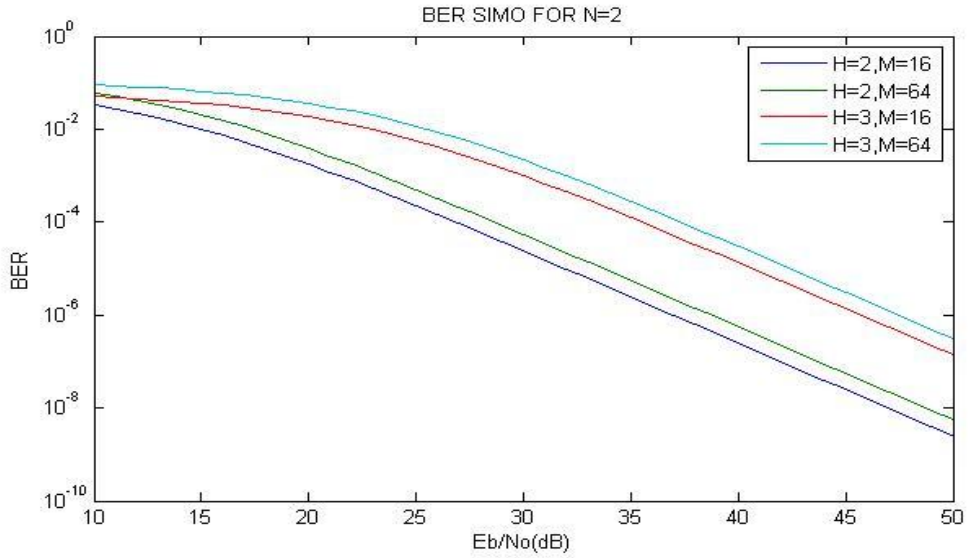

Fig 6: BER SIMO system for N=2

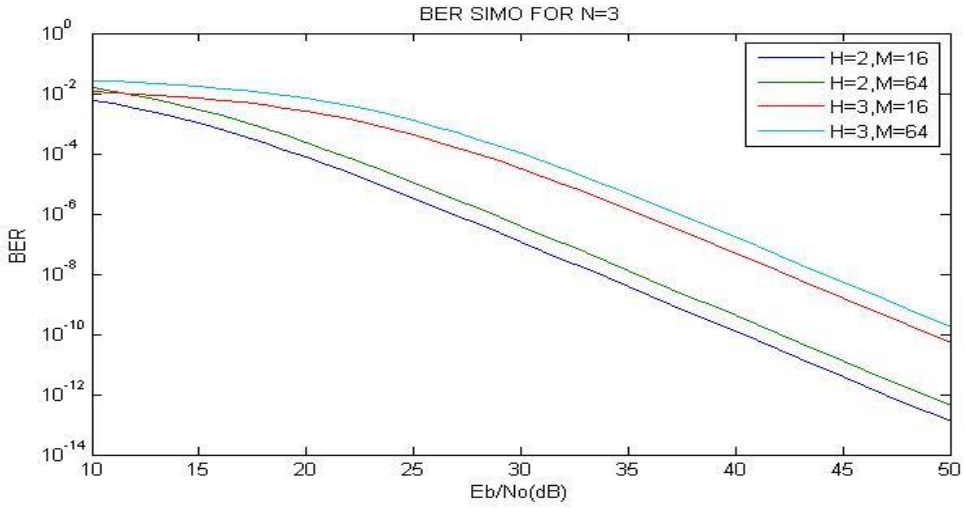

Fig 7: BER SIMO system for N=3

As it is concluded by comparison of figures 6 and 7, as the number of the receivers increases, the BER of the system decreases due to the fact that all the receivers cooperate in order to enhance the received signal and also each receiver has the same γ with the other. In addition to this, in each figure it is obvious that the more hops and M the system has, the larger BER occurs.

On the other hand, the SS process is proved an effective way of signal transmission with lower BER. Forward Error Correction (FEC) employed as a Convolution coding is also productive in obtaining a lowered BER thus reducing the inherent disadvantage of a QAM system i.e. high SNR requirement for a small change in BER[19].

In order to enhance the system performance and avoid the appearance of errors during the transmission of the signal, various error coding techniques can be used such as [20]:

- TPC.
- Serially Concatenated Convolutional Code (SCCC).
- Standard Convolutional Code (SCC).

Comparison of these techniques proves that, the most effective technique is the SCCC because it enhances the Bit Error Probability (BEP) in many orders of magnitude for high values of SNR for frequency hop communication systems operating over an Additive White Gaussian Noise (AWGN) channel and the Log Likelihood Ratio (LLR) metric. For instance, for SNR=4dB the BEP for SCCC is approximately equal to 0.5, for TPC is equal to 10^{-1} and for SCC is equal to $8*10^{-2}$. However, for SNR≥5dB the SCCC has the best performance because its BEP=0, while the TPC has BEP=$8*10^{-5}$ and the SCC has BEP=10^{-2} (where it is equal to 0 for SNR=8.3dB).

6. Conclusion

In this project, a wireless RF communication system using UAS was described to mitigate the multipath effect that occurs while two or more ships are trying to communicate on an archipelagos environment. Implementing the UAS as relay nodes, it is achieved a better LOS coverage of a region overcoming the possible physical obstacles that may occur. Also, using the abovementioned multiplexing and modulation techniques, the QoS augmentation of the system is achieved. In future work, the whole proposed system will be tested in the region of the physical layer taking into consideration different values of fading and noise factors, such as the sea clutter and the precipitation.

References

1. Advances in Massive MIMO Antenna Design, Channel Modeling, and System Technologies

2. Zander &Malmgren, 1995.

3. Sethy, Niharika and Subhakanta Swain. “BER analysis of MIMO-OFDM system in different fading channel.” (2013).

4. M. K. Samimi, S. Sun and T. S. Rappaport, "MIMO channel modeling and capacity analysis for 5G millimeter-wave wireless systems," *2016 10th European Conference on Antennas and Propagation (EuCAP)*, Davos, 2016, pp.1-5.
doi: 10.1109/EuCAP.2016.7481507

5. J. Reig and L. Rubio, "Estimation of the Composite Fast Fading and Shadowing Distribution Using the Log-Moments in Wireless Communications," in *IEEE Transactions on Wireless Communications*, vol. 12, no. 8, pp. 3672-3681, August 2013. doi: 10.1109/TWC.2013.050713.120054

6. Yuan-Pei Lin and See-May Phoong, "BER minimized OFDM systems with channel independent precoders," in *IEEE Transactions on Signal Processing*, vol. 51, no. 9, pp. 2369-2380, Sept. 2003. doi: 10.1109/TSP.2003.815391

7. L. Rugini and P. Banelli, "BER of OFDM systems impaired by carrier frequency offset in multipath fading channels," in *IEEE Transactions on Wireless Communications*, vol. 4, no. 5, pp. 2279-2288, Sept. 2005.
doi: 10.1109/TWC.2005.853884

8. J. Akella, M. Yuksel and S. Kalyanaraman, "Error analysis of multi-hop free-space optical communication," *IEEE International Conference on Communications, 2005.ICC 2005.2005*, Seoul, 2005, pp.1777-1781 Vol. 3.
doi: 10.1109/ICC.2005.1494647

9. P. Podder, T. Zaman Khan, M. Haque Khan, M. Muktadir, "BER Performance Analysis of OFDM-BPSK, QPSK, QAM Over Rayleigh Fading Channel & AWGN Channel" International Journal of Industrial Electronics and Electrical Engineering, ISSN: 2347-6982, Volume-2, Issue-7, July-2014.

10. M. Meena, M. Singh, "Performance Analysis of BER with FHSS System", Volume II, Issue V, May 2013, IJLTEMAS, ISSN 2278 – 2540, pgs. 29-35.

11. E. Morgado, I. Mora-Jiménez, J.J. Vinagre, J. Ramos, A. J. Caamano, "End-to-End Average BER in Multihop Wireless Networks over Fading Channels", IEEE TRANSACTIONS ON WIRELESS COMMUNICATIONS, VOL. 9, NO. 8, AUGUST 2010, pgs. 2478-2487.

12. N. Jindal, J. G. Andrews and S. Weber, "Multi-Antenna Communication in Ad Hoc Networks: Achieving MIMO Gains with SIMO Transmission," in *IEEE Transactions on Communications*, vol. 59, no. 2, pp. 529-540, February 2011.
doi: 10.1109/TCOMM.2010.120710.090793

13. G.K. Varotsos, H.E. Nistazakis, M.I. Petkovic, G.T. Djordjevic, G.S. Tombras, "SIMO optical wireless links with nonzero boresight pointing errors over M modeled turbulence channels", Optics Communications, Volume 403, 2017, Pages 391-400, ISSN 0030-4018, https://doi.org/10.1016/j.optcom.2017.07.055.

14. A Flexible Phased-MIMO Array Antenna with Transmit Beamforming

15. Beamforming Techniques for Wireless MIMO Relay Networks

16. H.E. Nistazakis, A.N. Stassinakis, S. Sheikh Muhammad, G.S. Tombras, "BER estimation for multi-hop RoFSO QAM or PSK OFDM communication systems over gamma gamma or exponentially modeled turbulence channels", Optics & Laser Technology, Volume 64, 2014, Pages 106-112, ISSN 0030-3992, https://doi.org/10.1016/j.optlastec.2014.05.004.

17. K.N. Manganaris, N.A. Androutsos, A.N. Stassinakis, A.D. Tsigopoulos, A. Tzanakaki, H.E. Nistazakis, "Outage performance study of a multi-hop AF relay system approximated by a dual-hop scheme over Rician fading wireless channels", pgs. 281-286, 8th International Conference on "Experiments/Process/System Modeling/Simulation/Optimization" 8th IC-EPSMSO,Athens 3-6 July 2019, ©LFME.

18. Yuan, Y., Chen, M. & Kwon, T, "A Novel Cluster-Based Cooperative MIMO Scheme for Multi-Hop Wireless Sensor Networks", *J. Wireless Com Network* **2006,** 072493 (2006). https://doi.org/10.1155/WCN/2006/72493.

19. B. Sklar "Rayleigh Fading Channels" Mobile Communications Handbook Ed. Suthan S. Suthersan Boca Raton: CRC Press LLC, 1999.

20. H. S. Kim and B. Daneshrad, "Energy-Constrained Link Adaptation for MIMO OFDM Wireless Communication Systems," in *IEEE Transactions on Wireless Communications*, vol. 9, no. 9, pp. 2820-2832, September 2010.
doi: 10.1109/TWC.2010.062910.090983.

21. H. E. Nistazakis, A. N. Stassinakis, H. G. Sandalidis and G. S. Tombras, "QAM and PSK OFDM RoFSO Over M-Turbulence Induced Fading Channels," in *IEEE Photonics Journal*, vol. 7, no. 1, pp. 1-11, Feb. 2015, Art no. 7900411.
doi: 10.1109/JPHOT.2014.2381670

22. B. Ahmed, M. Abdul Matin, "Coding for MIMO-OFDM in Future Wireless Systems", Springer Cham Heidelberg New York Dordrecht London, ISSN 2191-8120 (electronic) Springer Briefs in Electrical and Computer Engineering, ISBN 978-3-319-19153-9 (eBook) DOI 10.1007/978-3-319-19153-9 © The Author(s) 2015.

23. M. Strasser, C. Popper, S. Capkun and M. Cagalj, "Jamming-resistant Key Establishment using Uncoordinated Frequency Hopping," *2008 IEEE Symposium on Security and Privacy (sp 2008)*, Oakland, CA, 2008, pp. 64-78.
doi: 10.1109/SP.2008.9

24. C. Chen and P. P. Vaidyanathan, "MIMO Radar Ambiguity Properties and Optimization Using Frequency-Hopping Waveforms," in *IEEE Transactions on Signal Processing*, vol. 56, no. 12, pp. 5926-5936, Dec. 2008.
doi: 10.1109/TSP.2008.929658.

25. N. Hossein Motlagh, "Frequency Hopping Spread Spectrum: An Effective Way to Improve Wireless Communication Performance" pgs. 187-202, Advanced Trends in Wireless Communications.

26. W.G. Phoe, J.A. Pursley, M.B. Pursley, J.S. Skinner, "FREQUENCY-HOP SPREAD SPECTRUM WITH QUADRATURE AMPLITUDE MODULATION AND ERROR-CONTROL CODING", MILCOM 2004 - 2004 IEEE Military Communications Conference, pgs. 913-919.

27. A.N. Stassinakis, H.E. Nistazakis, G.S. Tombras "Comparative performance study of one or multiple receivers schemes for FSO links over gamma–gamma turbulence channels", Journal of Modern Optics Vol. 59, No. 11, 20 June 2012, pgs. 1023–1031.

Multistatic Radar Low Probability of Intercept signaling for the enhancement of target detectability in an adverse electromagnetic environment

Th. Papastamatis[a], K. Ioannou[b], I. Koukos[c] and T. Xenos[e]

[a] *Hellenic Air Force, Lieutenant, Ph.D. Candidate, Aristotle University of Thessaloniki, Greece*
[b] *Hellenic Navy, Lieutenant Junior Grade, PhD Candidate, Aristotle University of Thessaloniki, Greece*
[c] *Combat Systems Sector, Hellenic Naval Academy, Piraeus, Greece*
[d] *Aristotle University of Thessaloniki, Greece*

Abstract. Low Probability of Intercept (LPI) waveforms have been used so far in monostatic radar signaling for pulse compression that results in drastic improvement of radar resolution or granularity. Multistatic radar becomes increasingly important due to its alleged ability to detect stealth aircraft. However opportunistic exploitation of TV, FM radio or GSM Cellular emissions will not safeguard acceptable probability of detection levels, therefore the design of special signals emitted from dedicated beacons is a way to bring out all stealth's design weaknesses. This paper analyzes LPI waveforms via their Autocorrelation, their Periodic Ambiguity and Periodic Autocorrelation Functions for the bistatic radar which will open the way to discover new optimum target detection geometries and denoising strategies.

Keywords. -Low Probability of Intercept, Ambiguity Functions, Autocorrelation Functions, Bistatic Radar

1. INTRODUCTION

Airwaves are awash with commercial radiowave broadcasts emitted by WiFi, WiMax transmissions, DVB TV, FM radio or GSM *cellular phone* stations. Military researchers have thought long ago of using them as sources of RF radiation as a substitute of radar transmitters. This freely available radiation reflected from flying objects of any kind, will form a multistatic opportunistic passive radar that will detect a target by generating position and kinematic tracks equivalent to those of a regular monostatic radar. Furthermore, stealthy targets will be detected with much higher probability because a multistatic radar receiver can catch scattered reflections from a stealth aircraft which is structurally optimized only to minimize reflected signal from the direction of the illuminating source and cannot prevent scattering of radiation to other directions.

A radar detector classically searches the trace of a target in the output of a matched filter. Classically, the performance of a radar waveform is evaluated and presented in terms of the ambiguity function, originated in the 1950s by F. Gini et. al. [1], and which expresses the point

ISSN:1791-4469

target response of the signal u(t) as a function of delay τ and Doppler shift ν (or equivalently target range and velocity),

$$\left|\chi(\tau,\nu)\right|^2 = \left|\int u(x)u^*(x+\tau)\exp(j2\pi\nu x)dx\right|^2 \quad (1)$$

in the form of two dimensional plot.

2. THE BISTATIC RADAR EQUATION

The range equation for a monostatic radar is given by [2] :

$$R = \left[\frac{P_T G_T G_R \lambda^2 \sigma F^4}{(4\pi)^3 k T_s B_n (S/N)_{\min} L}\right]^{1/4} \quad (2)$$

where R is the range from the radar to the target, P_T is the transmitter power output, G_T is the transmitting antenna gain, G_R is receiving antenna gain, λ is the carrier wavelength, σ is target cross section, F is the atmospheric attenuation factor, k is Boltzmann's constant, T_S is receiving system noise temperature, and B_n is the receiver's noise bandwidth, $(S/N)_{min}$ is the minimum SNR required for detection, and L accounts for various losses. The coverage area resembles a circle around the radar. This causes the SNR to be constant at a given range [2]:

$$(S/N) = \left[\frac{P_T G_T G_R \lambda^2 \sigma F^4}{(4\pi)^3 k T_s B_n L R^4}\right] \quad (3)$$

The lines of constant SNR around the node are called SNR contours stemming from the geometric Cassini curve. The circular shape of the SNR contours means that the area is calculate by [6]:

$$A = \pi R^2$$

where R is the distance from the node to a given Cassini curve.

For the bistatic radar, the maximum range equation is given by [2] :

$$(R_T R_R)_{\max} = \left[\frac{P_T G_T G_R \lambda^2 \sigma F_T^{\,2} F_R^{\,2}}{(4\pi)^3 k T_s B_n (S/N)_{\min} L}\right]^{1/2} = \kappa \quad (4)$$

where R_T is transmitter to target range, R_R is receiver to target range, F_T is the atmospheric attenuation factor from the transmitter to the target, F_R is the atmospheric attenuation factor from the target to the receiver, and κ is the bistatic maximum range product.

Each Cassini oval represents a constant SNR level. R_T and R_R change as their intersection on a given SNR contour moves. The target position is considered to be this point of intersection. From the above equation, the SNR of the bistatic radar is given by [2] :

$$(S/N)=\left[\frac{P_T G_T G_R \lambda^2 \sigma F_T{}^2 F_R{}^2}{(4\pi)^3 k T_s B_n L R_T{}^2 R_R{}^2}\right] \tag{5}$$

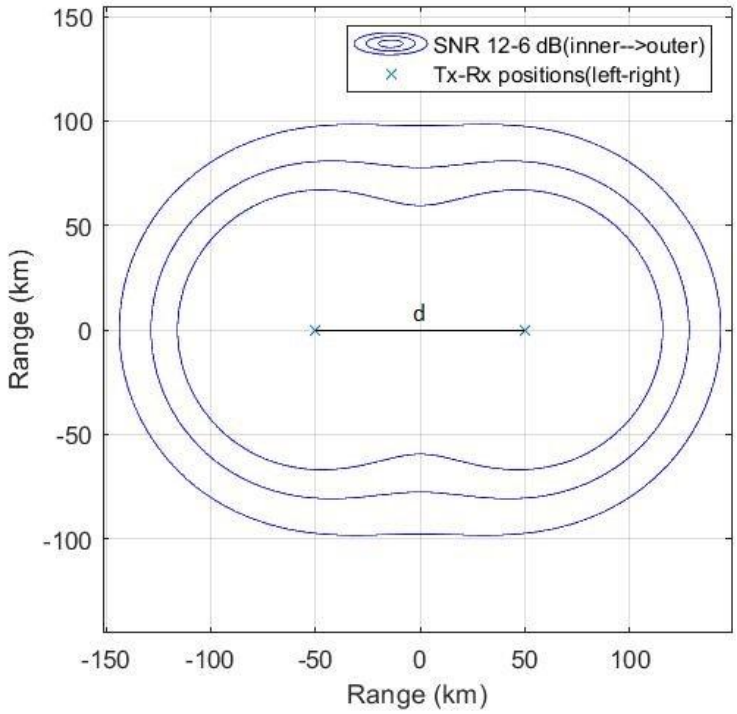

Figure 1. Bistatic radar Cassini ovals

From [2] we can also derive the area within the ovals of Cassini for a bistatic system, which can be used to compare different bistatic systems. This area is given as [2]:

$$A_B \approx \pi\kappa\left[1-\left(\frac{1}{2}\right)^2\left(\frac{d^4}{16\kappa^2}\right)\left(\frac{1}{1}\right)-\left(\frac{1*3}{2*4}\right)^2\left(\frac{d^4}{16\kappa^2}\right)^2\left(\frac{1}{3}\right)-\ldots\right]\approx\pi\kappa\left[1-\left(\frac{d^4}{64\kappa^2}\right)-\left(\frac{3d^8}{16384\kappa^4}\right)\right] \tag{6}$$

ISSN:1791-4469

3. NETTED RADAR

The netted radar system is a network of identical systems at each node, using the synchronization across transmitters and receivers. The target is an isotropic scatterer and a noise limited system performance has been achieved. Such a distributed radar system allows the potential SNR gains to approach n^2 where n is the number of sensor nodes. Synchronization is the key requirement in order to realize this potential.

The general radar range equation is modified to yield the range equation for the distributed radar [2]:

$$(S/N) = \sum_{i=1}^{n}\sum_{j=1}^{n}\left[\frac{P_T G_T G_R \lambda^2 \sigma F_T{}^2 F_R{}^2}{(4\pi)^3 k T_s B_n L R_{Ti}{}^2 R_{Rj}{}^2}\right] = \sum_{i=1}^{n}\sum_{j=1}^{n}(S/N)_{ij} \quad (7)$$

where R_{Ti} is range from transmitter i to the target, R_{Rj} is range from receiver j to the target, and $(S/N)_{ij}$ is the SNR when node i is the transmitter and j is the receiver. The indices of summation are due to the collective nature of the system as every node transmits a pulse and all radars receive returns due to every transmitted pulse. Each of these actions contributes to the overall system's SNR, resulting in the potential n^2 gains. Table 1 illustrates the affect the indices of summation have on the total SNR for a distributed radar network with $n = 3$. The rows represent the summation over i and the columns represent the summation over j.

	j=1	j=2	j=3
i=1	Tx_1/Rx_1	Tx_1/Rx_2	Tx_1/Rx_3
i=2	Tx_2/Rx_1	Tx_2/Rx_2	Tx_2/Rx_3
i=3	Tx_3/Rx_1	Tx_3/Rx_2	Tx_3/Rx_3

Table 1. Distributed radar network

In order to evaluate the performance of radar systems with different numbers of nodes, a means to plot these systems must be developed. This section expands the work done in [4] in order to develop a means to compare a monostatic radar system to a distributed radar system.

i. GENERAL EXPRESSION FOR R

The Cassini curve is a curve for which the product of multiple polar radii is constant. This is a generalization of the definition of Cassini oval (n = 2) provided in [2], as described above. This definition is expressed as [2]:

$$\prod_{i=1}^{n} R_i = a \quad (8)$$

where n is the number of nodes R_i is the distance from the ith node to a Cassini curve and α is a constant. The general equation for R, which is the distance from the origin point on a Cassini curve (given in polar form), is [2]:

$$R^n = 2\cos n\theta + \frac{\alpha - 1}{R^n} \tag{9}$$

where θ is the angle used in the polar plot ($0 \le \theta \le 2\pi$). Manipulating terms in the above equation yields the range from the origin to a point on a Cassini curve [2]:

$$R = r\sqrt[n]{\cos n\theta \pm \sqrt{\alpha - \sin^2 n\theta}} \tag{10}$$

where r is the radius from the origin to each node (and therefore dictates the size of the curves).

The geometry of the sensor network affects the variable r which is different for each formation. In order to simplify the results for these shapes and provide a more general expression for R than Equation (10), the following values for r are established for n=2, n=3(equilateral triangle), n=4 (square) [2]:

$$\begin{aligned} r &= \frac{d}{2}, n = 2 \\ r &= \frac{d}{\sqrt{3}}, n = 3 \\ r &= \frac{d}{\sqrt{2}}, n = 4 \end{aligned} \tag{11}$$

ii. TWO NODES

For the system consisting of n=2 nodes and the use of the Pythagorean theorem, the ranges R_R,R_T can be expressed as [2]:

$$R_R^2 = (R^2 + d^2/4) - Rd\cos\theta \tag{12}$$

$$R_T^2 = (R^2 + d^2/4) + Rd\cos\theta \tag{13}$$

The product of the above ranges is [2]:

$$R_T R_R = \kappa = \sqrt{R^4 + \frac{R^2 d^2}{2} + \frac{d^4}{16} - R^2 d^2 \cos^2\theta} \tag{14}$$

For $\kappa = 0$ the above equation transforms to [2]:

ISSN:1791-4469

$$R^2 = \left(\frac{d}{2}\right)^2 \left[\cos 2\theta + \sqrt{\cos^2(2\theta) + \left(\frac{2\sqrt{\kappa}}{d}\right)^4 - 1}\right] \tag{15}$$

For n = 2, we also have [2,4]:

$$r = d/2$$

$$a = \left(\frac{2\sqrt{\kappa}}{d}\right)^4 = \left(\frac{\sqrt{\kappa}}{r}\right)^4 \tag{16}$$

where d is the separation of the sensor nodes.

There are three cases for the Cassini ovals where:

- For $d > 2\sqrt{k}$ we get two ovals centered on each node
- For $d < 2\sqrt{k}$ we get a closed curve
- For $d = 2\sqrt{k}$ the curve is sinusoidal spiral or lemniscates

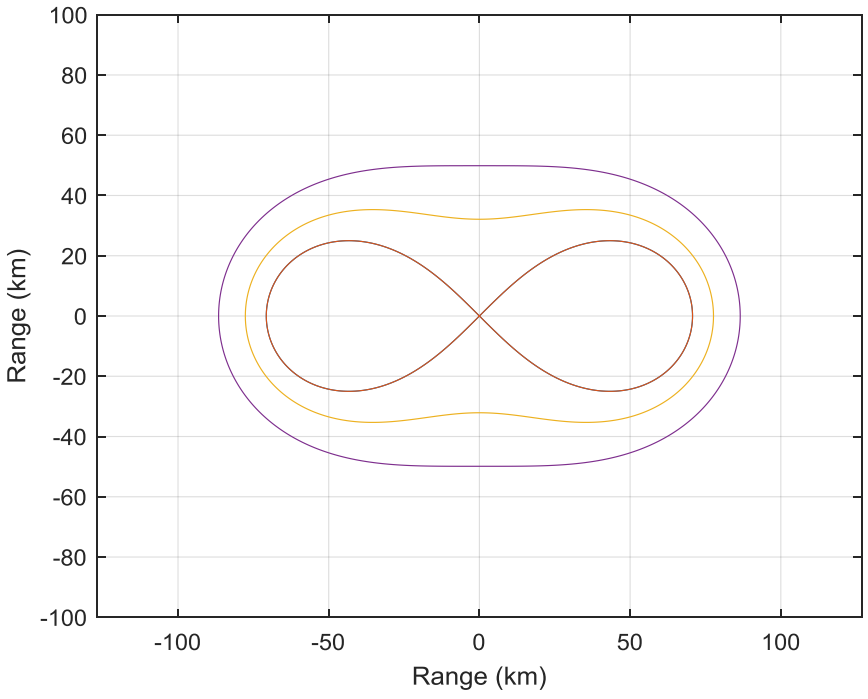

Figure 2. Cassini Ovals for n = 2 nodes

iii. THREE NODES

For n = 3 nodes configuration we use the same technique as we used for the n=2 nodes configuration with [2]:

$$r = d/\sqrt{3}$$
$$a = \left(\frac{\sqrt{\kappa}}{r}\right)^4 = \left(\frac{\sqrt{3}\sqrt{\kappa}}{d}\right)^4 = \frac{9\kappa^2}{d^4} \quad (17)$$

and the three cases for Cassini curves become:

- For $d > \sqrt{3k}$ we get three ovals centered on each node
- For $d < \sqrt{3k}$ we get a closed curve
- For $d = \sqrt{3k}$ the curve is sinusoidal spiral or lemniscate

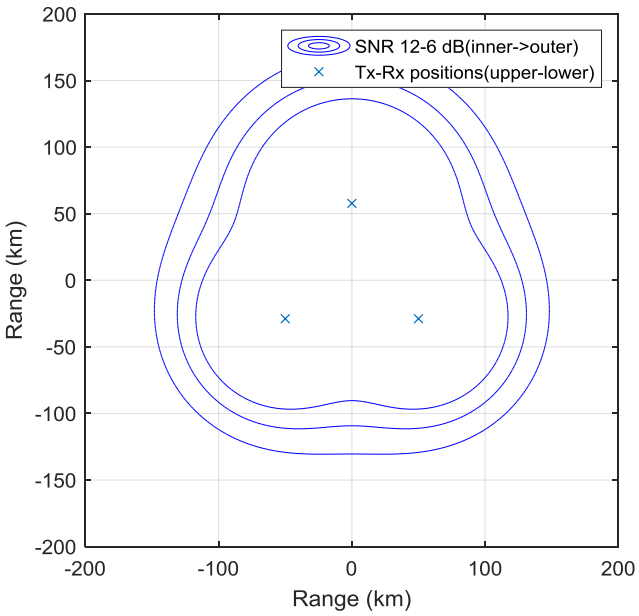

Figure 3. Cassini Ovals for n=3 nodes

We observe that the coverage is not symmetrical due to the odd number of nodes. Below we compare the monostatic and a 3-node netted radar network. The extra coverage, due to this configuration, is more than obvious, covering a 360 degrees sector and extending the range even 100 kilometers longer than the monostatic case.

ISSN:1791-4469

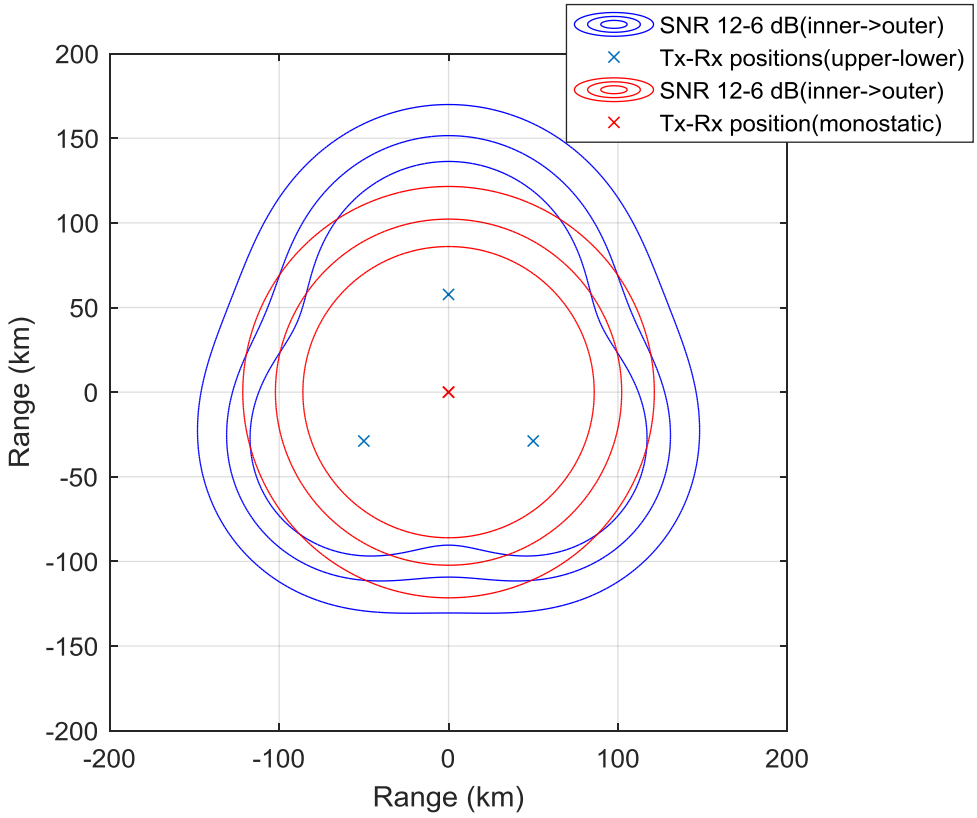

Figure 4. Comparison of coverage between n = 1 and n = 3 nodes Cassini Ovals

4. LPI RADARS

Radars, in general, transmit pulses with small pulsewidth. This has nothing in common with the LPI radars, where longer duration pulses are emitted in order to deceive the target's systems and believed to be a CW radar emission. This property is expressed by the parameter known as the Duty Cycle of the radar and which expresses the ratio of average power to the maximum radiated power of the radar.

$$dc = Pavg / Pmax \tag{18}$$

LPI radars use waveforms that don't differ from the classical pulse compression waveforms used in conventional pulse doppler radars. The main difference though, is that the signal carrier is a continuous wave. The pulse compression techniques instead, are the same and use frequency coding (frequency shift, FSK) or phase coding (phase shifting, PSK) or combined frequence and phase coding (FSK / PSK waveforms). The extraction of the pulse characteristics from the receiver depend on the complexity of the waveform.

5. AMBIGUITY FUNCTION, PERIODIC AMBIGUITY FUNCTION AND PERIODIC AUTOCORRELATION FUNCTION IN LPI SIGNALS [4]

If we consider a phase-modulated CW signal, where N_c is the number of phase states (codes), while t_b is the duration of each different state (subcode), the period of the signal is given by the relation:

$$T = N_C t_b \tag{19}$$

Then the complex periodic signal is mathematically described by the relationship:

$$u(t) = u(t+nT) = u(t+N_c t_b) \tag{20}$$

where: $n = 0, \pm 1, \pm 2, \pm 3, \ldots$

The Autocorrelation Function (ACF) of the signal expresses the response of the tuned filter of the receiver to the input signal. In particular, the response of the filter equals the complex conjugate of the emitted signal. Thus, the input signal passing through the tuned filter, in practice, correlates with its image from which the delay is calculated. The Periodic Autocorrelation Function (PACF) is used on the CW radar and essentially gives exactly what the ACF, the response of the tuned filter to the input signal. The PACF form, however, is different from that of ACF, since the transmitted signal - like the one received - on an LPI radar is a periodic waveform, which contains the NN copy number of the encoded signal. Consequently, the PACF study is more appropriate in the case of LPI radar. The PACF is given by the following relationship:

$$\mathrm{R}(\tau\, \mathrm{t}_b) = \frac{1}{N_c} \sum_{n=1}^{N_c} u(n)\, \mathrm{u}^*(n+\tau) \tag{21}$$

Where: τ is the time delay while the operator (*) denotes the complex conjugate. Given that the signal is continuous and periodic, it follows from the above equation that the PACF is maximal when the delay takes values that are multiples of the code period t_b, ie:

$$\mathrm{R}(\tau\, \mathrm{t}_b) = \begin{cases} 1, \tau = 0(\mathrm{mod}\mathrm{N}_c) \\ 0, \tau \neq 0(\mathrm{mod}\mathrm{N}_c) \end{cases} \tag{22}$$

Equation (22) practically means that CW waveforms, formed by a periodic function, can theoretically have the ideal PACF, i.e. zero side lobes. The autocorrelation function is sufficient to describe whether the received radar signal is shifted in time relative to its emitted analog, but it does not give any information about the change in its doppler frequency. As known, when the signal returning to the receiver is derived from a moving target, it has a frequency shift due to

ISSN:1791-4469

doppler the size of which needs to be known so that the frequency response of the tuned receiver is suitably matched to the frequency of the received signal, so it finally operates the tuned filter correctly.

Thus, the Periodic Ambiguity Function (PAF) is defined as the function describing the result of the correlation of N periodic copies of the emitted signal to the received CW signal for target detection. In fact, PAF expresses the response of the matched radar receiver to the input signal and includes any change in the doppler frequency and also in the delay. PAF is the analog of the Ambiguity Function (AF) used in pulse radars. The only difference is that PAF refers to a continuous wave radar where the transmitted CW signal is formed by a periodic function with period T, whereby the reference signal for the tuned receiver is a signal consisting of N periods. So if $u(t)$ is the reference signal generated by N number of periods, then PAF for the tuned receiver is given by:

$$\left|\chi_{\mathrm{NT}}(\tau,\nu)\right| = \left|\frac{1}{\mathrm{NT}}\int_{0}^{\mathrm{NT}} u(t-t)u^{*}(t)e^{j2\pi\nu t}dt\right| \tag{23}$$

where the delay τ is considered constant, while ν is the doppler displacement. It can also be shown that the following relationship applies:

$$\left|\chi_{\mathrm{NT}}(\tau,\nu)\right| = \left|\chi(\tau,\nu)\right|\left|\frac{\sin(N\pi\nu\mathrm{T})}{\mathrm{N}\sin(\pi\nu\mathrm{T})}\right| \tag{24}$$

where: $|\chi(\tau, \nu)|$ is the PAF for a period of the signal. Consequently, PAF of N signal periods can be calculated by multiplying the PAF of a period as in equation (23). It should be noted that the corresponding PACF of N periods of a signal result from the PACF of a period multiplied simply by N.

Similarly to AF, PAF has a maximum equal to 1 when $\nu = \tau = 0$ (beginning of axes) in the sense that the response of the custom filter is always the maximum when the associated signal is the copy of itself when is not delayed in time or altered in frequency. So by studying PAF, we can see changes in the frequency or time of the received signal. PAF also shows symmetry wrt both axes (ν, τ). In terms of time, the symmetry of PAF is expressed by the relationship:

$$\left|\chi_{\mathrm{NT}}(\mathrm{nT},\nu)\right| = \left|\chi_{\mathrm{NT}}(0,\nu)\right| \tag{25}$$

where: n is any integer. Similarly, in terms of Doppler frequency, symmetry is expressed as:

$$\left|\chi_{\mathrm{NT}}(\tau,\mathrm{m}/\mathrm{T})\right| = \left|\chi_{\mathrm{NT}}(\tau+\nu T,\mathrm{m}/\mathrm{T})\right| \tag{26}$$

where: m / T are intersections along the doppler axis ($\nu = m / T$) and $m = 0, \pm 1, \pm 2, ...$

It is easy to see that for v = 0, which is equivalent to the intersection of the time axis, the PAF graph is the same as the PACF.

i. Pulse

To begin with we will start observing the Ambiguity Function (AF) and Periodic Ambiguity Function (PAF) of a constant frequency pulse (unmodulated) in order to start as simple as possible.

The Ambiguity Function of this pulse is illustrated below [5]:

$$\chi(\tau,\nu)=\int_{-\infty}^{\infty}u(\mathrm{t})\,\mathrm{u}^{*}(\mathrm{t}+\tau)\exp(\mathrm{j}2\pi\nu\,\mathrm{t})\,\mathrm{dt} \tag{27}$$

In Figure 5, in which the two quadrants of the pulse are plotted, the triangular zero Doppler cut is shown clearly. The pulse's parameters, autocorrelation and spectrum plots are also shown below along with the Periodic Ambiguity plot.

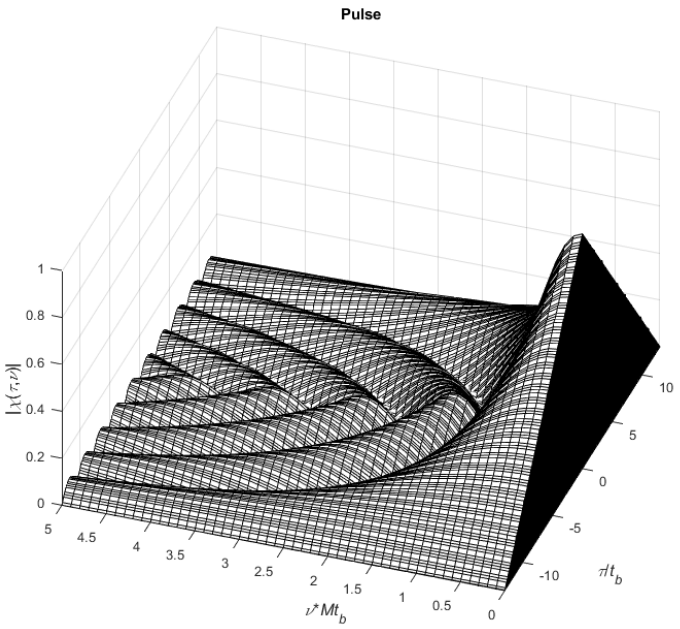

Figure 5. Ambiguity function plot of a constant frequency pulse

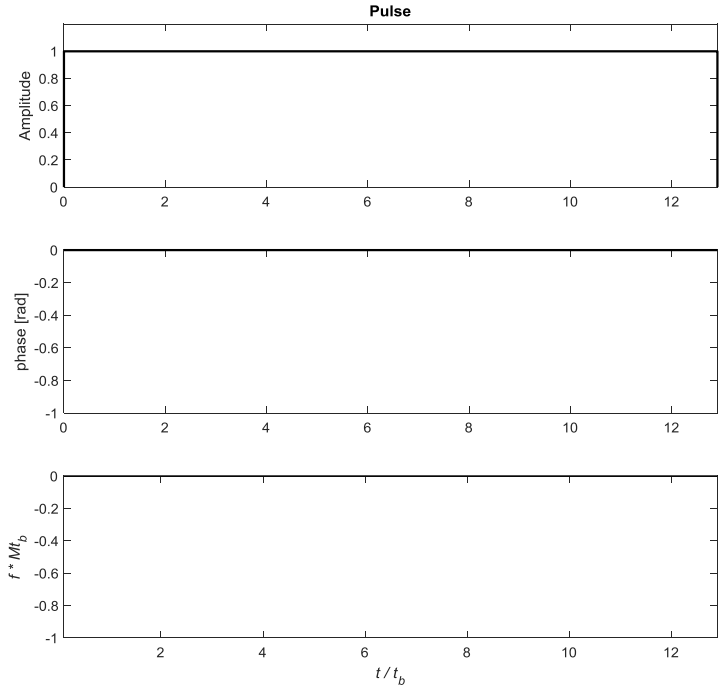

Figure 6. Signal parameters plot of a constant frequency pulse

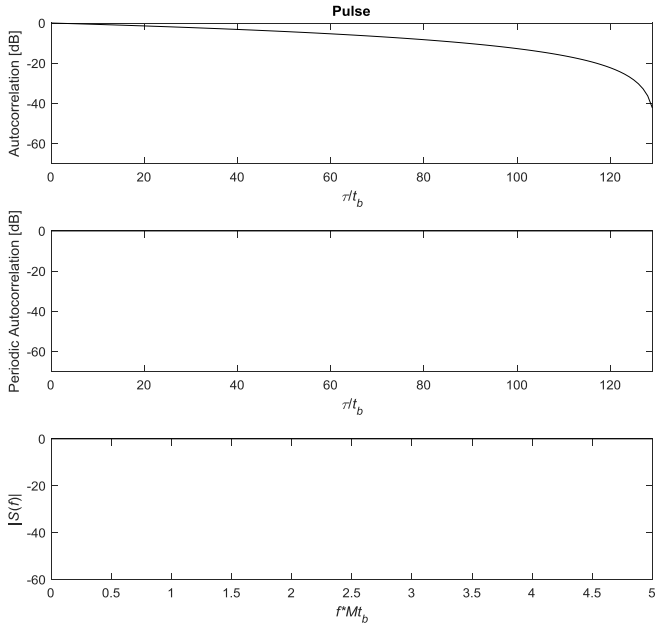

Figure 7. Autocorrelation and Spectrum plots of a constant frequency pulse

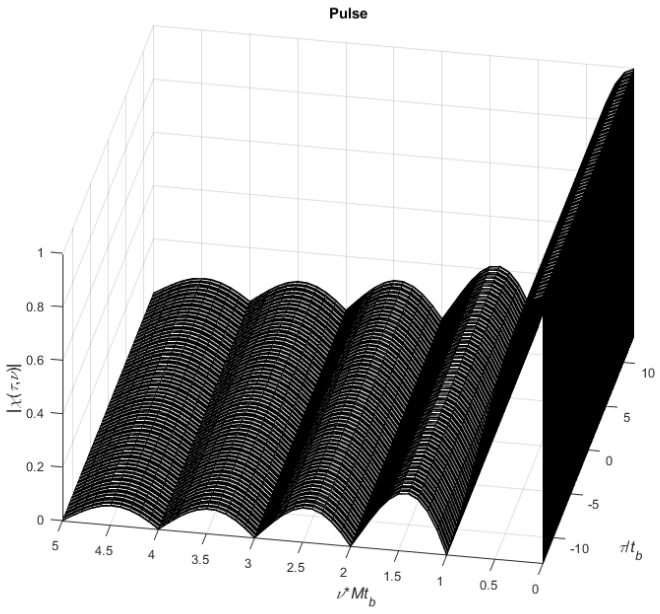

Figure 8. Periodic Ambiguity function plot of a constant frequency pulse

If more than one unmodulated pulses are transmitted, we are talking about a coherent pulse train (CPT). In our Ambiguity Function, signal characteristics, autocorrelation and Spectrum and Periodic Ambiguity Function plots we use six identical pulses. The production of more complicated signals though, needs some diversity.

ii. Coherent Pulse Train

For a coherent pulse train the Ambiguity Function is [5] :

$$|\chi(\tau,\nu)| = \frac{1}{N}\sum_{p=-(N-1)}^{N-1} |\chi_T(\tau - pT_r,\nu)| \left|\frac{\sin[\pi\nu(N-|p|)T_r]}{\sin \pi\nu T_r}\right|, \quad \begin{matrix} |\tau| \le NT_r \\ |\tau| \le T \end{matrix}, \text{ zero elsewhere} \qquad (28)$$

where $|\chi_T(\tau,\nu)|$ is Ambiguity Function of an individual pulse. For the illustrated unmodulated pulse below, we use the equation [5] :

$$|\chi_T(\tau,\nu)| = \left|\left(1-\frac{|\tau|}{T}\right)\frac{\sin\left[\pi T\nu(1-|\tau|/T)\right]}{\pi T\nu(1-|\tau|/T)}\right|, \quad |\tau| \le T \text{ , zero elsewhere} \qquad (29)$$

ISSN:1791-4469

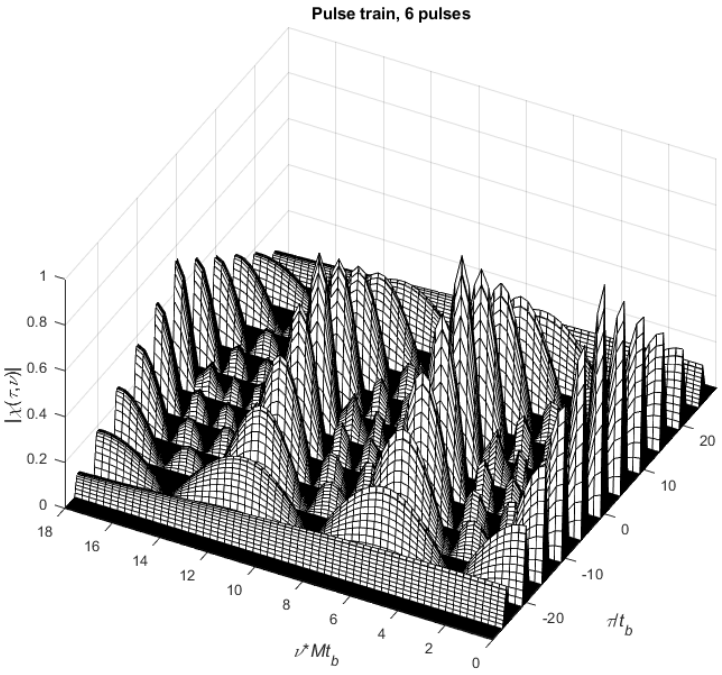

Figure 9. Ambiguity function plot of a 6 pulses Pulse train

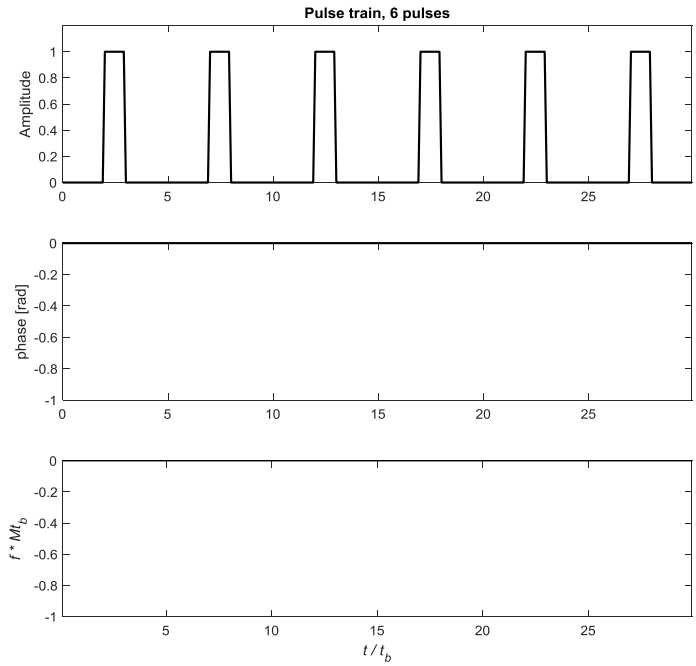

Figure 10. Signal parameters plot of a 6 pulses Pulse train

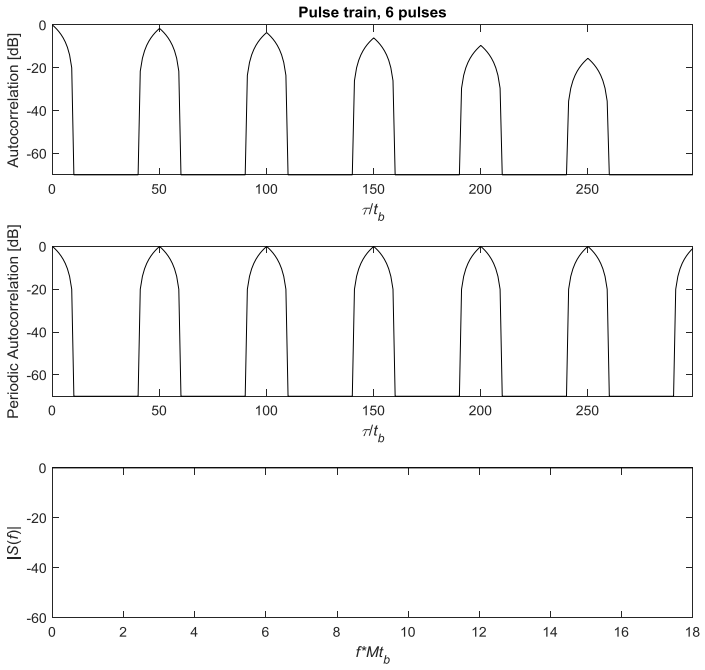

Figure 11. Autocorrelation and Spectrum plots of a 6 pulses Pulse train

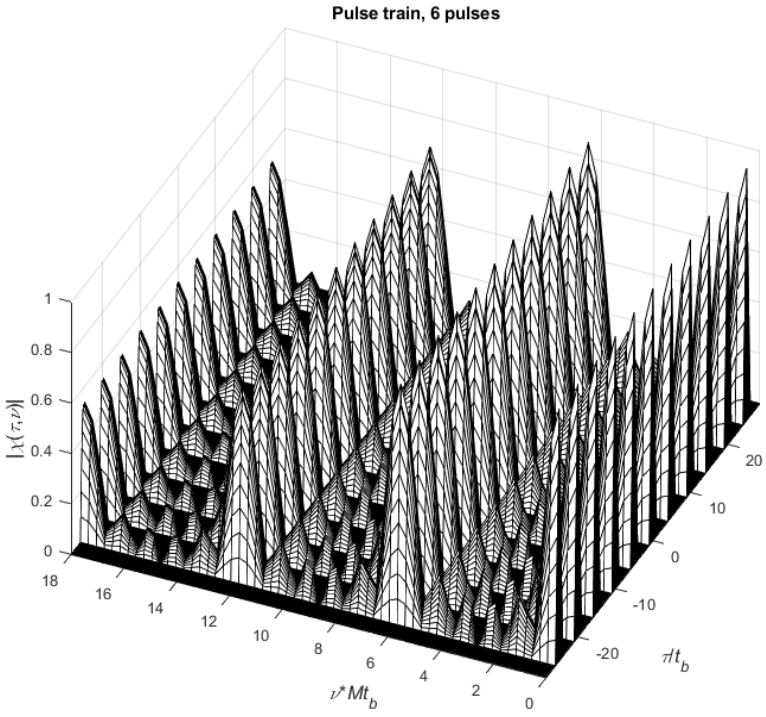

Figure 12. Periodic Ambiguity function plot of a 6 pulses Pulse train

ISSN:1791-4469

iii. Linear Frequency Modulated (LFM) and Weighted Linear Frequency Modulated (LFM) CW signal

If pulse compression method has to be introduced in order to have more efficient along with complicated pulses, then we should start with the frequency modulation method. The well-known Linear Frequency Modulation (LFM) is the one that will be discussed first.
Its Ambiguity Function is [5]:

$$|\chi(\tau,\nu)| = \left|(1-\frac{|\tau|}{T})\frac{\sin(\pi T(\nu \mp B(\tau/T))(1-|\tau|/T))}{\pi T(\nu \mp B(\tau/T))(1-|\tau|/T)}\right|,\ |\tau| \le T \text{, zero elsewhere} \quad (30)$$

Figure 14 illustrates the phase and frequency variation of a Linear Frequency Modulated (LFM) CW signals. Figure 16 shows the PAF of the signal while in Figure 15 is shown its corresponding ACF and PACF. M is the number of signal samples, while t_b is the sampling time, so obviously the total duration of the signal is Mt_b. One of the desired characteristics of the PAF of an LPI waveform is that the level of the side lobes must be as minimal as possible. This is because when the return of a target from the radar sidelobes is strong, there is the possibility that a smaller RCS target will not be detected because its return is lost in the sidelobes of the previous target.

The FMCW radar originally was designed to address the weakness of CW radar (unmodulated signal) to calculate the distance of a target. Afterwards, it turned out that FMCW waveforms have very good LPI features and also have several interesting advantages. FMCW waveforms have increased interference resistance in the sense that they are deterministic signals, and consequently any interfering signal lacking the same mathematical pattern can be recognized by the radar receiver and discarded, [2]. Yet another advantage is that the energy of the emitted signal diffuses over a wide modulation bandwidth, resulting in the signal eventually being very low in power and therefore difficult to detect. This is particularly desirable in cases where a low level of emissions from a platform is required. Figure 15 shows the ACF and PACF of the signal. As shown, the level of the side lobes in the ACF is relatively low, but the signal does not have the ideal PACF since there are sidelobes over time in the PACF plot. Figure 16 also shows the PAF of the signal, where the side lobes are plotted in terms of the doppler frequency, meaning that the signal does not behave well in the presence of doppler shifts.

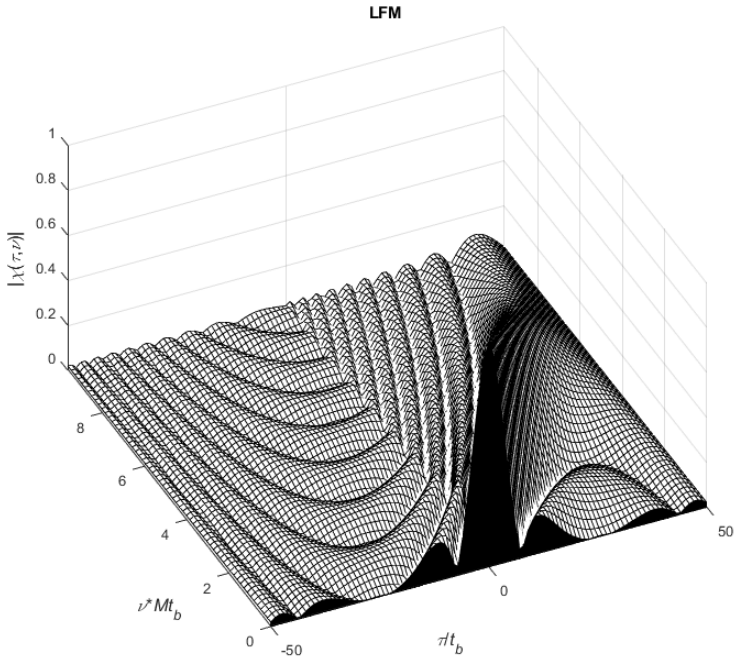

Figure 13. Ambiguity Function plot of a Linear Frequency Modulated (LFM) CW signal

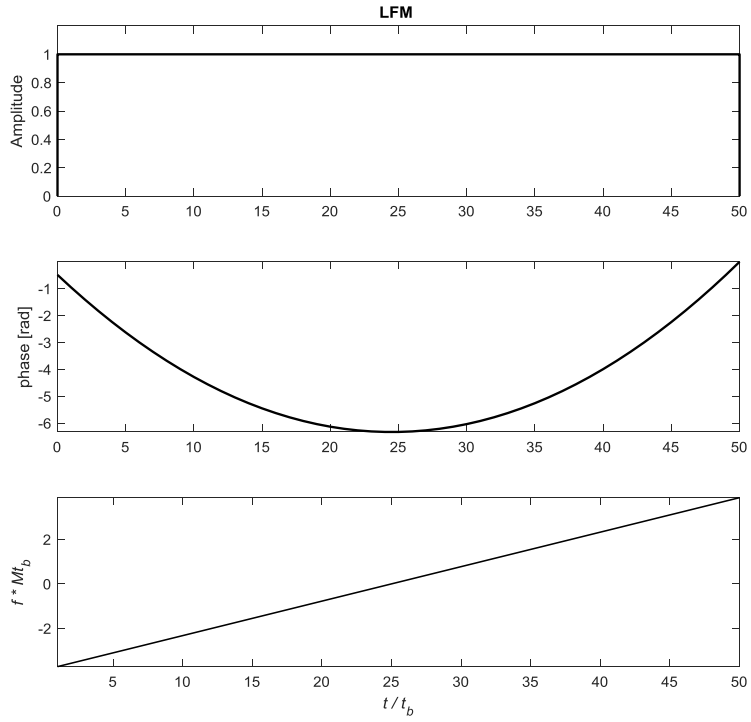

Figure14. Signal parameters plot of a Linear Frequency Modulated (LFM) CW signal

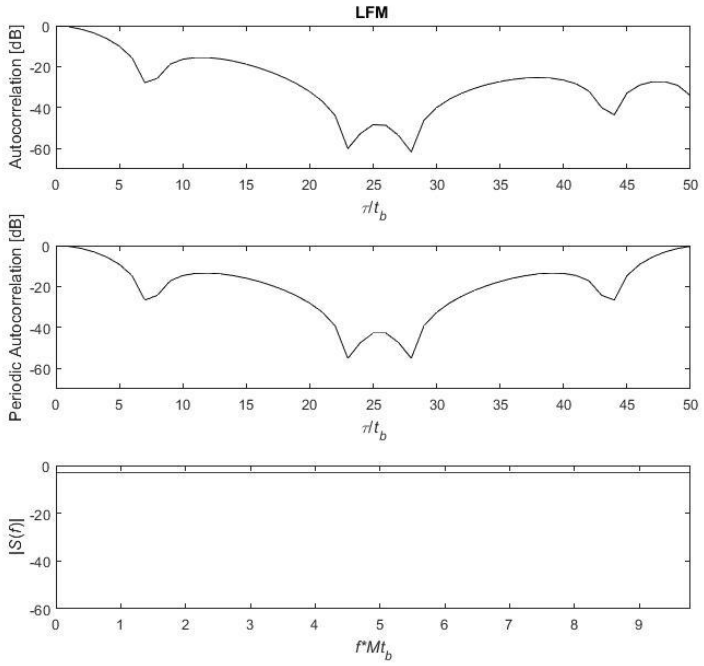

Figure 15. Autocorrelation and Spectrum plot of a Linear Frequency Modulated (LFM) CW signal

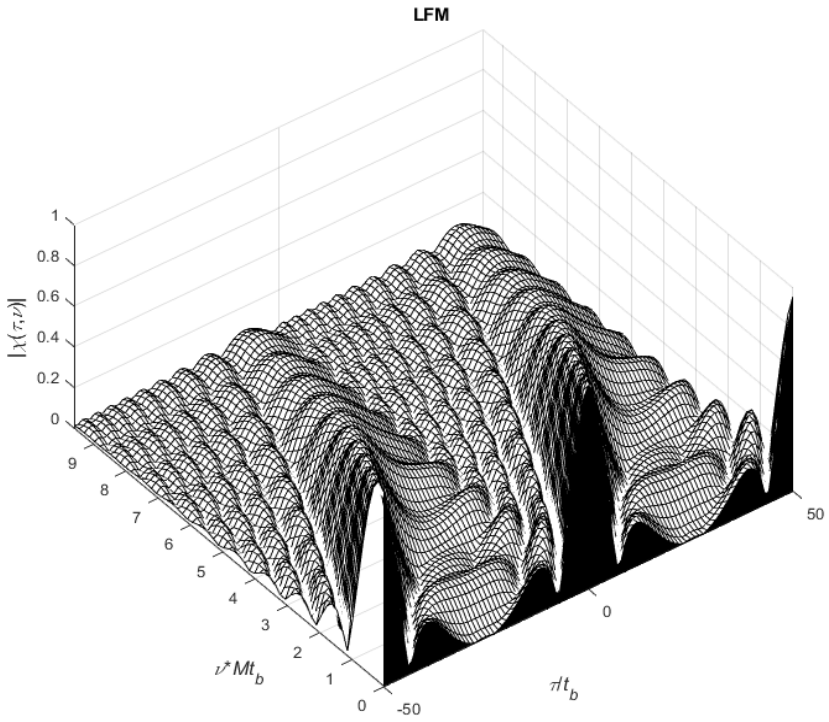

Figure 16. Periodic Ambiguity function of a Linear Frequency Modulated (LFM) CW signal

LFM has the positive outcome of improved range resolution, resulting from the increase of the bandwidth. The negative outcome of the LFM signal is the sidelobes' amplitude, that can be observed in Figure 13. In order to mitigate this phenomenon, spectral reshaping with amplitude or frequency weighting was introduced. In this simulation, the Hamming weighted LFM pulse was used.

Comparing Figure 13 with Figure 17 it is obvious that the sidelobes of the central lobe are reduced. It has also been observed the weighting has effects even at higher Doppler frequencies.

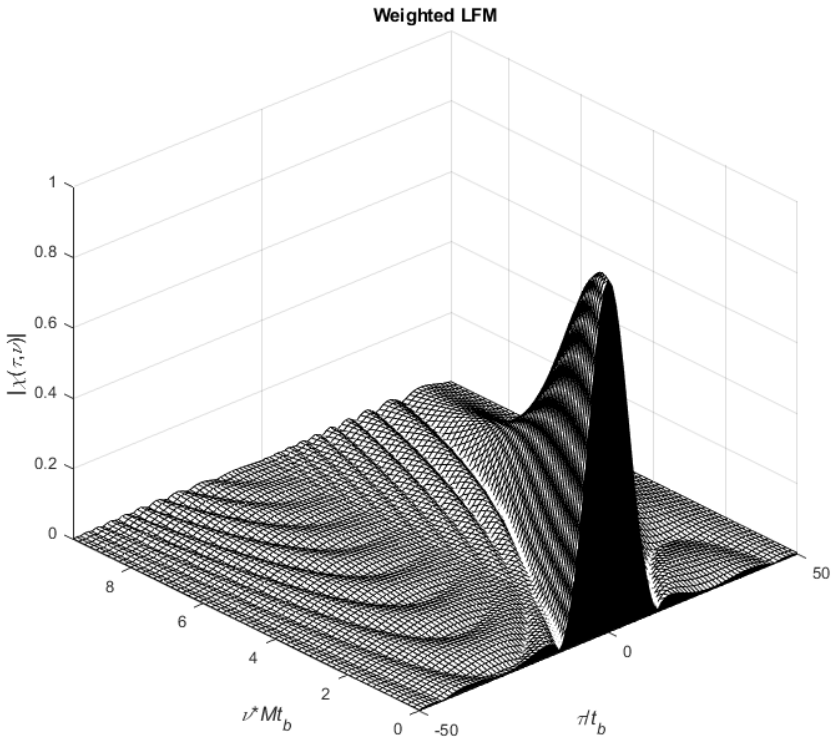

Figure 17. Ambiguity function plot of a weighted LFM signal

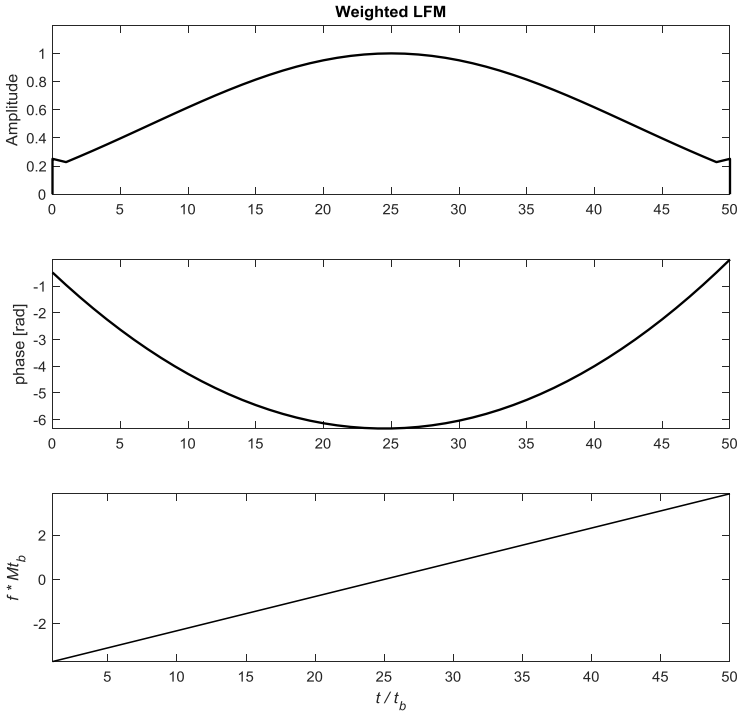

Figure 18. Signal parameters plot of a weighted LFM signal

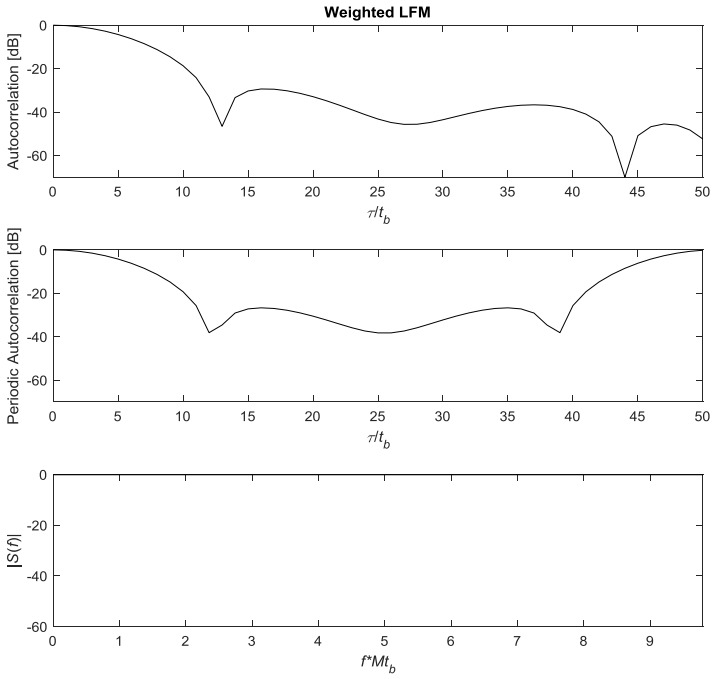

Figure 19. Autocorrelation and Spectrum plots of a weighted LFM signal

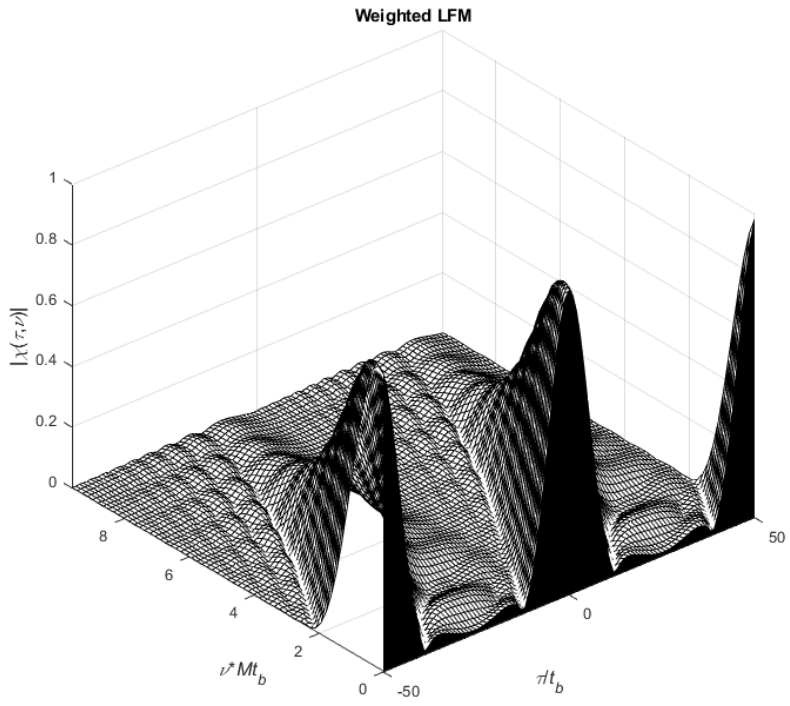

Figure 20. Periodic Ambiguity function plot of a weighted LFM signal

iv. Costas code

Another technique that is named Costas, is the exact opposite LFM pulses. It uses discrete frequency coding .

The Autocorrelation fuction of Costas can be found by overlapping two same matrices and in turn shifting them, in order to take into account delay (horizontal axis shifts) and Doppler (vertical axis shifts).

In the LFM, the number of coinciding dots will be N = M − |m|, representing delay and Doppler shifts of equal number of units. In the Costas signal case, this number's maximum value is one for all but the zero-shift case, where all dots coincide (N = M).

This unique characteristic gives us a narrow peak of the Ambiguity Function at the origin, and low sidelobes anywhere else.

ISSN:1791-4469

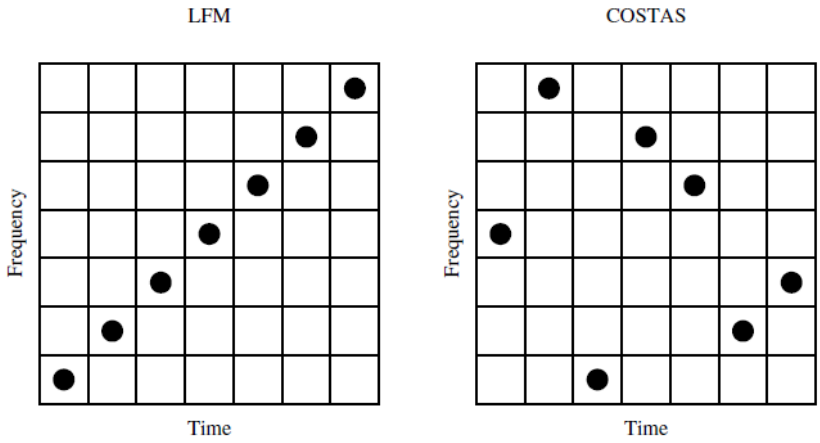

Figure 21. Binary matrix representation of LFM (left) and Costas coding (right) [5]

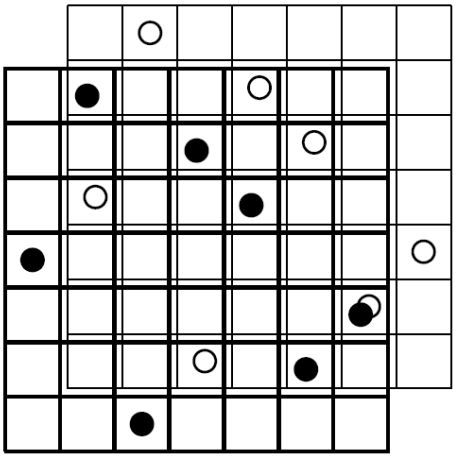

Figure 22. Example of one coincidence occurring at $\tau/t_b=1$, $\nu/\Delta f=1$ [5]

A closed-form expression of the Ambiguity Function of Costas is [5]:

$$\chi(\tau,\nu)=\frac{1}{\mathrm{M}}\sum_{m=1}^{\mathrm{M}}\exp[\mathrm{j}\,2\pi(\mathrm{m}-1)\nu\,\mathrm{t}_b]\{\Phi_{mm}(\tau,\nu)+\sum_{\substack{n=1\\ m\neq n}}^{M}\Phi_{mn}[\tau-(\mathrm{m}-\mathrm{n})\,\mathrm{t}_b,\nu]\} \tag{31}$$

where $$\Phi_{mn}(\tau,\nu)=\left(1-\frac{|\tau|}{t_b}\right)\frac{\sin\alpha}{a}\exp(-\mathrm{j}\beta-2\,\mathrm{j}2\pi\,\mathrm{f}_n\,\tau)\,,\ |\tau|\leq t_b\,,\text{zero elsewhere,} \tag{32}$$

in which $$\alpha=\pi(f_m-f_n-\nu)(t_b-|\tau|)\quad,\quad\beta=\pi(f_m-f_n-\nu)(t_b+\tau) \tag{33}$$

Below are plotted the Ambiguity Function (AF) (Fig. 23), the Autocorrelation Function (ACF) and Periodic Autocorrelation Function (PACF) (Fig. 25) and the Periodic Ambiguity Function (PAF) (Fig. 26) plots of the Costas signal derived from the numerical Ambiguity Function plotting program. The Ambiguity Function is calculated from coherent processing and the

sidelobe matrix doesn't use phase coherence. From these indications we proceed to the result that non-coherent processing will fit to Costas signals. At the zero-Doppler cut are shown various zero values at multiples of t_b and there are many sidelobes, as expected.

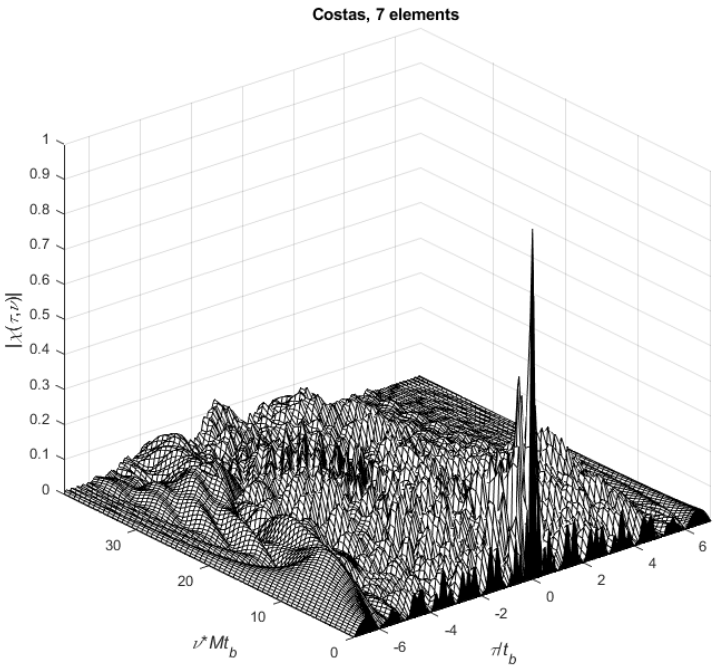

Figure 23. Ambiguity function plot of a 7 elements Costas signal

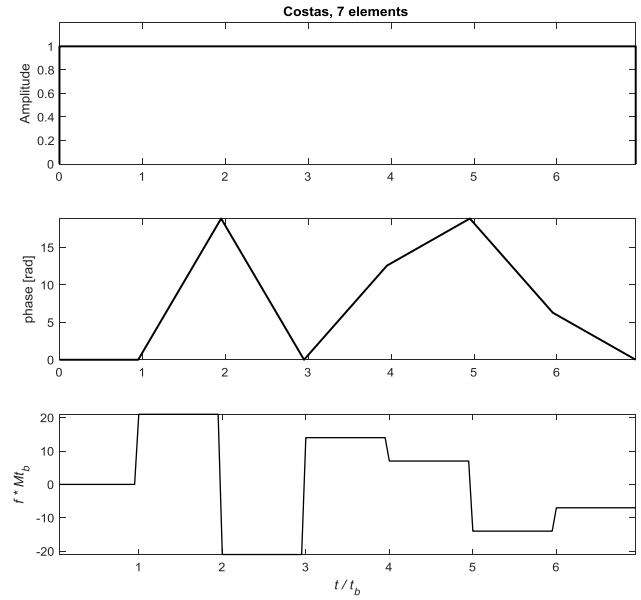

Figure 24. Costas signal parameters plot of a 7 elements Costas signal

ISSN:1791-4469

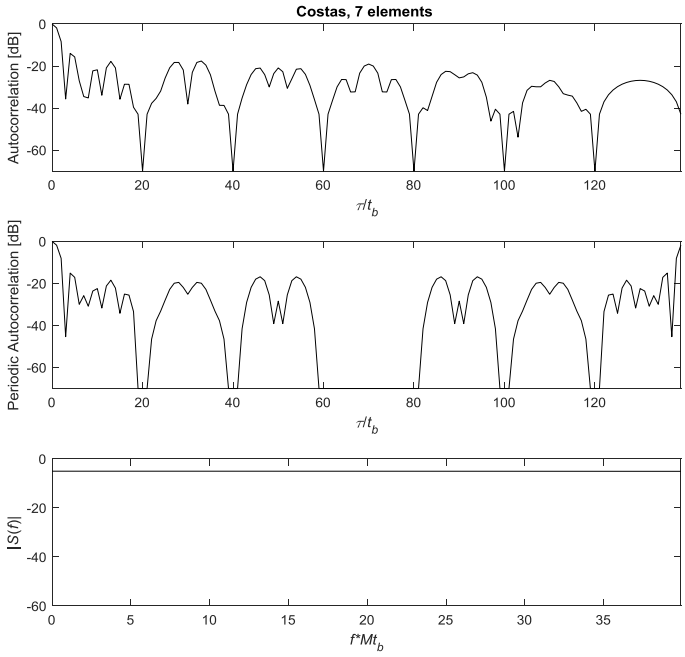

Figure 25. Autocorrelation and Spectrum plot of a 7 elements Costas signal

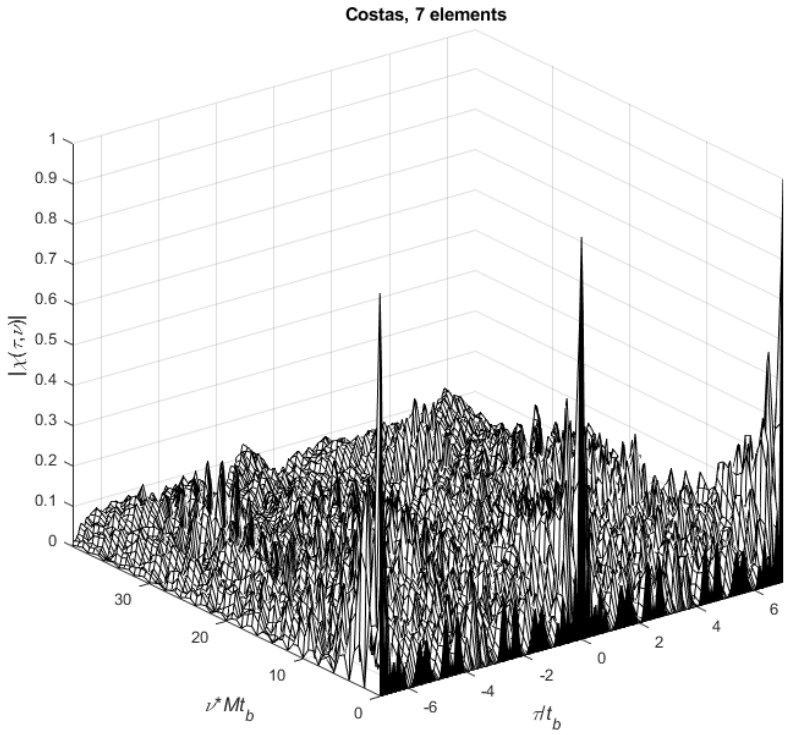

Figure 26. Periodic Ambiguity Function (PAF) of a 7 elements Costas signal

v. Barker code

Another pulse, that uses phase coding is named Barker code signal. It uses a set of *M* binary phases generating a peak-to-peak sidelobe ratio of *M*. It is well known that no binary Barker codes exists for 13 <*M* < 1 and for all odd *M* >13. It is also widely believed that there is no Barker code for all M >13. The main positive aspect of the binary Barker is its simplicity. Its main drawback is its limitation concerning the values of M. Below there is a table of all known binary Barker Codes followed by the Autocorrelation Function, Signal parameters, Autocorrelation and Spectrum and the Periodic Autocorrelation function plots.

Code Length	Code
2	11 or 10
3	110
4	1110 or 1101
5	11101
7	1110010
11	11100010010
13	1111100110101

Table 2. Binary Barker codes

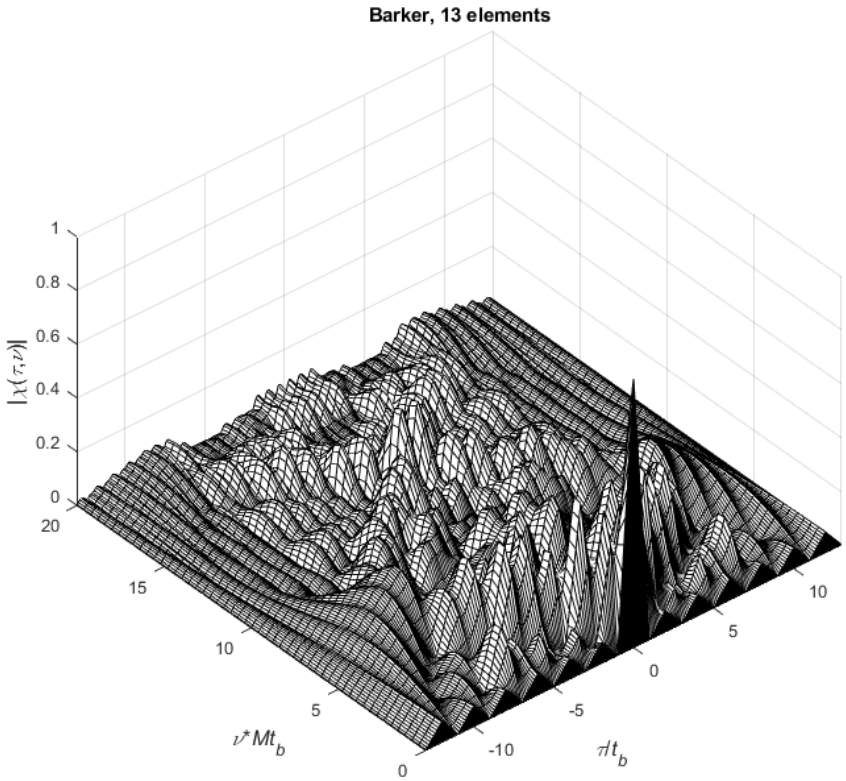

Figure 27. Ambiguity function plot of a 13 elements Barker code signal

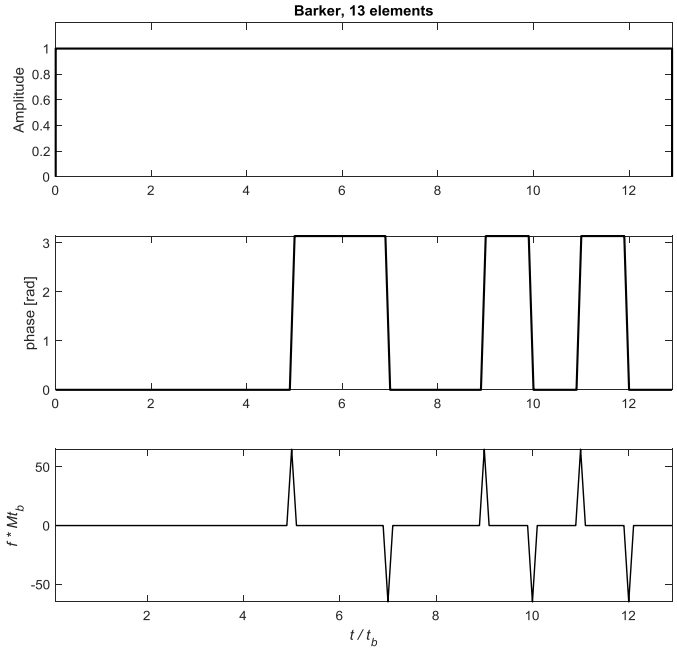

Figure 28. Signal parameters plot of a 13 elements Barker code signal

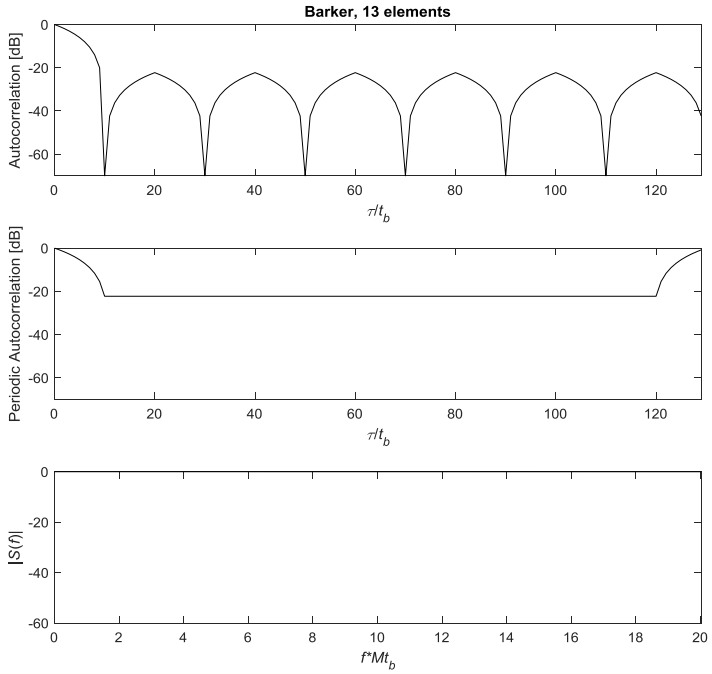

Figure 29. Autocorrelation and Spectrum plots of a 13 elements Barker code signal

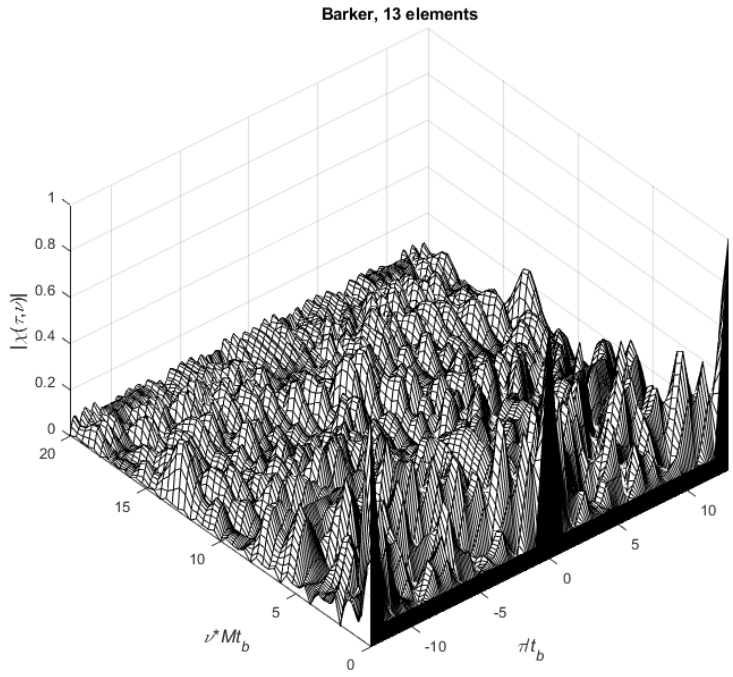

Figure 30. Periodic Ambiguity function plot of a 13 elements Barker code signal

vi. Frank code PSK

Frank code PSK waveforms are widely used in LPI radars, implementing the linear frequency modulation stepwise (step approximation). The values of the code were expressed by Frank using the elements of an $L \times L$ discrete Fourier transform matrix given by [5]:

$$\begin{bmatrix} 0 & 0 & 0 & \cdots & 0 \\ 0 & 1 & 2 & \cdots & L-1 \\ 0 & 1 & 4 & \cdots & 2(L-1) \\ \vdots & \vdots & \vdots & \ddots & \vdots \\ 0 & L-1 & 2(L-1) & \cdots & (L-1)^2 \end{bmatrix} \tag{34}$$

The original Frank code has two important properties:

i) the code is perfect and

ii) the aperiodic autocorrelation exhibits relatively low sidelobes

Its main negative property is that it is applied only for codes of perfect square length ($M = L^2$).

ISSN:1791-4469

The Ambiguity Function (AF) of a 16-element Frank Code signal is plotted below (Figure 32) along with its Autocorrelation Function (ACF) , the Periodic Autocorrelation Function (PACF) (Figure 34) and its Periodic Ambiguity Function (PAF) (Figure 35).

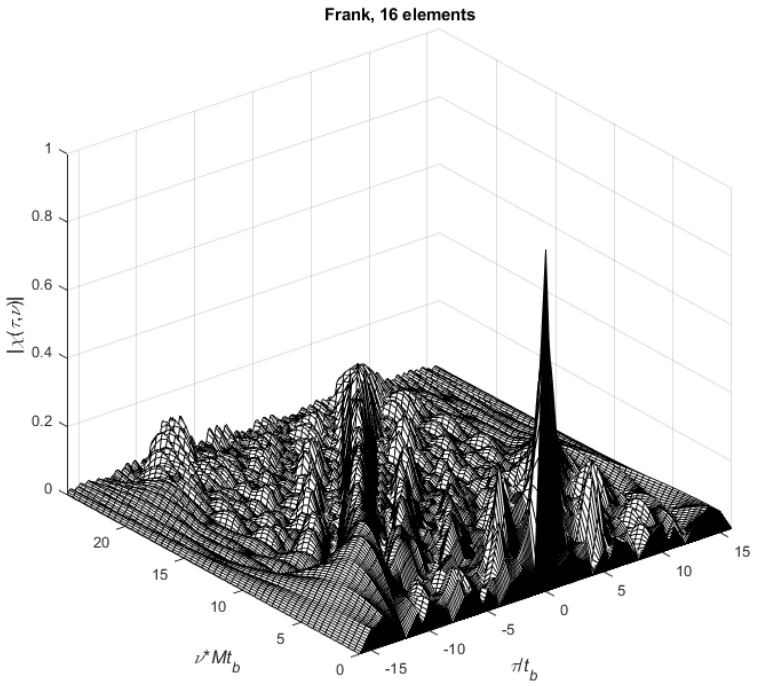

Figure 31. Ambiguity function plot of a 16 elements Frank Code signal

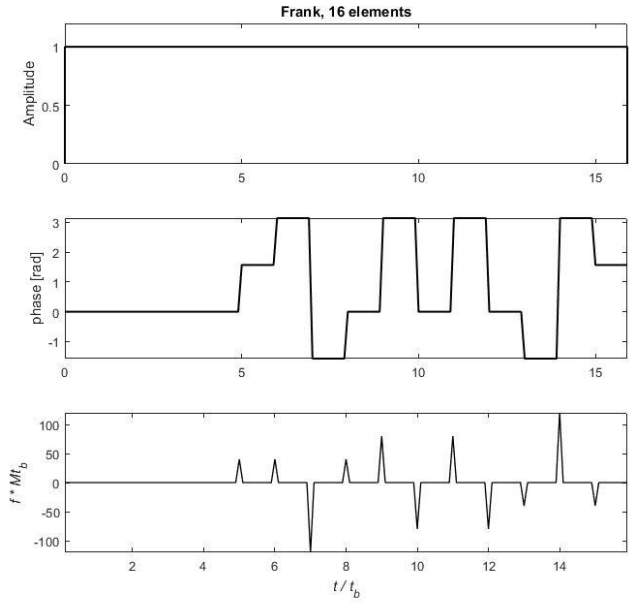

Figure 32. 16 Signal parameters plot of a 16 elements Frank Code signal

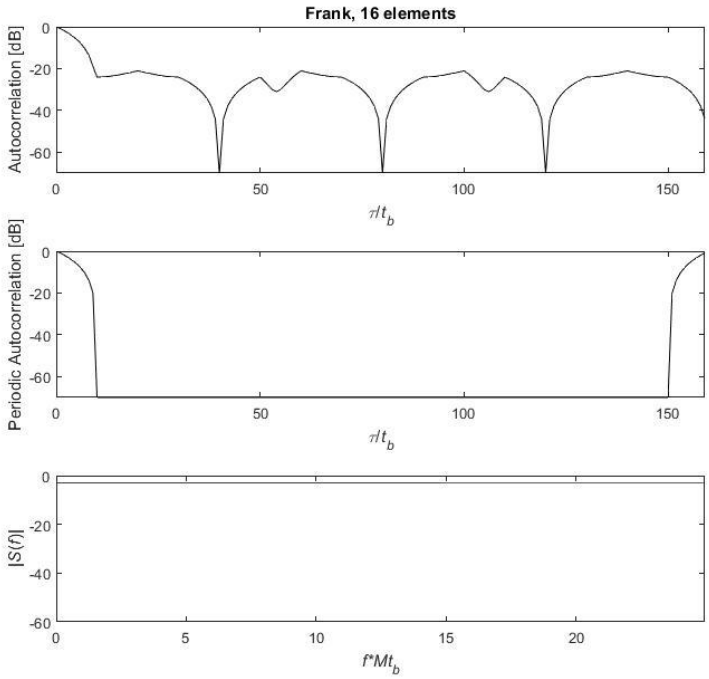

Figure 33. Autocorrelation and Spectrum plots of a 16 elements Frank Code signal

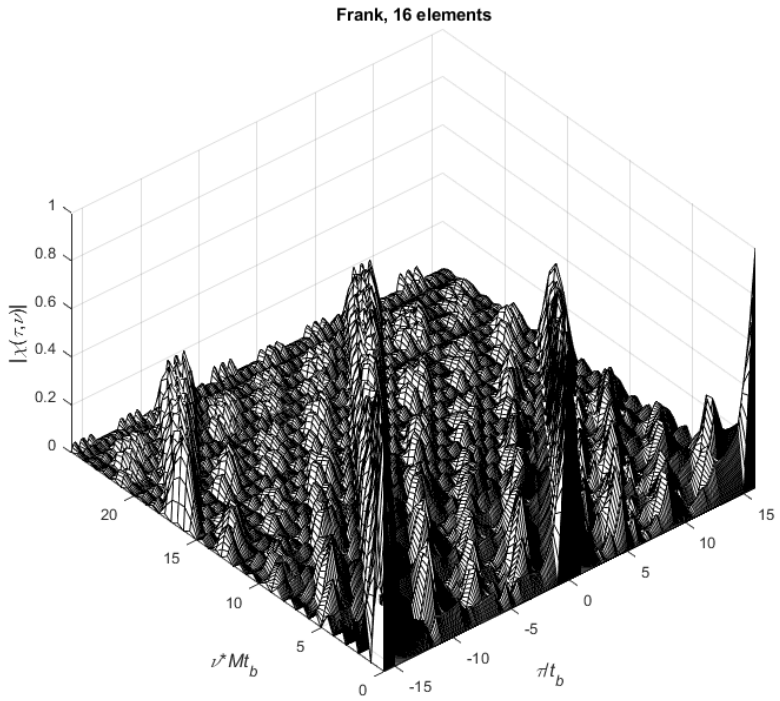

Figure 34. Periodic Ambiguity function plot of a 16 elements Frank Code signal

vii. Polyphase codes P1, P2, P3, P4

Instead of using Frank code, we can use other PSK waveforms called polyphase codes. Polyphase codes simulate the Linear Frequency Modulation (LFM) waveform. They differ from each other , having different code for the signal phase changes and the way they are generated in hardware. P1, P2, P3 and P4 codes have low level of sidelobes in the ACF and excellent tolerance to Doppler shifts.

P1, P2, P3 and P4 codes were introduced by Lewis and Kretschmer (P1, P2:1981 and P3,P4:1982).

P1 and P2 codes are stem from the Frank code.Their main drawback is that they can be applied only for square length (such as the Frank code). On the other hand, P3 and P4 codes are can be applied for any length *M*.

Lewis and Kretschmer later on (1983), proved that P3 and P4 codes show more tolerance than the Frank or P1 and P2 codes to Doppler shifts. For this reason we used P4 codes in our plots.

P4 code is defined for any length by [5]:

$$\varphi_m = \frac{2\pi}{M}(m-1)\left(\frac{m-1-M}{2}\right) \quad , \quad \text{where } 1 \le \text{m} \le \text{M} \tag{35}$$

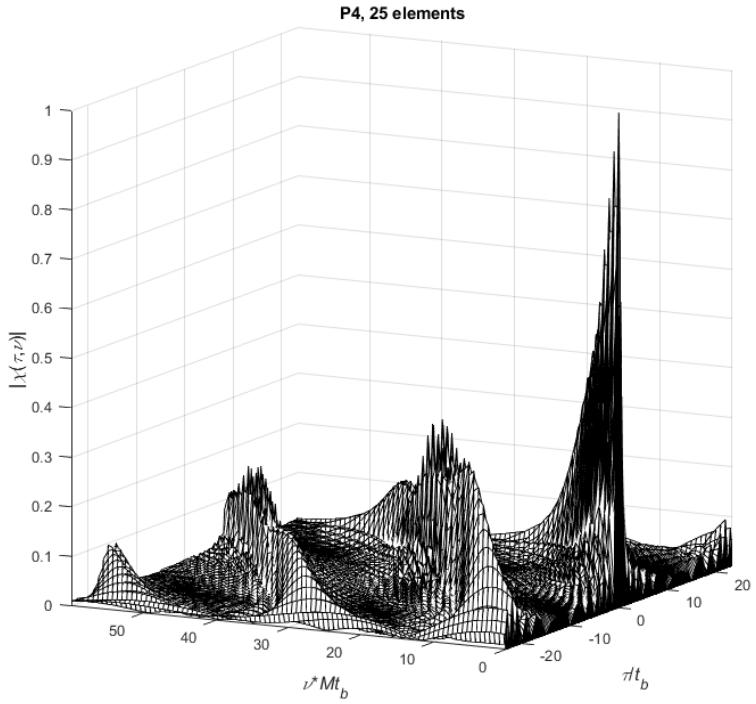

Figure 35. Ambiguity function plot of a 25 elements P4 signal

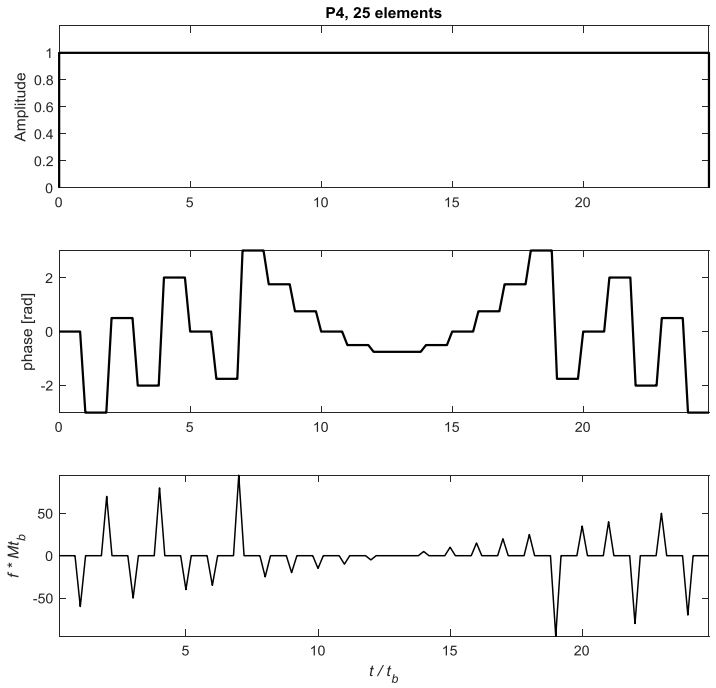

Figure 36. Signal parameters plot of a 25 elements P4 signal

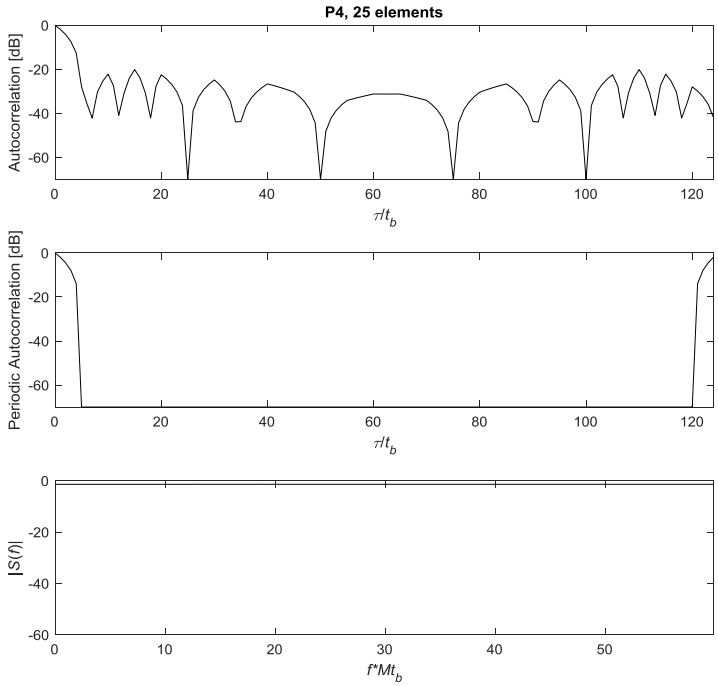

Figure 37. Autocorrelation and Spectrum plots of a 25 elements P4 signal

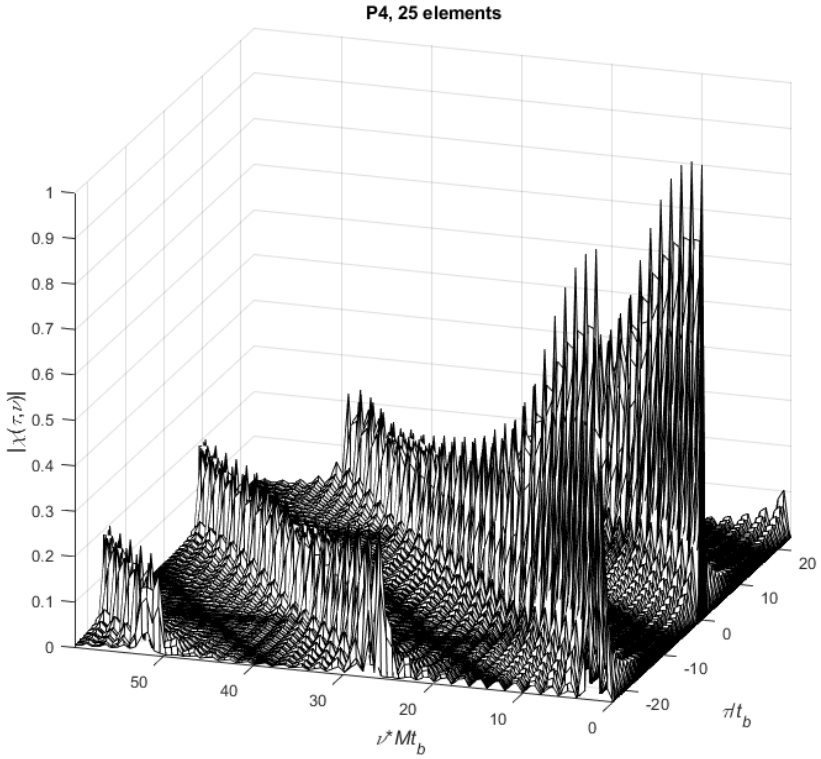

Figure 38. Periodic Ambiguity function plot of a 25 elements P4 signal

6. AMBIGUITY FUNCTION IN A BISTATIC RADAR [3]

The Ambiguity Function of the Monostatic Radar (Equation 1) differs depending on the relative target position in the bistatic plane. The Tsao et. Al. [3] version of this equation shows the non-linear relationships between target velocity and Doppler shift. Also, between target range and delay. The Ambiguity Function for a bistatic radar configuration is expressed as [3]:

$$\left|\chi\left(R_{R_H},R_{R_A},V_H,V_a,\theta_R,L\right)\right|^2=\left|\int_{-\infty}^{+\infty}\tilde{f}\left(t-\tau_a\left(R_{R_A},\theta_R,L\right)\right)\tilde{f}^*\left(t-\tau_H\left(R_{R_H},\theta_R,L\right)\right)\cdot \exp\left[-j\left(\omega_{D_H}\left(R_{R_H},V_H,\theta_R,L\right)-\omega_{D_a}\left(R_{R_a},V_a,\theta_R,L\right)\right)t\right]dt\right|^2 \quad (36)$$

where R_R and R_T are the ranges of the target from the transmitter and the receiver , V is the bistatic range rate, θ_R is the angle of the target measured from the receiver, L is the bistatic baseline, T is the transmitter–target–receiver delay time and subscripts $_H$ and $_a$ are hypothesized and actual values.

The illustration of this equation is depicted in the figures below, where a target's location and direction gives us the ambiguity function's results for four different cases (Figure 3 a,b,c,d). The waveform used is consisted of three rectangular pulses. From these figures we assume that when the target approaches the baseline between the receiver and the transmitter Figure 3 c,d (in Figure 3d a complete change of the scheme is observed), the change of the plot is more drastical than that of Figure 3 a,b, where the target approaches from a different direction.

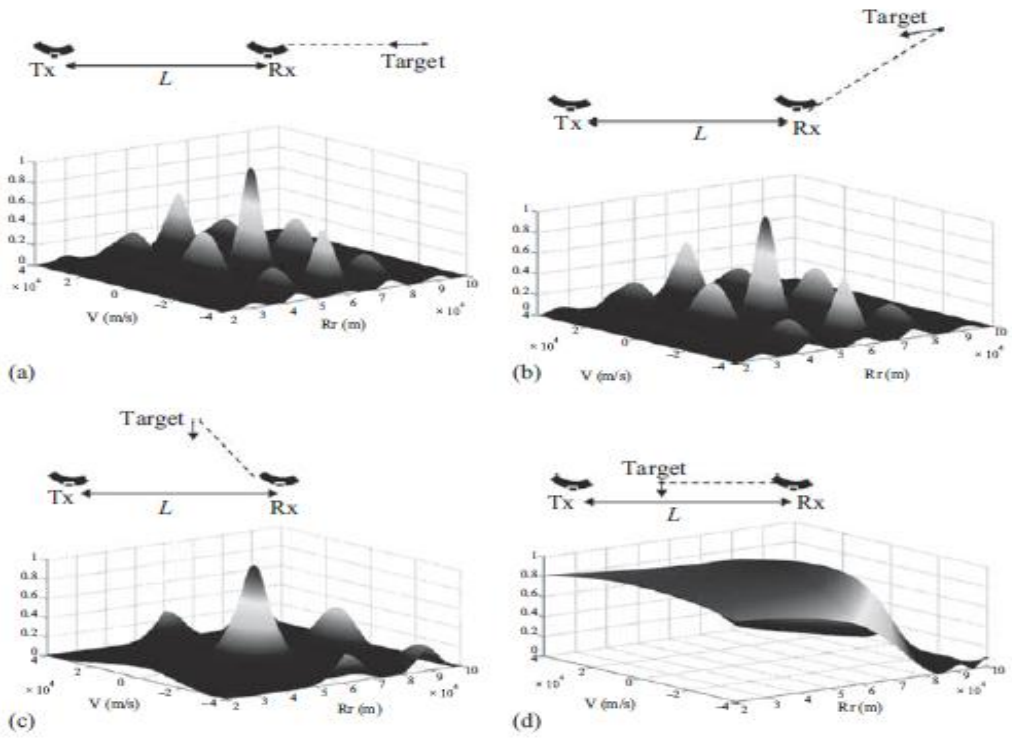

Figure 39. Bistatic ambiguity functions for four different target patterns [1]

7. CONCLUSIONS

As noted, bistatic radar alone cannot provide an adequate correlation peak for all relative locations of the target versus the Tx/Rx pair (e.g Figure 39). Thus, the netted radar solution seems to provide a realistic capability of detecting a target by accumulating individual target detections from the scattered receivers in the net. Regarding the LPI waveforms, P4 coding is a brilliant choice for a modern radar configuration due to low level of sidelobes in the ACF and excellent tolerance to Doppler shifts. Research continues in order to help the derivation of algorithms for optimal detection and the frequency range (e.g. DVB-T, FM) where a netted radar network can provide us a better performance in stealth target detection.

ISSN:1791-4469

REFERENCES

1. F. Gini et. al. (Eds) (2012), *"Waveform Design and Diversity for Advanced Radar Systems",* IEE ISBN 978-1-84919-266-8 (PDF).

2. N.Willis, *"Bistatic Radar",* Scitech Publ, 2005.

3. T. Tsao, et.al. *, "Ambiguity function for a bistatic radar",* IEEE Trans. Aerosp. Elect. Sys.,vol. 33, no. 3, pp. 1041–1051, July 1997.

4. G. Tsolis, (2011), "*Analysis and Processing of LPI Waveforms using Hilbert- Huang Transform and their Classification with Support Vector Machines",* PhD Dissertation, Aristotle University of Thessaloniki.

5. Nadav Levanon, Eli Mozeson *, "Radar Signals,* Wiley, 2004.

6. Baker, C. J. and Hume, A. L., "*Netted Radar Sensing*," Proceedings of the CIE International Radar Conference , pp. 110-114, 2001.